EUROPEAN COMMISSION
DIRECTORATE-GENERAL
Joint Research Centre

Institute for the Protection and the Security of the Citizen
European Laboratory for Structural Assessment (ELSA)
I-21020 Ispra (VA) Italy

Influence of the Quality of Construction on the Seismic Vulnerability of Structures

S. Dimova, P. Negro

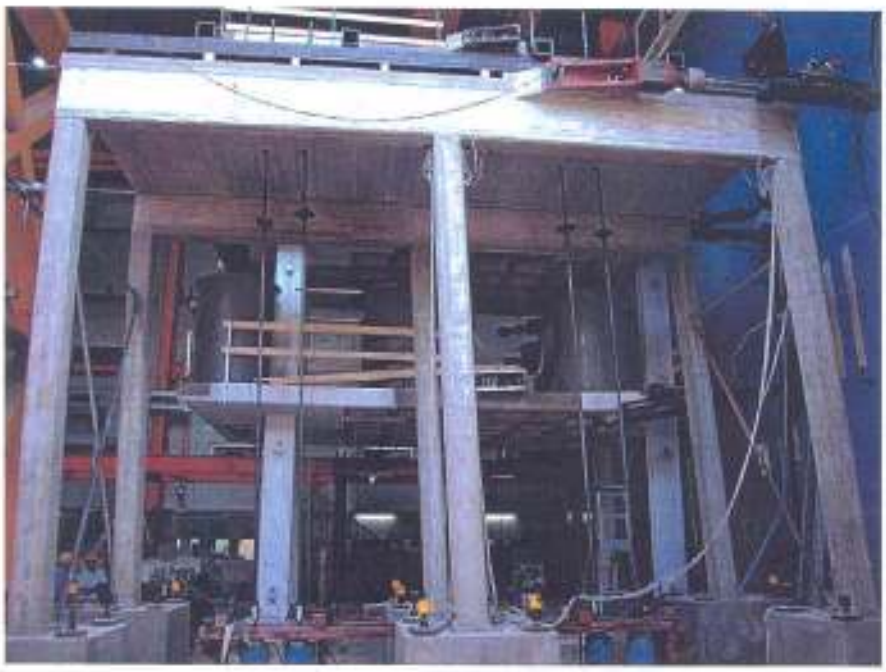

elsa

2004

EUR 21009 EN

CONTENTS

Acknowledgements

Some of the test results mentioned in the present report, namely the tests on the model referred to as "Structure A", were obtained as a part of the research project "Seismic Behaviour of Reinforced Concrete Industrial Building", funded in the V Framework Programme under the contract ECOLEADER. The project was coordinated by Prof. G. Toniolo from the Polytechnic of Milan, with the participation of the University of Ljubljana, the Italian Precast Industry Association (ASSOBETON), the Spanish Precast Concrete Association (ANDECE) and the Portuguese Concrete Products Association (ANIPC), and the collaboration of Prof. F. Karadogan from the Technical University of Istanbul.

In producing the work described in the present report, the authors received much assistance and information from Prof. Toniolo, as well from many partners of the ECOLEADER project, in particular from Dr. A. Colombo, Dr. L. Ferrara, Mr. C. Bonfanti and Mr. P. Kante.

The tests were performed at the European Laboratory for Structural Assessment. The enthusiasm and dedication of the whole ELSA staff has made possible the preparation and execution of the tests.

ABSTRACT

This report presents an experiment-based assessment of vulnerability of a cast- in-situ one story industrial reinforced concrete frame designed according to Eurocode 8. The influence of the quality of construction is estimated by consideration of two models of the experimental prototype: structure erected under special measures for control of the quality of execution and structure erected with normal measures for control of the quality of execution which resulted in significant deficiencies in the practical arrangement of the reinforcement. On the basis of the experimental data the displacement ductility and behaviour factor supply of the two structures are estimated. Their vulnerability is estimated by fragility analysis based on fitting the numerical models of the structural response in different seismic intensity levels to the experimental data. Widely used damage indices, such as the interstorey drift, the modified Park and Ang overall structural damage index and the homogenized reinforced concrete damage scale index are associated with the conditional probability of failure and the damage states of the studied structures are expressed in terms of their fragility. The damage states of the structures are related to the European Macroseismic Scale intensity. Quantitative expressions for the influence of the quality of construction to seismic capacity, behavior factor, seismic vulnerability and observational damage grade are provided. Recommendations for refinement of modern seismic design codes and particularly, Eurocode 8 to take into account the quality of construction are given.

1. **INTRODUCTION**

The forthcoming application of Eurocode 8 [2] necessitates experiment-based calibration of its design rules for the specific classes of buildings. Special attention deserves the estimation of the behaviour factor supply of structures, designed and detailed according to its prescriptions, in order to validate the admissible limits of reduction of the elastic seismic forces. The full-scale experimental tests make it possible to validate and develop concepts and numerical models, needed for the proper implementation of Eurocode 8 prescriptions in the research and future design practice. The experimental data are the unique source to adjust some of the wide-used damage indices and macro seismology damage descriptions to the degree of damage observed during the tests.

One of the main reasons for the extent of earthquake damage is attributed to the building quality. The damage observations of modern buildings after almost all recent earthquakes refer to cases of poor quality of materials, inadequate detailing of reinforcement and absence of capacity design principles, as for example [47, 48, 49, 50, 51, 52]. Though the quality of execution of the structures is reported as a widespread reason for earthquake damage, there are very few studies on this subject. Experimental tests on 2/3 scaled beam-column sub-assemblages, with structural deficiencies typical for Italian construction practice between the 50's and 70's, performed under seismic loading are reported in [52]. The seismic capacity of a two storey reinforced concrete (RC) frame with insufficient confinement in the critical zones of the columns was experimentally estimated and compared with the seismic capacity of similar frames, designed according to the Eurocode 8 requirements for ductility class 'High' and 'Medium' in [22].

Whereas the post-earthquake observations and the (few) experimental activities refer to the combined effects of poor quality of execution and inadequate detailing/lack of up-to-date seismic provisions, no studies seem to exist as for the effects of poor quality of execution in otherwise well conceived and designed structures. This problem is felt as deserving much attention, since it directly affects the performance of structures designed according to the new codes, and is the object of this study.

The studied cast-in-situ one storey RC frame was designed and tested in the European Laboratory for Structural Assessment (ELSA) of the Joint Research Centre (JRC) of the European Commission at Ispra in the framework of the research project 'Seismic behaviour of reinforced concrete industrial buildings' by means of the Ecoleader programme, which is reserved to the European Consortium of Laboratories for Earthquake and Dynamic Experimental Research. The objective of the project was to provide specific experimental evidence about seismic behaviour of precast one-storey frames for industrial buildings as compared to the corresponding cast-in-situ analogous structures. The results were expected to contribute to the correct calibration of Eurocode 8 design rules. To this purpose prototypes of precast one-storey frame and of cast-in-situ one-storey frame have been designed, both consisting of six columns connected by two lines of beams and an interposed slab. During the testing programme, the prototype of the cast-in-situ industrial frame corresponded to two models:

(i) structure erected under special measures for control of the quality of execution, referred further to as Structure A,

(ii) structure erected with normal measures for control of the quality of execution, which resulted in significant deficiencies in the practical arrangement of the reinforcement, referred further to as Structure B.

The present report deals with the interpretation of the experimental data and numerical modeling of the seismic response of the two models of the cast-in-situ industrial frame. On this basis the displacement ductility and behavior factor supply are estimated. The vulnerability of the structures is estimated by fragility analysis based on fitting the numerical models of the structural response in different seismic intensity levels to the experimental data. Widely used damage indices, such as the interstorey drift, the modified Park and Ang overall structural damage index and the homogenized reinforced concrete damage scale index are associated with the conditional probability of failure and the damage states of the studied structures are expressed in terms of their fragility. The damage states of the structures are related to the European Macroseismic Scale intensity. Quantitative expressions for the influence of the quality of construction to seismic capacity, behavior factor, seismic vulnerability and observational damage grade are provided. Recommendations for the refinement of modern seismic design codes and particularly, Eurocode 8 to take into account the quality of construction are given.

2. EXPERIMENTAL STRUCTURE

The one storey industrial frame shown in Figure 2.1 was designed according to Eurocode 2 [1] and Eurocode 8 [2] for ductility class H, as described in details in the design calculations [3].

Figure 2.1. View of the experimental frame

The two bays were 4 m each, the storey height was 5.3 m. In Figure 2.2 a the cross-sections of the columns are shown, which have been reinforced with 8 ϕ14 bars, stirrups ϕ6@50 mm in the critical zones and ϕ6@150 mm in the central part. The beams were reinforced with 8 ϕ14 bars, stirrups ϕ6@50 mm in the end zones and ϕ6@150 mm in the middle part, as shown in Figure 2.2 b, c. The design and experimental properties of the materials are given in Appendix A.

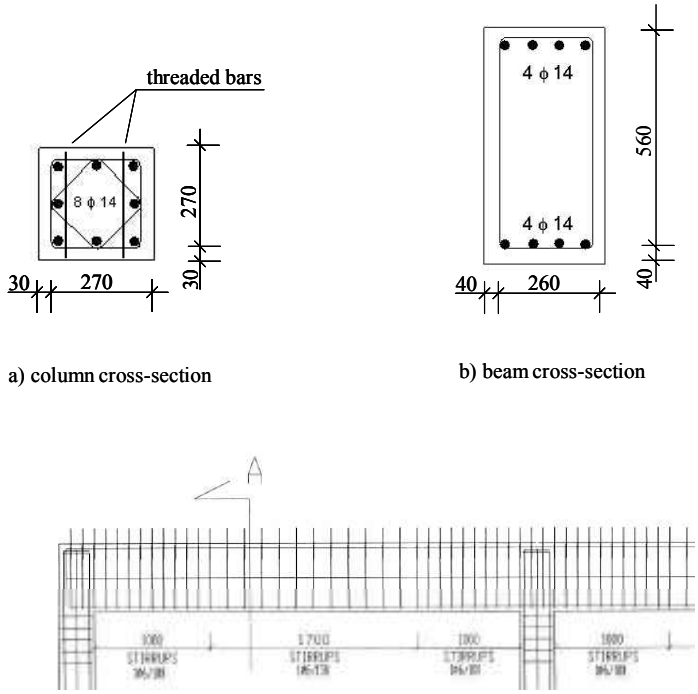

a) column cross-section

b) beam cross-section

c) detailing of beams and beam-column connections

Figure 2.2 a, b, c. Structural details

Normally, the dimensioning of such kind of industrial buildings for horizontal loads is determined by non-seismic design conditions, such as the wind loading. The total horizontal force the frame was able to sustain was evaluated as F_d = 192.9 kN, considering the design properties of the materials. In the structural design the accidental torsional effects were not considered, since such effects were not taken into account in testing.

The seismic excitation, which the structure was able to sustain, was evaluated by considering the initial stiffness, corresponding to the initiation of yielding of the reinforcement [2]. In this way the first natural period was calculated as T_1 = 1.01 s. The Eurocode 8 subsoil class B acceleration design spectrum S_d considered in [3] implies design seismic loading:

$$E_d = S_d \frac{W}{g} = a_g S \frac{2.5T_c}{qT} \frac{W}{g} \qquad (3.1)$$

where

S = 1.2 and T_C = 0.5 s for subsoil class A,
q = 4.95 is the behaviour factor for ductility class H,
a_g is the design ground acceleration,

g is the acceleration of gravity,
W = 720 kN is the weight of the structure.

Setting $F_d = E_d$, in [3] it was estimated that the structure was able to sustain seismic excitation with $a_g = 0.89\ g$.

The tests have been carried out in ELSA in November 2002 (Structure B)[46] and July 2003 (Structure A) by means of the pseudodynamic method [4, 5, 6, 7], which make it possible to overcome the limitations of weights and dimensions, which are associated with the use of shaking tables. In order to reproduce in the columns the design values of the axial loads, a total vertical load of 600 kN was applied by means of vertical jacks, as shown in Figure 2.1. The horizontal displacements were applied to the structure by means of hydraulic actuators connected with spherical joints to the deck, in the vicinity of the midspan of the first bay (see Figure 2.1). The resulting reaction forces were measured by load cells placed in the actuators.

The seismic excitation applied exhibits Eurocode 8 compatible design spectrum, as shown in Figure 2.3.

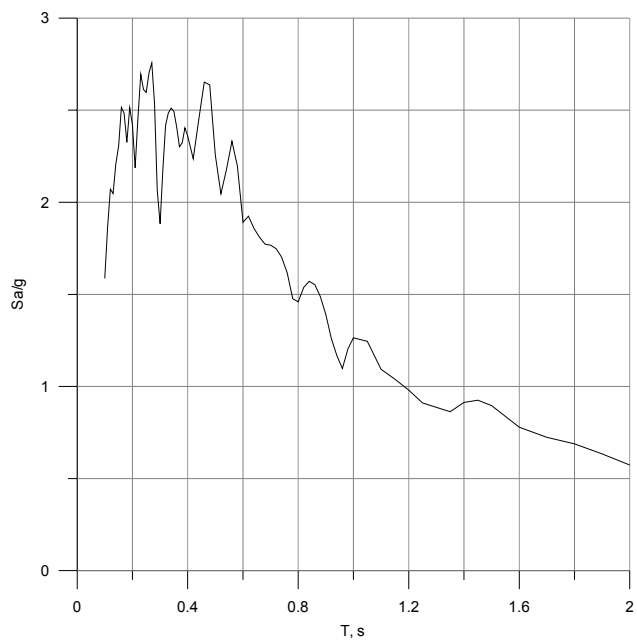

Figure 2.3. Acceleration response spectrum of the experimental accelerogram

3. STRUCTURE A

3.1 Experimental programme for Structure A

The experimental programme comprised pseudodynamic tests with peak ground acceleration (PGA) of 5% *g*, 32% *g*, 64% *g* and 80% *g*, as well as an additional displacement-controlled cyclic excitation [46].

The control measurement comprised the applied displacements and the related reaction forces. Structure A was instrumented by relative displacements transducers placed on three levels on the lateral faces at the top and bottom of one lateral column (further referred to as column NW) and one central column (further referred to as column NC) as shown in Figure 3.1 a, b for the bottom and top of the columns, respectively. The relative displacements at the top and bottom of one of the beams were measured at two levels, as shown at Figure 3.1 b for the bottom of the beam.

The part of the beam framing into the central column will be further referred to as the side NCW and the part framing into the lateral column will be further referred to as the side NEW. The denotations adopted for description of the experimental results and data about the disposition of the transducers are shown in Figure 3.2.

a) b)

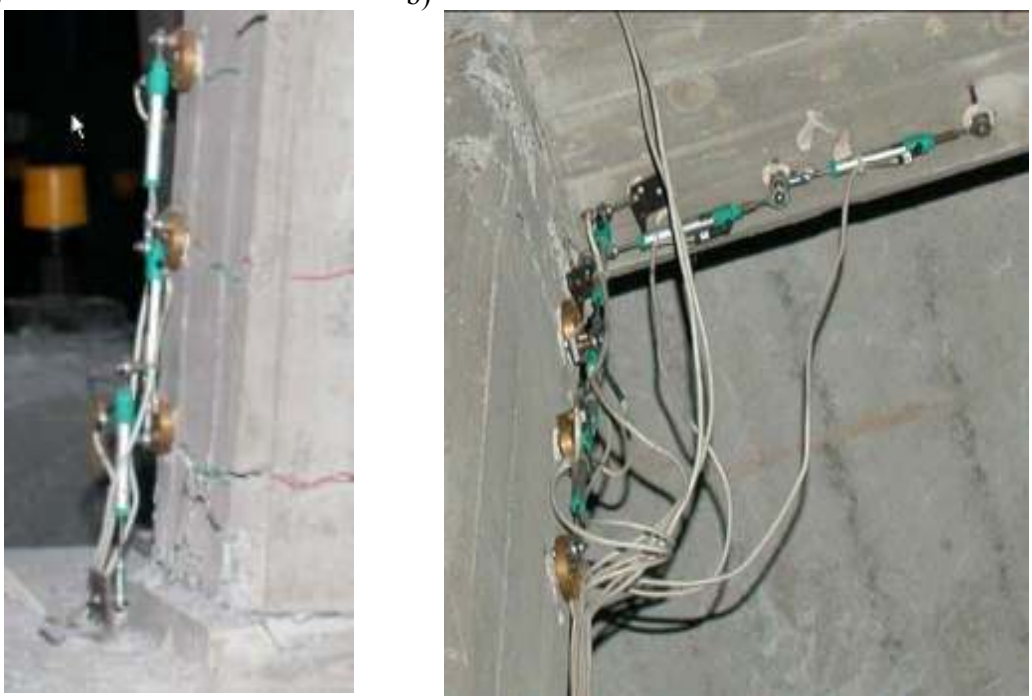

Figure 3.1 a, b. Details of instrumentation for measurement of relative displacements

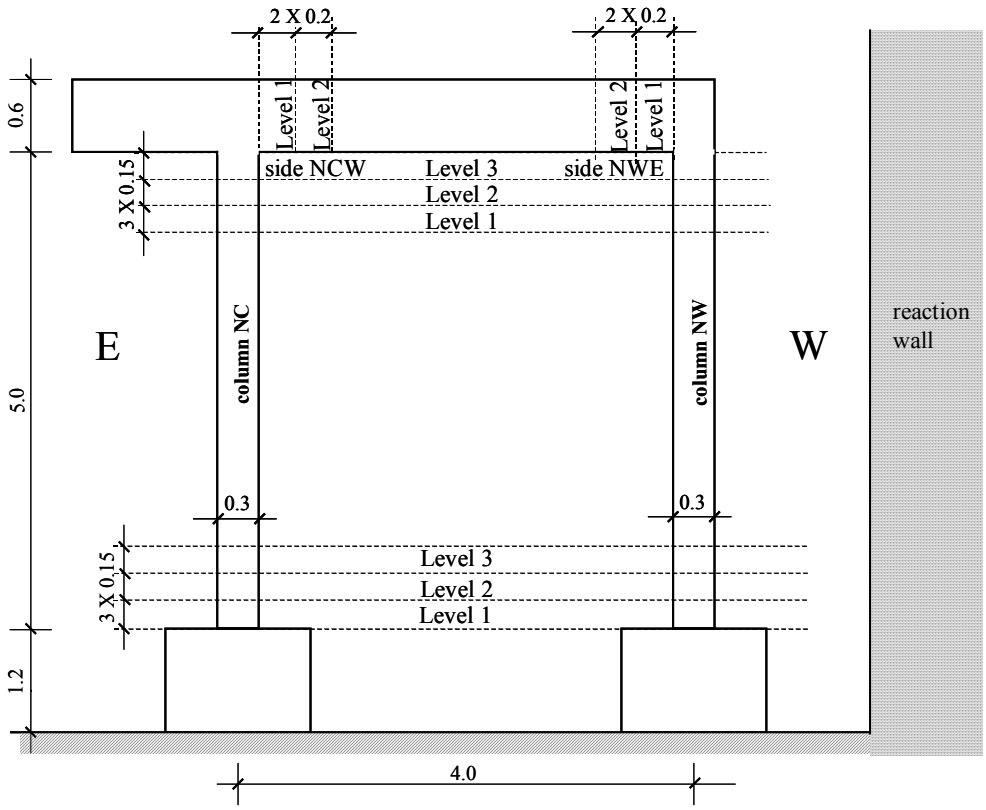

Figure 3.2. Scheme of the instrumentation of the structure (dimensions in meters)

On the basis of the measurements of the relative displacements, the mean curvatures for each segment were calculated as the estimated cross-section rotation divided by the corresponding gauge length. As it can be seen in Figure 3.1a, the lower ends of the lower transducers at the bottom of the columns were fixed to the foundation plate. In Figure 3.1 b is shown that the upper ends of the upper transducers attached to the top of the columns were fixed to the beam. Also, on the bottom of the beams, the ends of the transducers adjacent to the columns were attached to them, as depicted in Figure 3.1 b. This way of fixing the ends of the edge transducers implies that the measured displacements cannot be treated as the exact relative displacements between two points of one and the same element. They include also displacements due to the deformations along some additional part of the element in the beam-column or column-foundation joint and displacements due to the rotation of the adjacent element. These records were corrected considering that the relative displacements were obtained along distances, which were larger than the actual lengths of the instruments. For the top of the columns and the beams, it was assumed that the distance was equal to the length of the instrument plus the distance from the end of the instrument to the crossing of the geometric axes of the beam and column. For the bottom of the columns the distance equals the length of the instrument plus the length *l'* of the part of the columns embedded into the foundation, which reacts during dynamic excitations. The reacting embedded part, together with the design length of the column *l* was considered to form the effective length of the column l_e. During the test on Structure A the relative displacements of the zone embedded into the foundation of the columns were measured. The curvatures calculated from these measurements were not

negligible and gave reason and possibility to estimate the length *l'* as 0.15 m. Having in mind the much larger stiffness of the beams in comparison with those of the columns, the rotation of the beams was not considered when correcting the relative displacements on the top of the columns. The mean rotation at Level 3 of the top of the columns was calculated from the measured relative displacements and used for the correction of the records of the relative displacements at Level 1 of the instrumented beam (see Figure 3.2).

The curvatures calculated from the so-corrected records of the relative displacements of the beam still did not show any coincidence with the calculated ones, as shown in Figure 3.3 for the side NWE for one of the tests. There by '0.5 d col' the correction of the distance of the instrument by length from its end to the crossing of the geometric axes of the beam and column is marked.

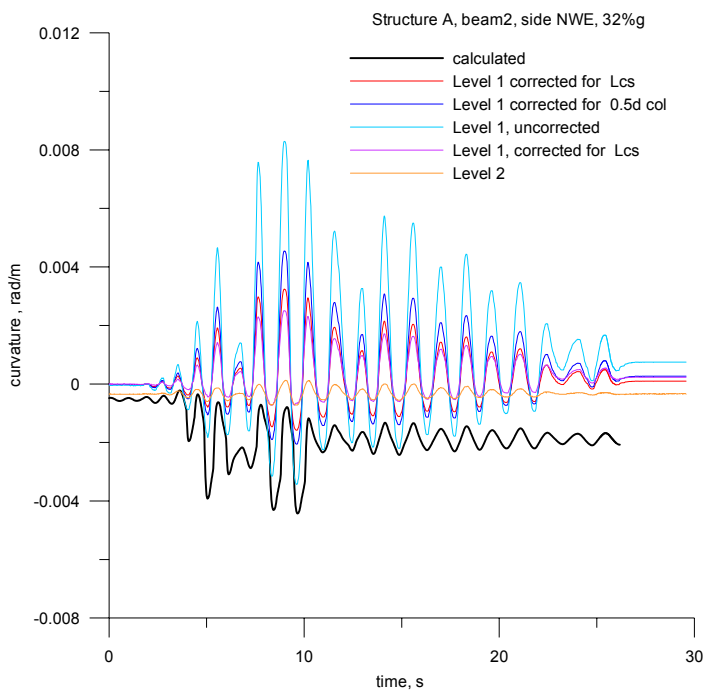

Figure 3.3. Correction of the data for estimation of the curvatures in the beam

As an alternative means for correction, the maximum slippage length L_{cs} specified in [11] was considered for beam-column joints. For interior joints L_{cs} is the column depth plus half of the beam depth, *i.e.* in the considered case, L_{cs} = 0.5 m. For the exterior joints L_{cs} is the straight lead embedment length plus the circumference of the bent up portion, in the considered case L_{cs} = 0.274 m. Using these corrections, the obtained curvature excursions have considerable similitude with the calculated ones. It should be noticed that, due to the large stiffness of the beams, their curvatures and measured relative displacements are much smaller than those of the columns. Since the measured values are small and tend to the exact limit of the transducers, no considerable coincidence with the calculated results should be expected.

3.2. Modelling of the seismic response of Structure A

3.2.1 Assumptions

The cross-section capacities were calculated by taking into account the hardening of the steel and the properties of the confined concrete, since in the critical zones of the structure the design envisaged spacing of the stirrups at 50 mm. The confinement index k for the columns according to [12] was 1.232. For the beams the confinement index was $k = 1.01$, due to the larger area of the cross-section and thus for the beams the confinement did not influence substantially the properties of the concrete. The characteristics of the confined concrete of the columns were calculated according to [12] as follows:

strength of the confined concrete $f_{cc} = k f_{cm} = 52.7$ MPa ,
strain corresponding to the peak stress $\varepsilon_{ccl} = k^2 \varepsilon_{cl} = 0.00371$,
strain corresponding to a 15% drop of the peak strength $\varepsilon_{cc85} = 0.021$.

The moment – curvature relationships are shown in Table 3.1, where the following denotations are used:

M_{cr} and φ_{cr} are the moment and curvature at cracking,
M_y and φ_y are the moment and curvature at yielding,
M_u and φ_u are the ultimate moment and curvature,
M_{des} is the design value of the resisting bending moment,
φ_{yp} is the curvature at yielding taking into consideration the pull-out of the reinforcing bars and shear effects, as considered below in the current section.

The moment – curvature relationships of the columns were estimated with reference to the values of axial forces N, used in the seismic design - N = 221 kN for the central columns and N = 100 kN for the lateral columns [3].

Table 3.1. Cross-section capacities

	M_{cr}, kNm	φ_{cr}, rad/m	M_y, kNm	φ_y, rad/m	φ_{yp}, rad/m	M_u, kNm	φ_u, rad/m	M_{des}, kNm	M_y/M_{des}
Lateral columns	25.4	$1.67\ 10^{-3}$	93.03	$18.5\ 10^{-3}$	$25.0\ 10^{-3}$	91.11	$200.8\ 10^{-3}$	78.6	1.18
Central columns	34.0	$2.33\ 10^{-3}$	106.46	$20.4\ 10^{-3}$	$27.0\ 10^{-3}$	82.33	$165.95\ 10^{-3}$	92.6	1.15
Beams	99.55	$8.82\ 10^{-4}$	180.93	$9.21\ 10^{-3}$	$18.7\ 10^{-3}$	220.36	$74.93\ 10^{-3}$	154.4	1.17

The seismic behaviour of the structure was modelled by means of the computer code IDARC 5.5 [13], taking into account the P-delta effects. The effective length of the columns $l_e = 5.45$ m was accepted, as determined for Structure B (see section 4.3.3 for more details). The tri-linear moment-curvature envelopes shown in Figure 3.4 a were specified using the cross-section characteristics given in Table 3.1.

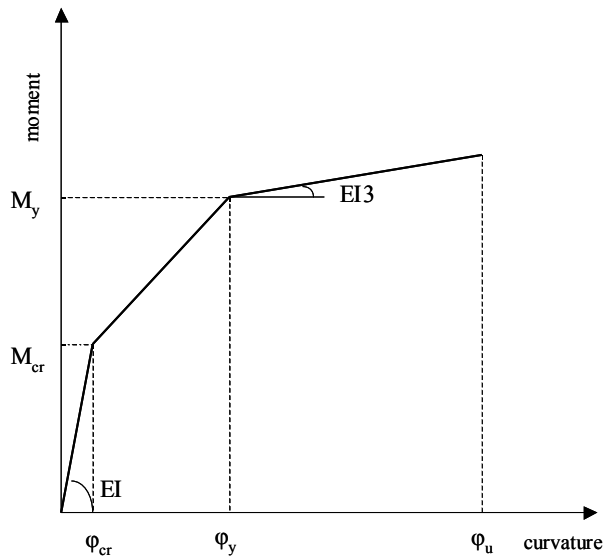

Figure 3.4a. Tri-linear moment-curvature envelope

In this way the initial stiffness *EI* of the members is determined by the cracking moment and the curvature at cracking. The yielding moments M_y are calculated by assuming that the reinforcement bars located in the middle of the cross-section are still not yielded in tension. The definition of M_y accepted in the study aimed at the proper determination of the first yielding in the system as an important parameter for the calculation of the behaviour factor (see section 3.4).

The yielding curvatures φ_y, shown in Table 3.1 were obtained by means of a fibre model [14] based on the cross-section parameters and material properties and do not account for the fixed-end rotations due to the bar pull-out and for the shear distortion of the shear span at flexural yielding. Yielding curvatures φ_{yp}, which account for the above phenomena were obtained based on the relationships for the yielding chord rotation given in [15, 16]:

$$\theta_y = \varphi_y \frac{L_s}{3} + 0.0025 + a_{sl} \frac{0.25\varepsilon_y d_b f_y}{(d - d')\sqrt{f_c}} \qquad (3.2)$$

where:

θ_y is the chord rotation at yield,
L_s is the shear span, $L_s = M / Q$ with M and Q the moment and shear force in the end cross-section obtained from the static linear solution,
a_{sl} equals either 1, if slippage of the longitudinal steel from its anchorage zone beyond the end section is possible, or 0 if it is not possible,
ε_y and f_y (in MPa) are the yield strain and strength of steel, respectively,
f_c is the concrete strength in MPa,
$d - d'$ is the distance between the tension and compression reinforcement.

The second term of Eq.(3.2) can be considered as the average shear distortion of the shear span at flexural yielding [16], the third term is the fixed-end rotation due to slippage. Based on Eq.(3.2), the chord rotations at yield were estimated as θ_y = 0.0209 for the lateral columns, θ_y = 0.0226 for the central columns, θ_y = 0.00514 for the beams considering the larger shear span and θ_y = 0.00436 for the beams considering the smaller shear span. The corrected values of the curvature at yield φ_{yp} shown in Table 3.1 were calculated assuming that the effects considered above do not substantially change the triangular distribution of curvatures at yield along the shear span, as $\varphi_{yp} = 3\theta_y / L_s$. For the beams, the more conservative value, corresponding to the larger shear span was accepted.

As an alternative, the case was considered, in which the increment of curvature due to the shear effects and the slippage is uniformly distributed over the potential plastic hinge length, and the plastic hinge length is equal to the depth of the member [17]. In this case the yield curvatures are φ_{yp} = 0.0367 rad/m for the lateral columns, φ_{yp} = 0.0386 rad/m for the central columns and φ_{yp} = 0.0136 rad/m for the beams (in this case it does not depend on the length of the shear span). The comparison of the simulated responses of the structure with these values of φ_{yp} shows substantial difference with the responses calculated with the values of φ_{yp} shown in Table 3.1 only for the seismic excitation with PGA of 5% g. In this case, the maximum member responses are influenced by the decreased slope in the second part of the three-linear moment-curvature envelopes, the maximum displacement increases by 0.8% and the maximum base-shear increases by 1.4%. In the further calculations the values of φ_{yp} shown in Table 3.1 were retained.

The hysteretic behaviour of the elements was modelled by use of the smooth hysteretic model, which offers better possibilities to trace the elastic-yield transition, the shape of unloading and the slip as compared to the three-linear hysteretic model. Due to the peculiarities in the structural behaviour at the different intensities of the imposed seismic excitation (PGA of 5% *g*, 32% *g*, 64% *g* and 80% *g*), separate hysteresis models for the columns were built for each test, in order to describe as better as possible the seismic behaviour of the structure. To take into account the effects of the previous excitations, acceleration spikes with the maximum amplitude of the previous excitation were imposed so to reach the maximum and minimum displacements attained during the previous excitation. Between the spikes and the test seismic excitation, a time interval with zero excitation was implied with duration sufficient for attenuation of the free vibrations caused by the acceleration spikes, as shown in Figure 3.4 b.

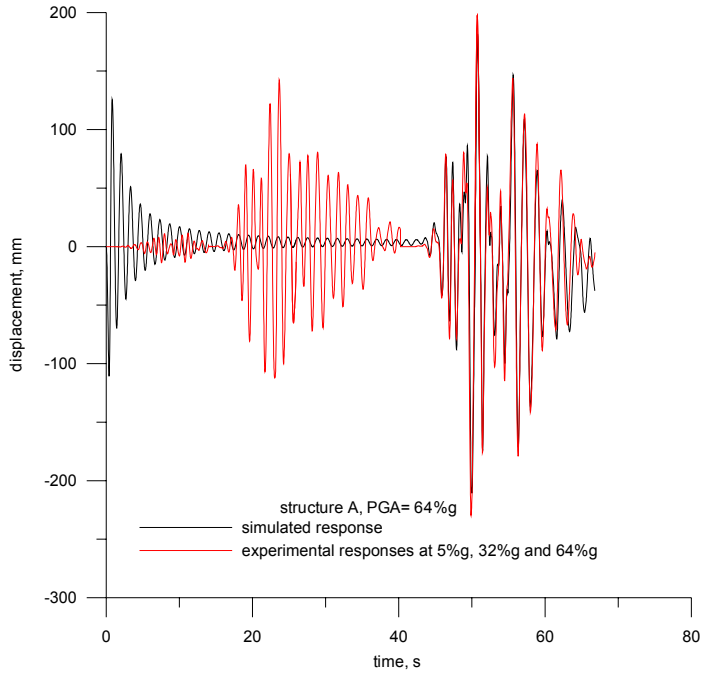

Figure 3.4 b. Modelling of the seismic excitation for the test with PGA of 64% *g*

This approach is intended as more appropriate than the application of the previous seismic excitation, since the new hysteresis model changes substantially the seismic behaviour of the structure during the previous excitations and no correct 'initial conditions' are imposed to the structure at the beginning of the considered test.

3.2.2 Are the models which best fit the experimental data correct?

As mentioned in section 3.2.1, four structural models were developed for the considered seismic excitations with different PGA in order to adjust the slope of the post-yielding branch of the moment-curvature relationship (see Figure 3.4 a), as well as the hysteresis properties, such as the stiffness degradation and strength decay, pinching effects, smoothness of the elastic-yield transition, *etc*. The calibrated models have yielded very good coincidence with the recorded displacement time histories and with the base shear – storey displacement relationships. In Figure 3.4 c such displacement time history for PGA of 64%g, denoted as model 1, is shown.

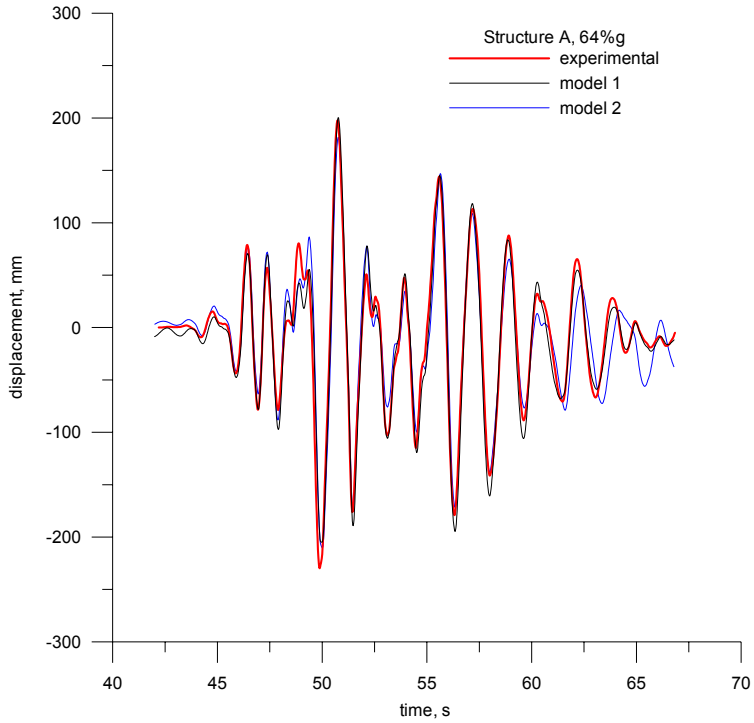

Figure 3.4 c. Displacement time histories obtained by two different numericalnumerical models

With the aim of performing the seismic fragility analysis, described in section 3.5, the maximum storey displacement was calculated for twenty seismic excitations compatible with the response spectrum of the experimental accelerogram (see Figure 3.4 d), but having longer effective duration.

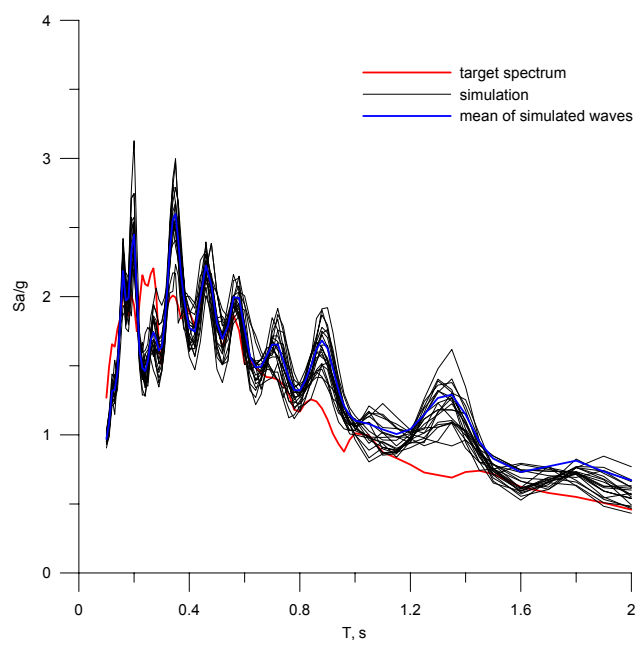

Figure 3.4 d. Acceleration response spectra of the generated accelerograms

The twenty accelerograms were generated in accordance with the procedure described by Clough and Penzien [34] as follows:

(i) non-stationary ground motions in terms of acceleration time histories were simulated;

(ii) an iterative procedure involving scaling in frequency domain was performed in order to match the specified target response spectrum.

The calculations were performed for PGA of 5% *g*, 32% *g*, 64% *g,* 80% *g* and 90% *g*. The models of the structure created to fit the experimental behaviour for the respective intensities were used. When examining the calculated maximum displacement, it was found that the maximum displacements calculated for the most of the generated accelerograms for PGA of 64% were larger than the respective values for PGA of 80% *g*, as shown in Table 3.2.

The reason for such incompatibility of the results, obtained from models very well fitting the experiment, is that there is no genealogy in their hysteresis parameters. IDARC 5.5 offers the possibility of using the smooth hystersis model for RC members. This model allows the elastic-yield transition, the shape of unloading and the slip in comparison to be more accurately modelled, but it uses eight parameters for description of these phenomena [13], namely:

HC, the stiffness degrading parameter, (HC ≥ 2, default: 200 – no degradation),
HBD, the ductility-based strength decay parameter, (default: 0.01 – no degradation),
HBE, the hysteresis energy-based strength decay parameter, (default: 0.01 – no degradation),
NTRANS, the smoothness parameter for elastic-yield transition, (default: 10 – bilinear),
ETA, the parameter for shape of unloading, (default: 0.5 – linear),
HSR, the slip length parameter,
HSS, the slip sharpness parameter, (default: 100 – no slip),
HSM, the parameter for mean moment level of slip.

In Table 3.3 the values of the above parameters, used in the initial models fitted to the experiment, are summarized. As it can be seen from Table 3.3, initially the stiffness degradation and the ductility-based strength decay of the model for PGA of 64% *g* were larger than in the model for PGA of 80% *g*. As a result, during the seismic excitations with longer effective duration and smaller PGA, the degradation of the considered structure was more intensive and the resulting maximum storey displacements – larger. The corrected models shown in Table 3.3 also exhibit very good coincidence with the experimental results, as reported in section 3.3, but there is a gradual change of the stiffness degradation and of the strength decay parameters, as well as of the smoothness and shape unloading parameters and of the parameters describing the slip. The maximum storey displacements obtained from them for the fragility analysis do not show incompatibility at the different levels of PGA, as described in section 3.5.

Table 3.2. Maximum simulated storey displacements (in mm)

Generated accelerogram №	PGA of 64% *g*	PGA of 80% *g*	Difference, mm
1	358.31	369.6	-11.29
2	399.18	352.18	47
3	293.13	313.12	-19.99
4	424.08	402.07	22.01
5	367.09	378.63	-11.54
6	361.47	355	6.47
7	340.81	409.95	-69.14
8	434.75	362.76	71.99
9	449.29	413.48	35.81
10	366.75	353.32	13.43
11	272.88	274	-1.12
12	251.47	285.2	-33.73
13	282.03	330.47	-48.44
14	384.59	391.26	-6.67
15	240.95	326.77	-85.82
16	371.85	342.89	28.96
17	361.57	469.97	-108.4
18	374.4	393.35	-18.95
19	368.84	360.47	8.37
20	350.29	367.89	-17.6

Table 3.3. Characteristics of the hysteresis models

PGA	HC	HBD	HBE	NTRANS	ETA	HSR	HSS	HSM
				initial models				
5% *g*	1	0.7	0.01	2	0.25	0.25	0.2	0.25
32% *g*	150	0.02	0.01	2	0.1	0.23	0.325	0.04
64% *g*	1.5	0.1	0.3	4	0.3	0.2	0.4	0.15
80% *g*	2	0.2	0.1	4	0.8	0.2	0.3	0.25
				corrected models				
5% *g*	200	0.05	0.01	1.27	0.1	0.27	0.32	0.01
32% *g*	70	0.2	0.01	1.27	0.1	0.23	0.33	0.01
64% *g*	2	0.2	0.01	4	0.4	0.2	0.3	0.15
80% *g*	2	0.2	0.1	4	0.8	0.2	0.3	0.25

Consequently, when using different models for the description of the seismic response of structures to different intensities, the genealogy of their hysteresis parameters is a prerequisite for their adequateness. Simulations with accelerograms with longer effective duration could be recommended for the validation of such models.

3.3. Experimental tests and their numerical simulations

3.3.1 Test with PGA of 5% g

The recorded restoring force – displacement relationship (see Figure 3.5 a) shows the effects of initiation of cracks in the concrete. The maximum storey displacement was 0.25% of the storey height. From the first 4 seconds of the record, when there was still no stiffness degradation, the elastic stiffness of the structure was estimated as k_{el} = 5943 kN/m. Thus the fundamental period of the structure was estimated as T_{1A} = 0.691 s.

From the numerical model, a fundamental period of 0.68 s was obtained, which coincides well with experimental period. As shown in Figure 3.5 a, the calculated hysteresis loop reflects very well the slope of the recorded loop, but does not adequately reproduce the effects of micro cracking, since the model used (see Figure 3.4 a) implies linear moment-curvature relationship for this seismic intensity level. This deficiency of the model was balanced by introducing in the model structural damping of 3 % of critical. As it can be seen in Figure 3.5 b, the calculated displacement time history exhibits very good coincidence with the experimental data. Due to the very small measured relative displacements, which are close to the resolution of the transducers, no curvatures were calculated for this test.

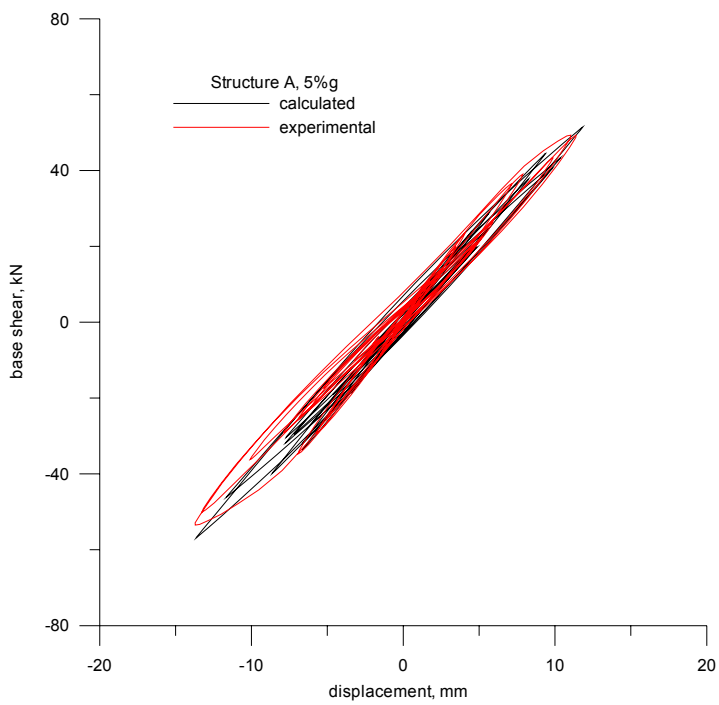

Figure 3.5 a. Hysteresis loop for PGA of 5% *g*

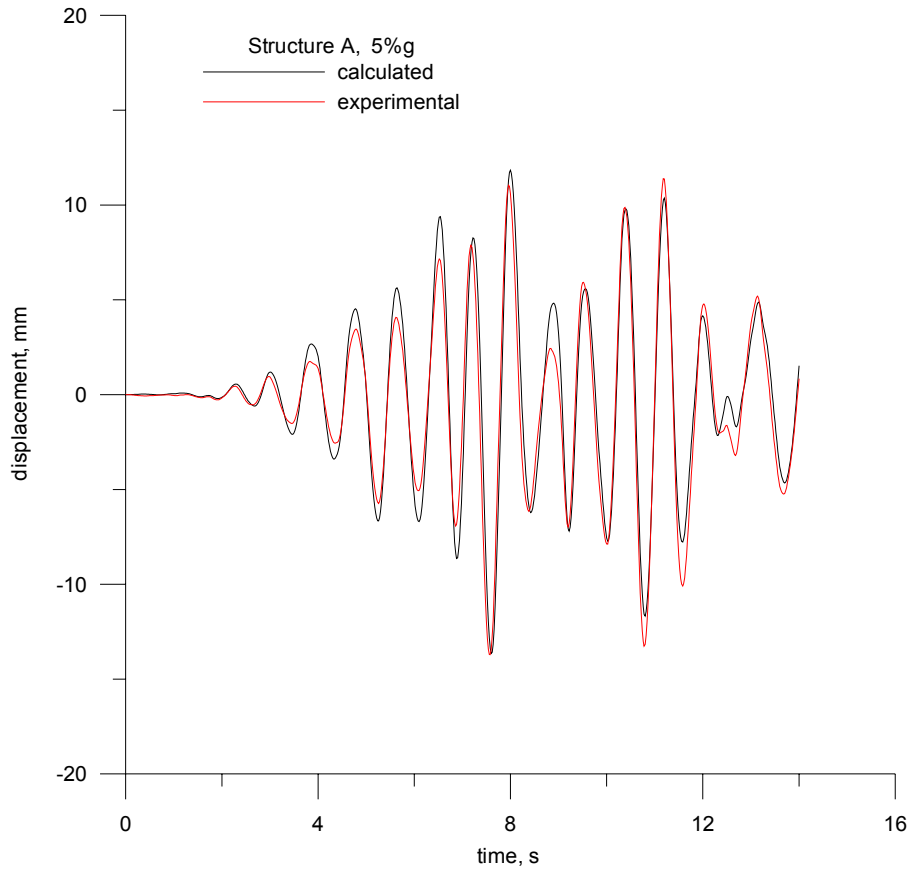

Figure 3.5 b. Displacement time history for PGA of 5% *g*

3.3.2. Experimental test with PGA of 32% g

During the seismic excitation with PGA of 32% g, the structure reached the first yield at the bottom of the lateral columns, as described in details in section 3.4.2. Flexural cracks appeared in the columns near the joints. The maximum storey displacement was 2.6% of the storey height. In Figures 3.6 a and 3.6 b, the calculated displacement time history and base shear-story displacement relationship are compared with the experimental ones, showing good agreement.

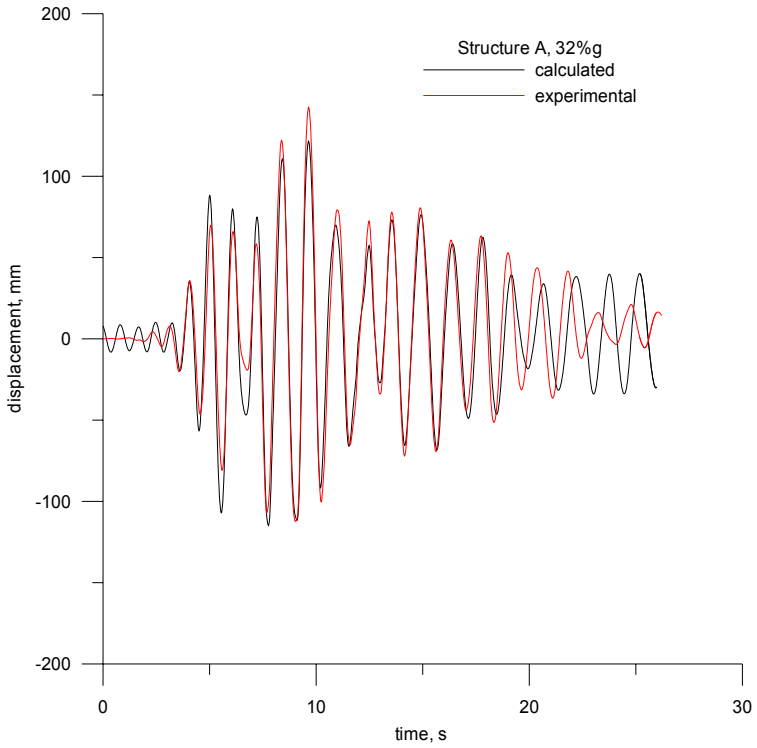

Figure 3.6 a. Displacement time history for PGA of 32% *g*

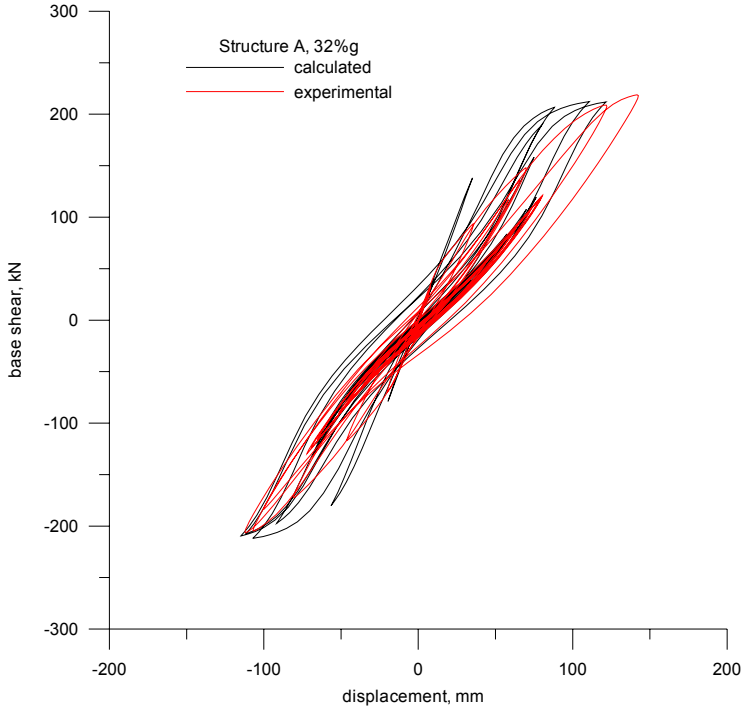

Figure 3.6 b. Hysteresis loop for PGA of 32% *g*

In Figures 3.7 a,b the calculated curvatures at the bottom and top of column NC are compared with the experimentally obtained ones.

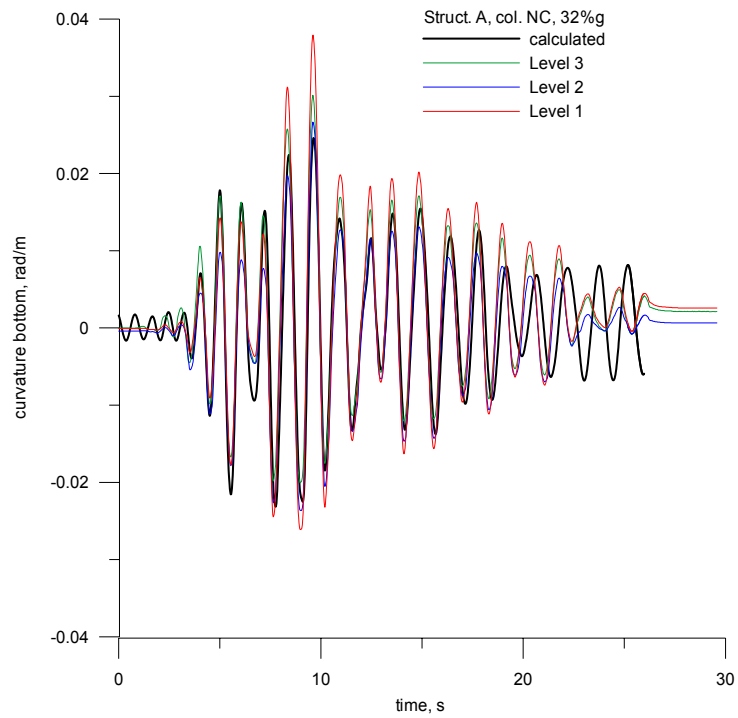

Figure 3.7 a. Curvatures at the bottom of column NC for PGA of 32% *g*

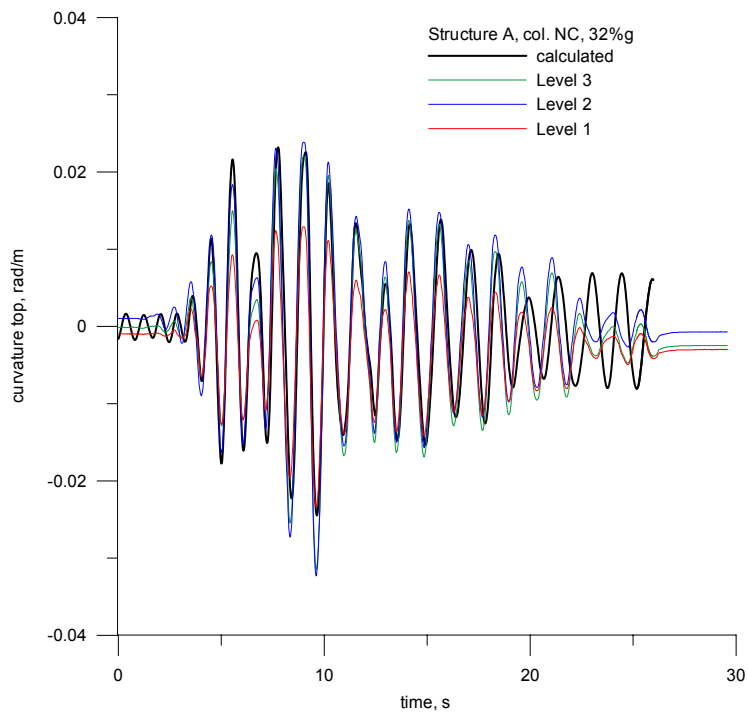

Figure 3.7 b. Curvatures at the top of column NC for PGA of 32% *g*

In Figures 3.8 a,b the calculated and the experimentally obtained curvatures at the bottom and top of column NW, respectively, are shown.

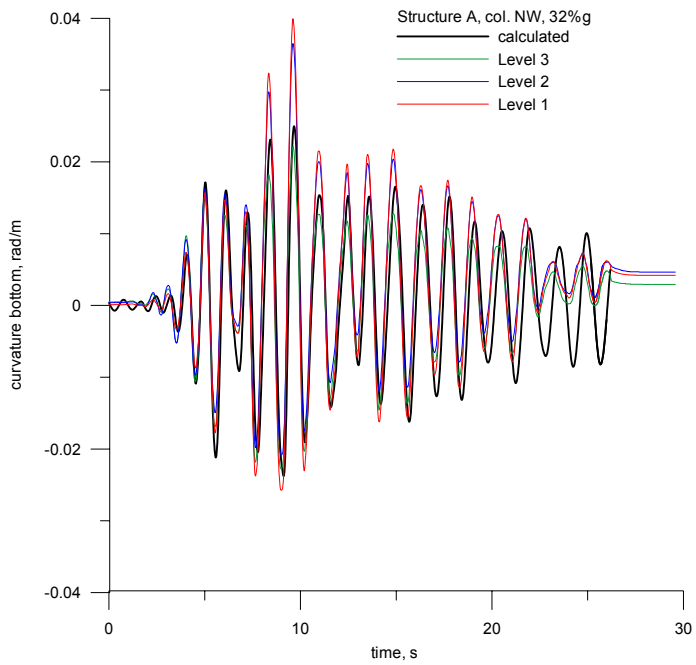

Figure 3.8 a. Curvatures at the bottom of column NW for PGA of 32% *g*

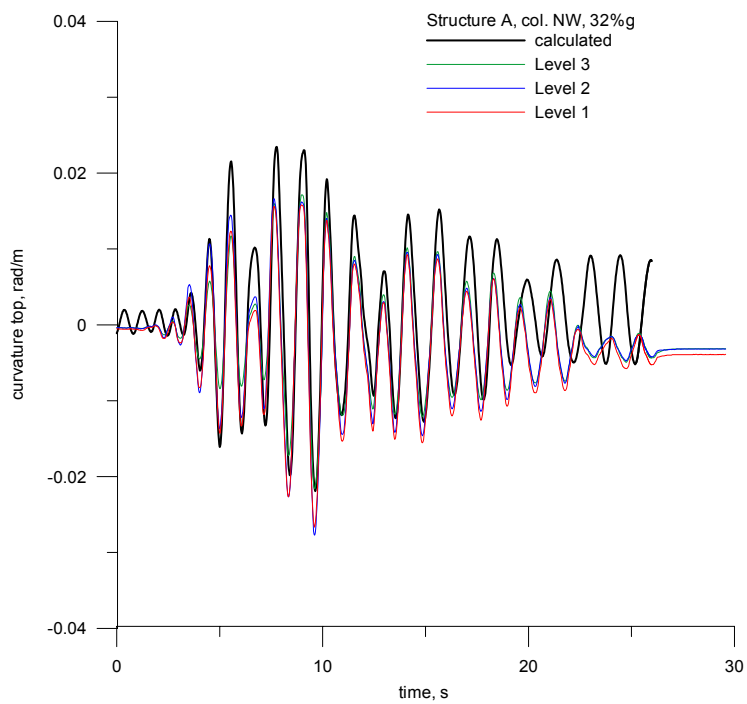

Figure 3.8 b. Curvatures at the top of column NW for PGA of 32% *g*

The measured mean curvatures in the segments with largest moments (Level 1 and Level 2 at the bottom of the columns and Level 3 and Level 2 at the top of the columns, as shown in Figure 3.2) agree well with the calculated curvatures. For the case of the bottom of column NW, the measured curvatures are shifted up, but the curvature excursions coincide well with the calculated ones. Such shifting was observed in other measured curvatures, such as at Level 3 at the bottom of column NC. The shifting could be explained by some inaccuracies in the measurements due to the small relative displacements recorded. As it will be seen furthering the following, during the tests with larger values of PGA, such shifting did not appear.

In Figure 3.9 a,b the calculated and the measured mean curvatures at Level 1 and Level 2 (see Figure 3.2) are compared, based on corrected measurements, as described in section 3.1.

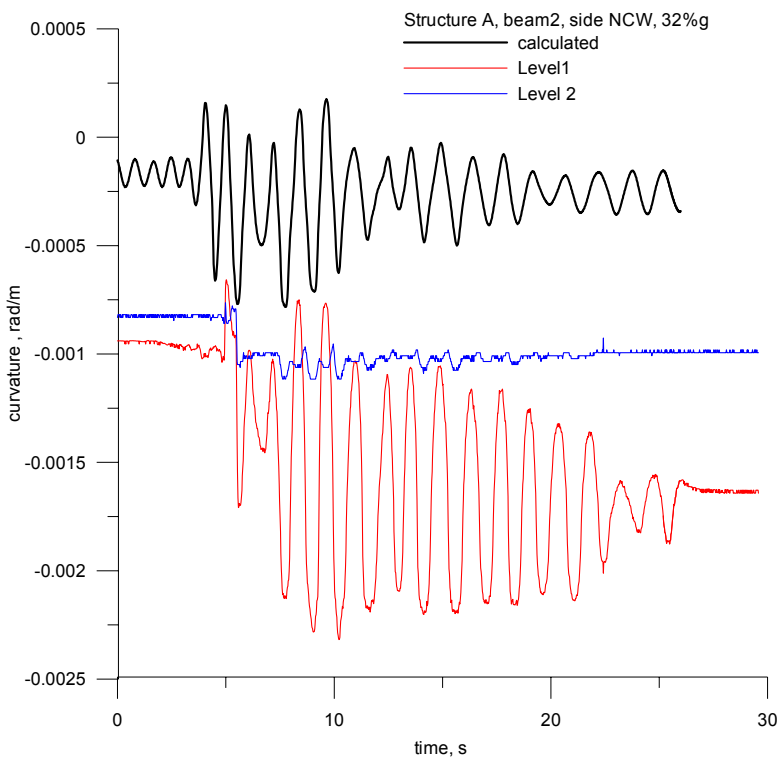

Figure 3.9 a. Curvatures at the site NCW of the beam for PGA of 32% *g*

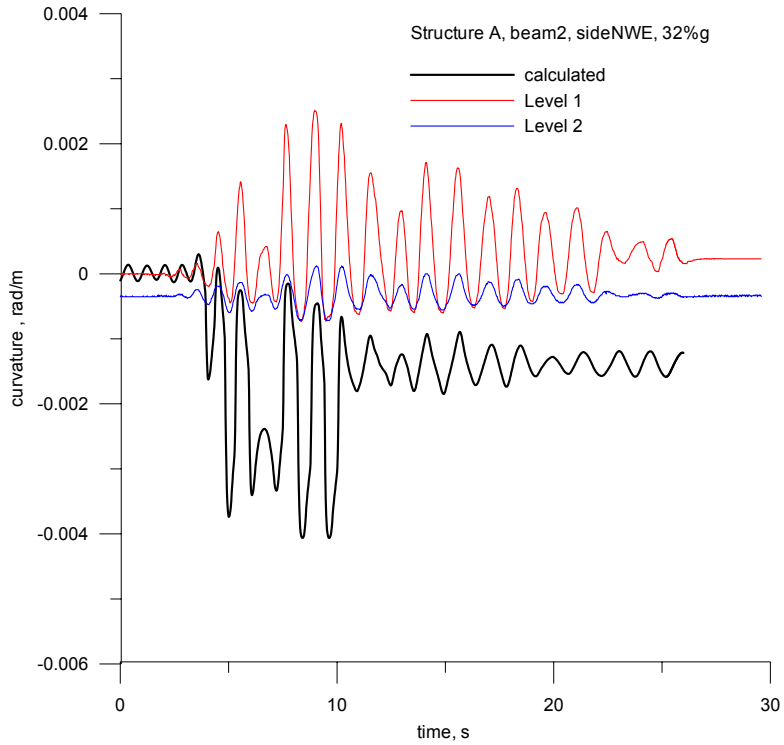

Figure 3.9 b. Curvatures at the site NWE of the beam for PGA of 32% *g*

For the beam side new, the calculated curvature excursions show coincidence with the measured mean curvature excursions at Level 1. For the beam side NCW, the measured mean curvature excursions at Level 1 are larger than the calculated ones. This generally not good agreement between the experimental and calculated results could be explained by the small magnitude of the beam curvatures under the seismic excitation with PGA of 32% *g* and the correspondingly small relative displacements measured.

3.3.3 Experimental test with PGA of 64% g

During this test, the columns underwent large plastic excursions. The flexural cracks, obtained during the test with PGA of 32%g enlarged and new flexural cracks appeared along the height of the columns. No visible cracks appeared in the beams, and in the beam-column connections as well. The maximum storey displacement was 4.2 % of the storey height. In Figures 3.10 a, b the calculated displacement time history and base shear - storey displacement relationship are compared to the experimental ones, showing very good agreement.

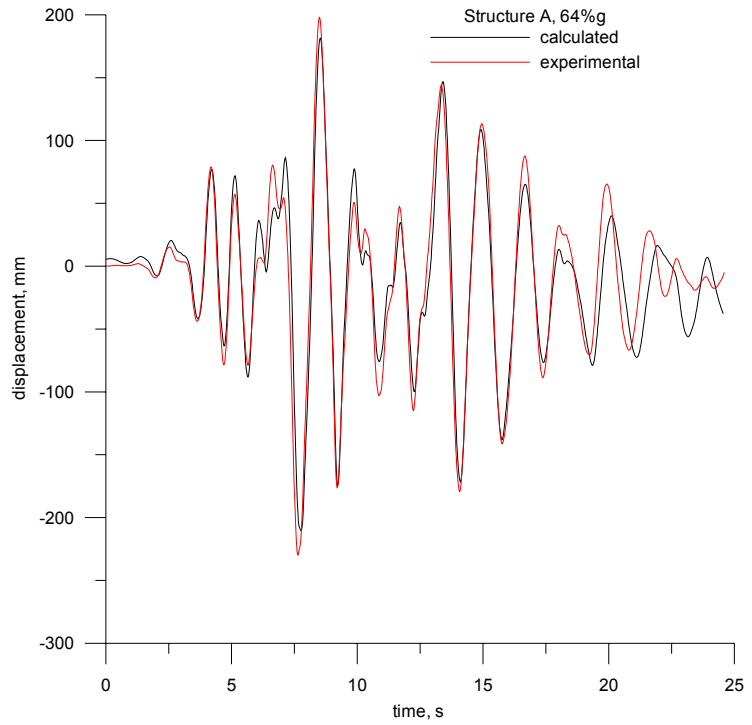

Figure 3.10 a. Displacement time history for PGA of 64% *g*

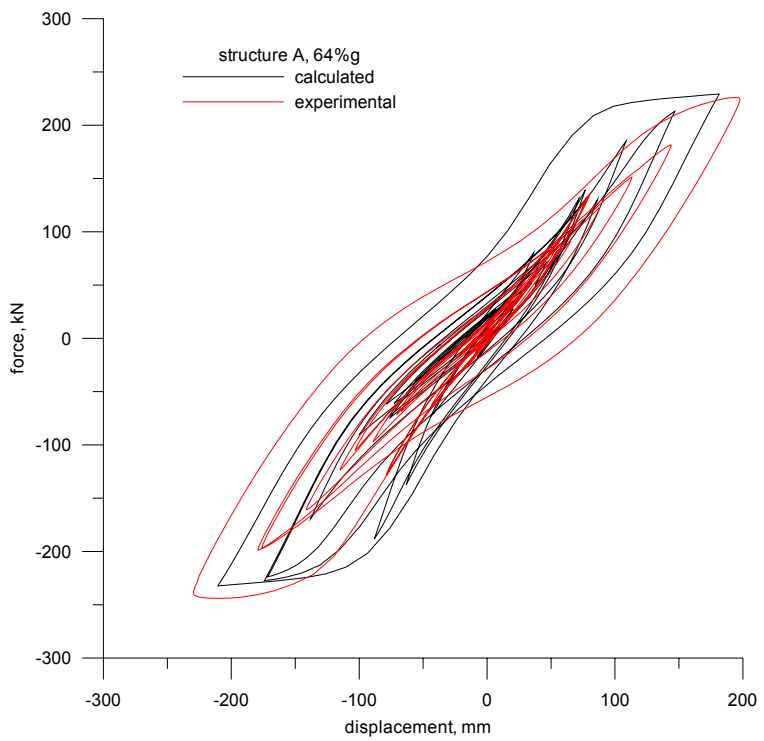

Figure 3.10 b. Hysteresis loop for PGA of 64% *g*

In Figures 3.11 a, b the calculated curvatures at the bottom and the top of column NC are compared with the experimentally obtained ones.

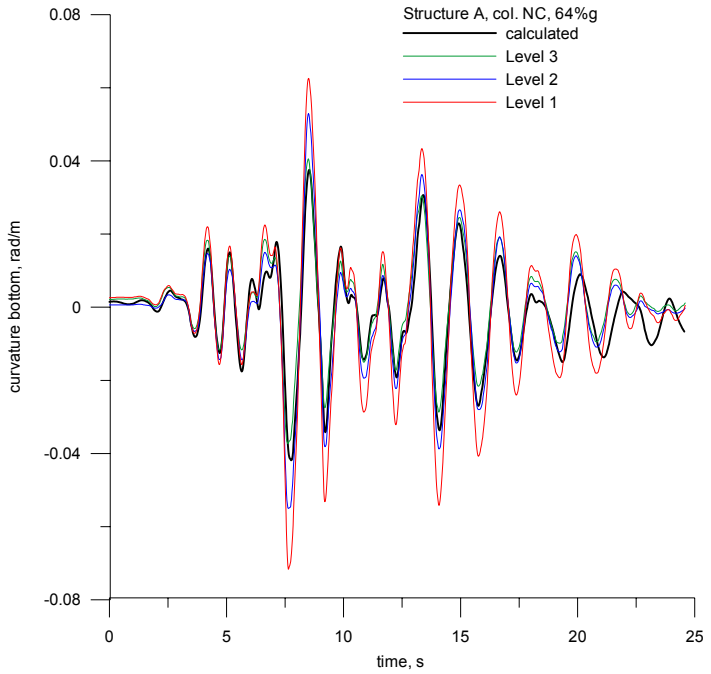

Figure 3.11 a. Curvatures at the bottom of column NC for PGA of 64% *g*

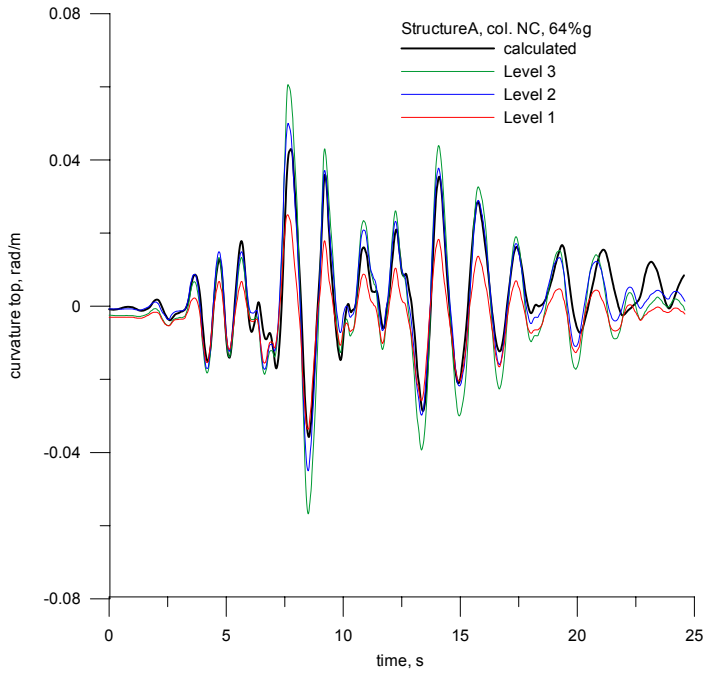

Figure 3.11 b. Curvatures at the top of column NC for PGA of 64% *g*

The calculated and experimental curvatures at the bottom and the top of column NW are shown in Figures 3.12 a, b.

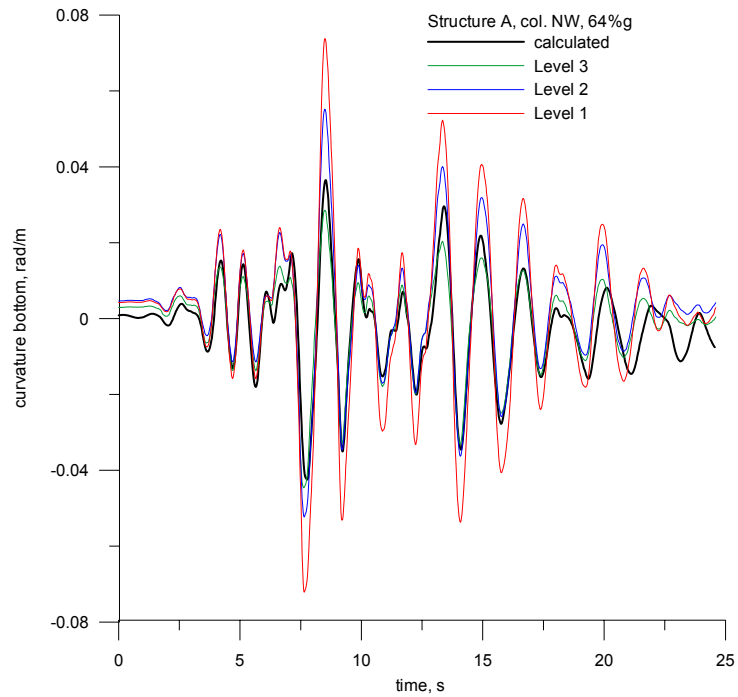

Figure 3.12 a. Curvatures at the bottom of column NW for PGA of 64% *g*

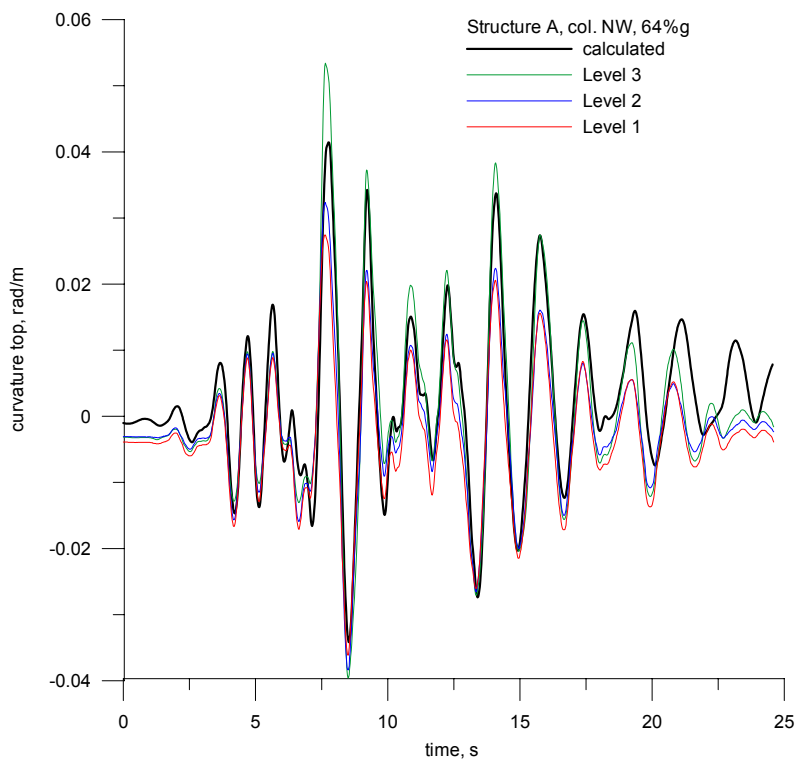

Figure 3.12 b. Curvatures at the top of column NW for PGA of 64% *g*

For the two considered columns the measured mean curvatures along the plastic hinge length at the top coincide relatively well with the calculated curvatures. The calculated curvatures at the top of the columns are smaller than the experimental curvatures along the plastic hinge length. This fact could be explained by a substantial bond deterioration in the beam-column joints which might have taken place during the test.

In Figure 3.13 a, b the calculated and the measured mean curvatures at Level 1 and Level 2 (see Figure 3.2) of the beam side NCW and NWE, respectively, are compared .

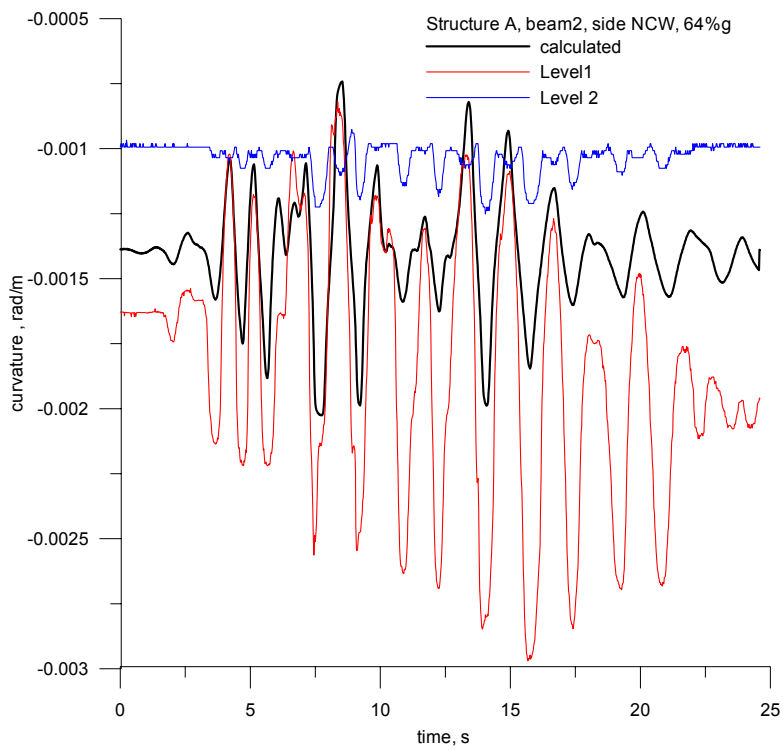

Figure 3.13 a. Curvatures at the site NCW of the beam for PGA of 64% *g*

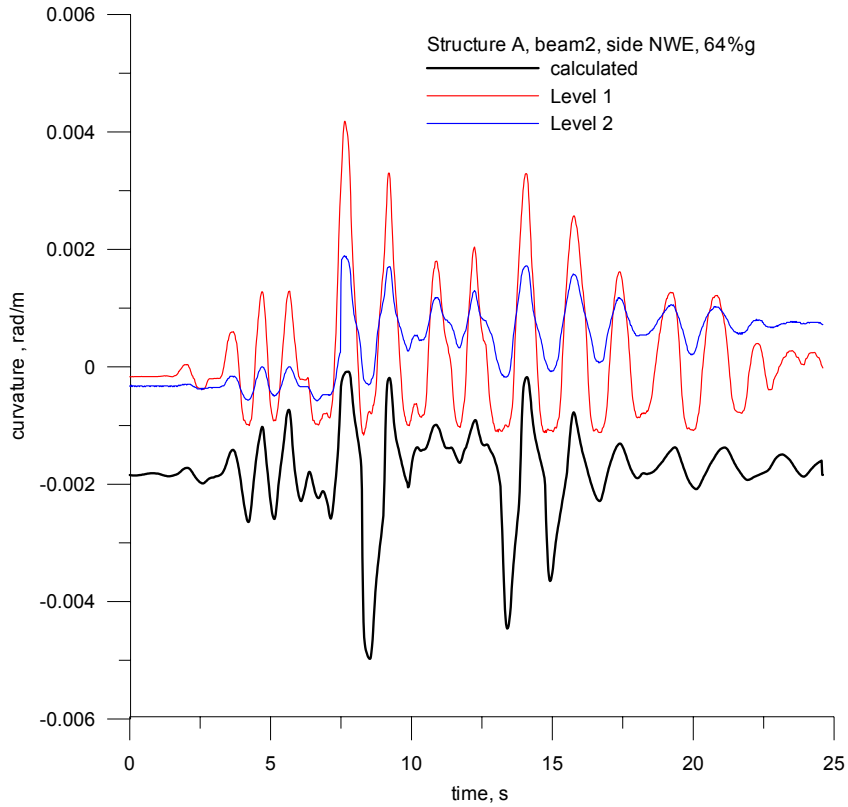

Figure 3.13 b. Curvatures at the site NWE of the beam for PGA of 64% *g*

As in the case of the test with PGA of 32%g, for the beam side NWE, where the bending moment was larger, the calculated curvature excursions show coincidence with the measured mean curvature excursions at Level 1. For the beam side NCW, where the bending moment is smaller, the measured mean curvature excursions at Level 1 differ significantly from the calculated ones. It should be noted that, despite the not good coincidence, both, the calculated and measured curvatures, show that the beam was in the elastic stage (φ_{yp} = 0.0187 rad/m) having considerable 'reserves' of strength.

3.3.4 Experimental test with PGA of 80% g

During this test, the maximum storey displacement was 6.8 % of the storey height. In spite of this large storey drift, no shear cracks or crushing of the concrete appeared. The flexural cracks in the columns resulting from the previous tests enlarged and new flexural cracks appeared over the height of the columns. No cracks become visible in the beams, and in the beam-column connections as well. The calculated displacement time history and base shear - storey displacement relationship shown in Figures 3.14 a, b coincide well with experimental ones.

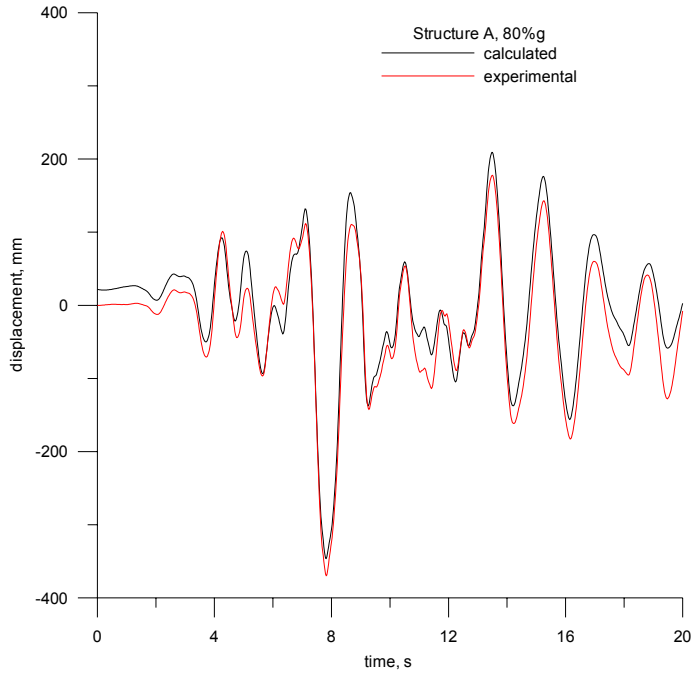

Figure 3.15 a. Displacement time history for PGA of 80% *g*

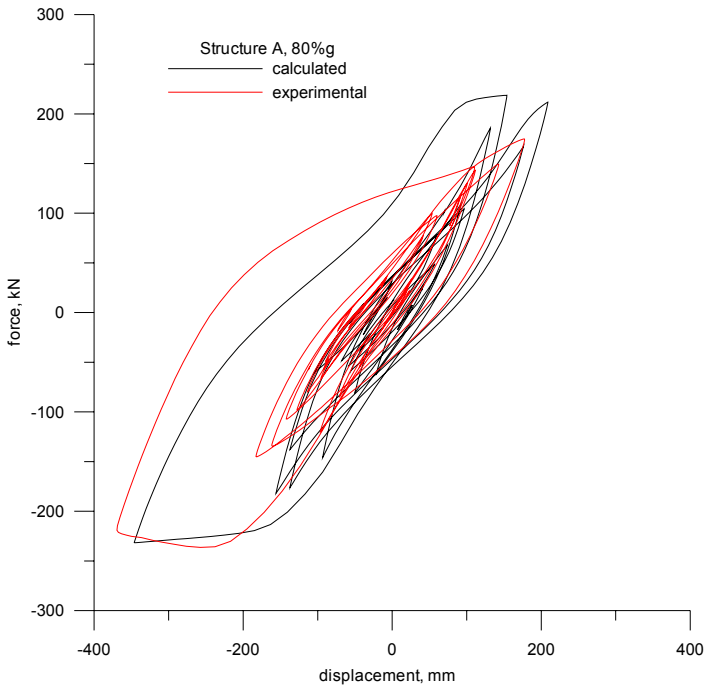

Figure 3.15 b. Hysteresis loop for PGA of 80% *g*

The measured mean curvatures at the top and bottom of the column NC are compared with experimental ones in Figure 3.16 a, b.

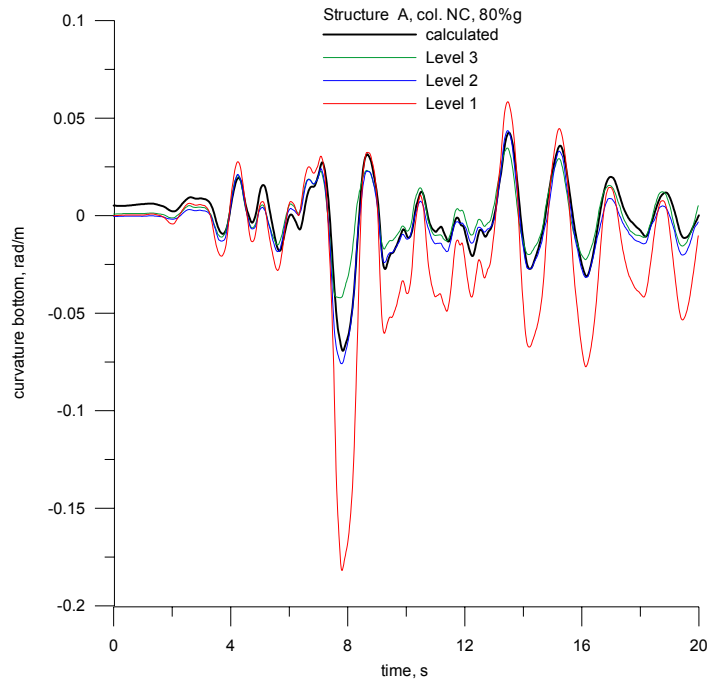

Figure 3.16 a. Curvatures at the bottom of column NC for PGA of 80% *g*

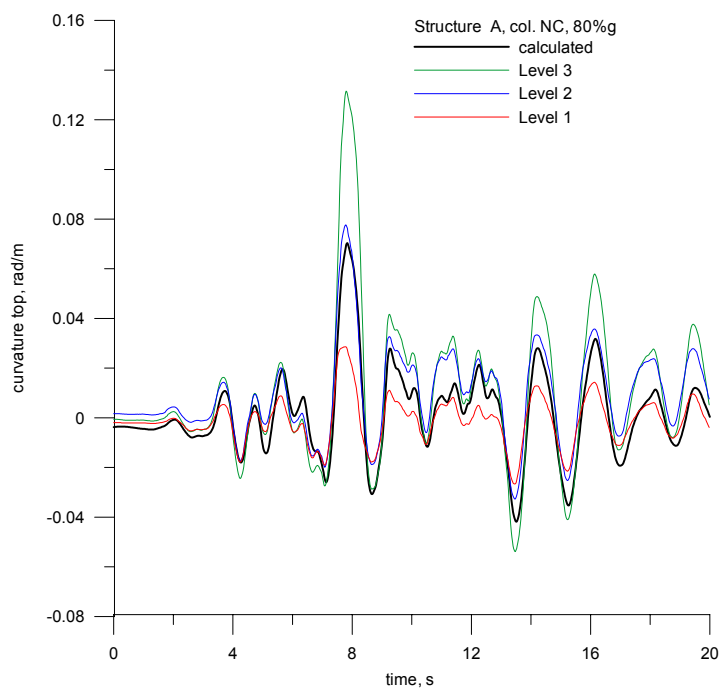

Figure 3.16 b. Curvatures at the top of column NC for PGA of 80% *g*

In Figures 3.17 a, b the experimental mean curvatures at the bottom and top of the column NW are compared with the calculated curvatures.

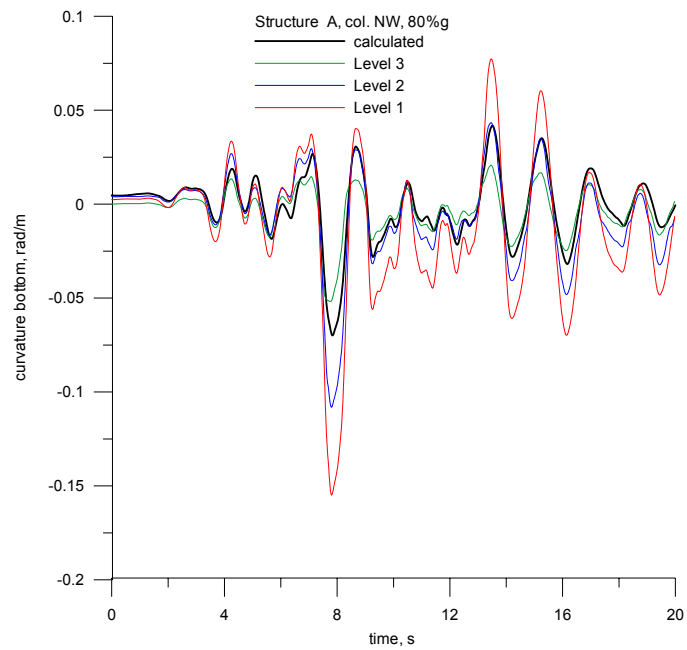

Figure 3.17 a. Curvatures at the bottom of column NW for PGA of 80% *g*

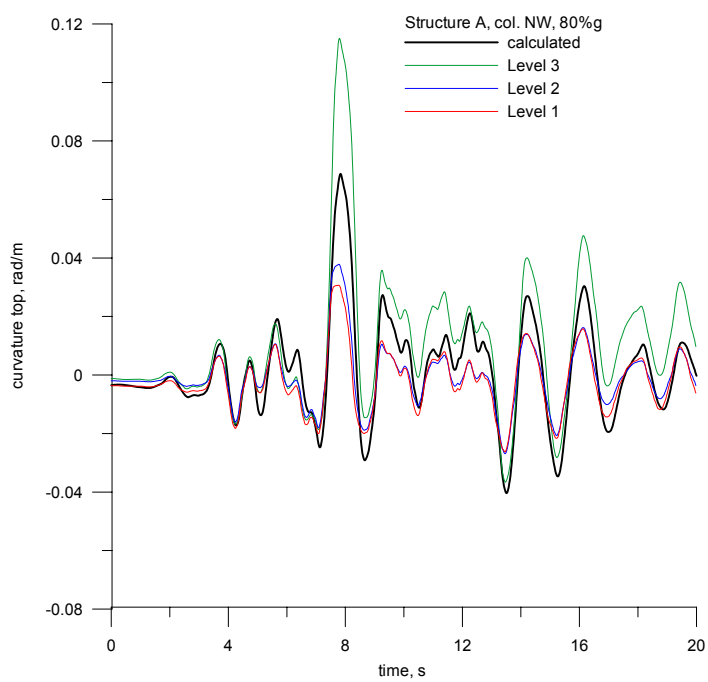

Figure 3.17 b. Curvatures at the top of column NW for PGA of 80% *g*

As it can be seen from Figures 3.16 a, b the mean curvatures measured above Level 2 agree well with the calculated curvatures at the top and bottom of column NC. For the bottom of column NW, the calculated curvatures coincide also with the mean curvatures measured above Level 2, except in the case of the maximum excursion (Figure 3.17 a). For the top of column NW, the calculated curvatures agree with the mean values of the measured mean curvatures along the plastic hinge length (Figure 3.17 b).

In Table 3.4 the maximum excursions of the measured curvatures during this test are presented.

Table 3.4. Measured maximum curvature excursions during the test with PGA of 80%*g*

		maximum curvature excursions (rad/m)		curvature ductility	
Position	Segment	central column (NC)	lateral column (NW)	central column (NC)	lateral column (NW)
Top	Level 1	0.0477	0.0507	1.77	2.03
	Level 2	0.0976	0.0568	3.61	2.27
	Level 3	0.159	0.134	5.89	5.36
Bottom	Level 1	0.214	0.195	7.93	7.80
	Level 2	0.0945	0.138	3.50	5.52
	Level 3	0.0649	0.0665	2.40	2.66

They show that during the imposed large storey drift demand (6.8 %), the plastic deformations were spread beyond the assumed 0.3m plastic hinge length. In this way the overall ductile behaviour of the structure was provided by spreading the ductility demands in larger parts of the members. This fact, as well as the overall structural behaviour during this test, prove that the detailing rules of Eurocode 8 for ductility class H fully comply with its requirement to 'enable the structure to develop stable mechanisms associated with large dissipation of hysteretic energy under repeated reversed loading, without suffering brittle failures'.

The large values of the maximum excursions of the measured curvatures prove considerable pull-out and push-in effects in the longitudinal reinforcement [18]. The longitudinal bars at the bottom of the columns were anchored at the bottom of the foundation (1.2 m deep), thus they had approximately two times larger a maximum slippage length L_{cs} ([11], see also section 3.1) than at the top of the column, where they were anchored at the level of the top of the beam (0.6 m deep). In this way the larger maximum slippage length L_{cs} generated larger curvature excursions at Level 1 at the bottom of the columns (see Table 3.4), than at Level 3 at the top of the columns.

At the bottom part of the columns the pull-out and push-in effects in the longitudinal reinforcement were more intensively spread along the instrumented part of column NW (maximum measured curvature excursion of 0.138 rad/m at Level 2), than along the instrumented part of column NW (maximum measured curvature excursion of 0.0976 rad/m at Level 2). This fact could be related to the positive effect, which the larger axial force in the central column (NC) plays in suppressing the pull-out of the longitudinal reinforcement in the end of the column fixed to the foundation. In the ends of the columns framing to the beam the maximum measured curvature excursions at Level 2 were much smaller than those at Level 3 (see Table 3.4). Consequently, in the ends of the columns framing in the beam-column joint, the pull-out and push-in effects in the longitudinal reinforcement were spread mainly in the upper half of the plastic hinge and did not relate strongly the magnitude of the axial force.

In Figures 3.18 a, b the calculated and the measured mean curvatures at Level 1 and Level 2 of the beam side NCW and NWE, respectively, are compared .

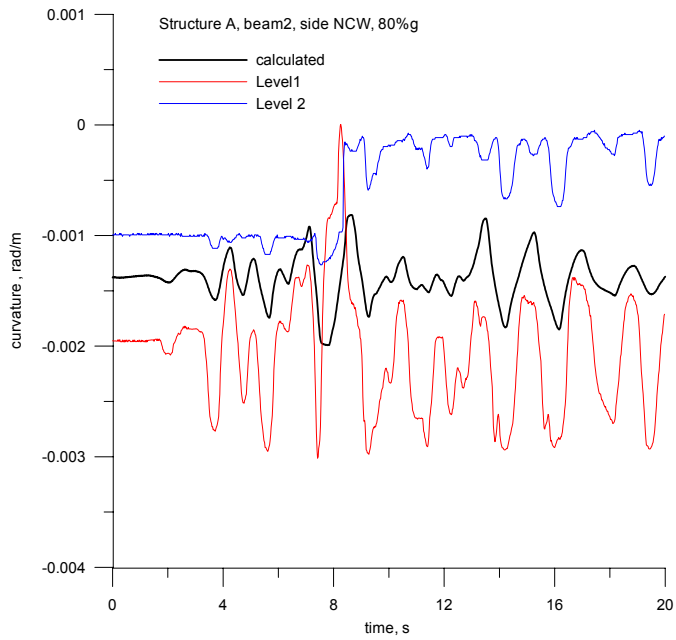

Figure 3.18 a. Curvatures at the site NCW of the beam for PGA of 80% *g*

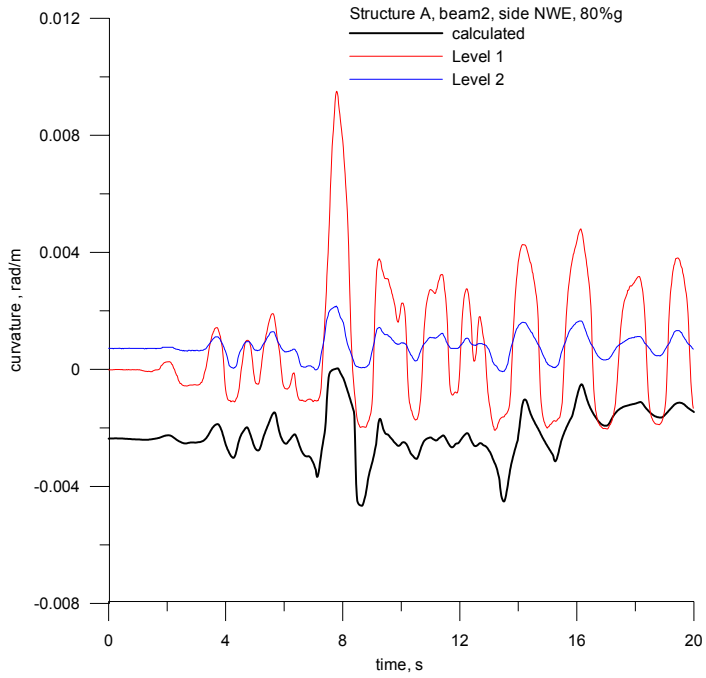

Figure 3.18 b. Curvatures at the site NWE of the beam for PGA of 80% *g*

Similarly to the case of test with PGA of 64% *g*, there is not good coincidence between the measured and calculated curvatures at the ends of the instrumented beam. The calculated curvatures relate the mean value of the curvatures measured at Level 1 and Level 2. Both the calculated and measured curvatures give a qualitative estimate of the non-yielded state of the beam, since they do not exceed the calculated yielding curvature (φ_{yp} = 0.0187 rad/m).

3.3.5 Agreement between the experimental and calculated response

As it can be seen from the above presented comparisons between the experimental and calculated responses, the calculated overall characteristics of the structural response, such as the displacement time history and the relationship base-shear – storey displacement coincide very well with experimental ones. At the same time the 'local' response characteristics, such as the curvatures, do not show good coincidence for all the tests. The larger values of the measured curvatures with respect to the calculated ones during the time intervals of largest responses could be explained by the following reasons:

(i) the inclusion of the effects of shear distortion of the shear span and the fixed-end rotation due to slippage in the yielding curvature is not sufficient to account for these effects under higher intensity of the seismic excitation. This fact is confirmed by the good coincidence between the measured and calculated curvatures for the seismic excitation with PGA of 32%g. For the tests with larger values of PGA the measured curvatures are much larger than the calculated ones. These larger values are most probably caused by the bond deterioration inside the joint cores, which requires more refined modelling of the non-linear seismic response of the structural members, than the use of the fibre model for moment-curvature characteristics in the plastic hinge, as shown in [19].

(ii) As noticed also in [18], the nominal curvature measured over the plastic hinge length satisfactorily coincide with the one computed by means of the fibre models. The zones adjacent to the beam-column or beam-foundation joints are subjected to a strain 'interference' due to the deformation of the adjacent elements. This statement could be supported by the measured relative displacements at the top of the column NW. On the west side of the column the upper transducer was not fixed to the beam, so formally there are no reasons to correct these data, as done with the data from the transducer on the east side of the column. In Figure 3.19 the mean curvatures obtained by correcting the data on the two sides of the upper segment (Level 3), the curvatures obtained by correction only of the data on the east side and the calculated curvatures are compared.

The double negative curvatures when the data of the West side are not corrected, prove the existence of considerable deformations on the West side of the upper segment, which are induced by the deformations of the beam. Also, the lateral force F_y, which causes yielding in the frame, could be approximately computed as [3]:

$$F_y = \sum 2M_{yi} / l_e \qquad (3.3)$$

where:

M_{yi} is the yielding moment for the *i-th* column,
l_e is the effective length of the column.

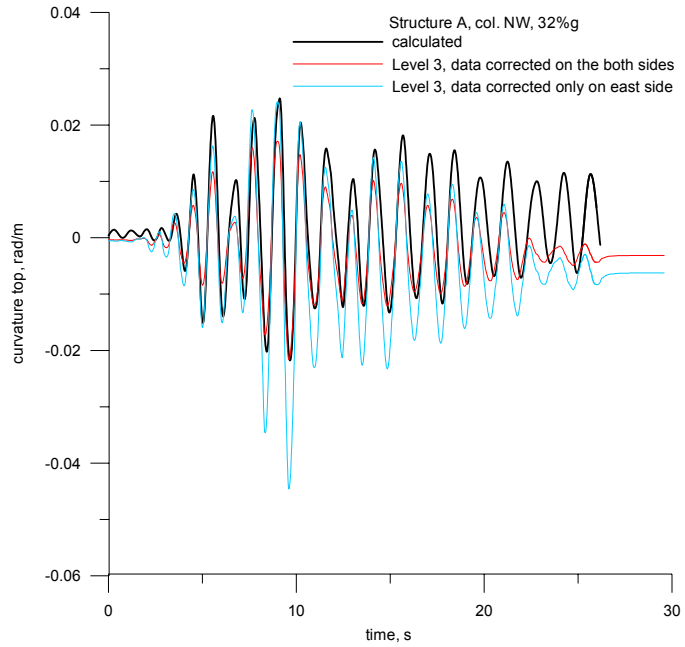

Figure 3.19. Curvatures obtained by different correction of data for the top of column NW

By using the yielding moments corresponding to the actual material properties (shown in Table 3.1) and l_e = 5.45 m, F_y is estimated as 214.7 kN. As depicted in Figure 3.6 b, the maximum base-shear measured during the experiment with PGA of 32% g is 218.8 kN, which corresponds to the onset of yielding. In this way it would be impossible to develop in column NW curvatures far beyond φ_{yp} = 0.025 rad/m (see Table 3.1). Moreover, the maximum curvature calculated when the data of the West side are not corrected is 0.0446 rad/m, *i.e.* it justifies a pronounced yielding at the top of the column, something which contradicts the maximum base-shear measured during the experiment. This fact confirms the above statement about the strain 'interference' due to the deformations of the adjacent element.

Although the not good coincidence between measured and calculated curvatures for all the tests, a good agreement between the experimental and calculated displacement time histories and base-shear – storey displacement relationships was reached by exploiting the capabilities of the smooth hysteresis model [13]. The choice of appropriate parameters describing the stiffness and strength degradation, the elastic-yield transition, the shape of unloading and the slip gave the possibility of creating structural models which describe well the overall characteristics of the structural response at all the levels of the imposed seismic intensity.

3.4 Evaluation of the displacement ductility supply and of the behaviour factor

3.4.1 Estimation of structural ultimate capacity

In Figure 3.20 the envelope of the base-shear – storey displacement relationships recorded during the experimental tests is shown.

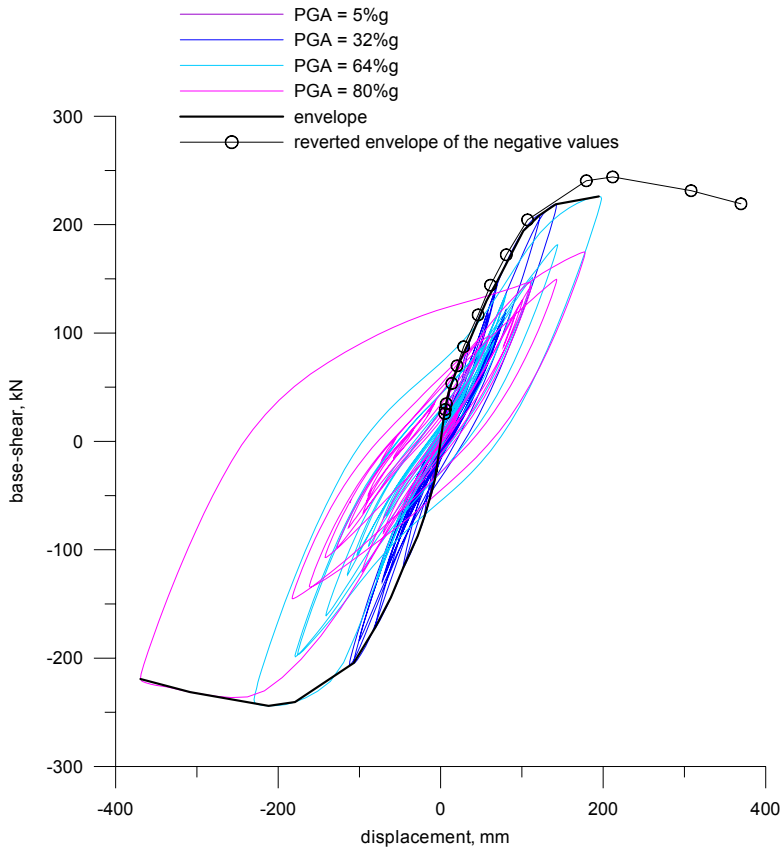

Figure 3.20. Envelope of the recorded hysteretic loops

As it can be seen from the hysteresis loops recorded during the tests with PGA of 64% g and 80% *g*, during the imposed seismic excitations the structure exhibited only one large hysteretic loop. The lack of high amplitude cycling in the structural response can be explained mainly by the following reasons:

(i) the duration of the active part of the seismic excitation was relatively short (strong motion effective duration of 9.2 s according to Trifunac-Brady [20]);

(ii) the seismic response of such slender structure was considerably influenced by the P-delta effects and it exhibited asymmetric hysteretic loops with negative slope and a preferential direction of inelastic response [21], as it can be seen in Figure 3.20 for the test with PGA of 80% g.

Due to the lack of cycling during the applied seismic excitations there was little strength degradation and the obtained envelope curve did not provide an estimate of the ultimate structural displacement. Experimental data for the structural behaviour under cycling with large displacements were obtained from an additional test with the displacement excitation with increasing amplitude shown in Figure 3.22 a.

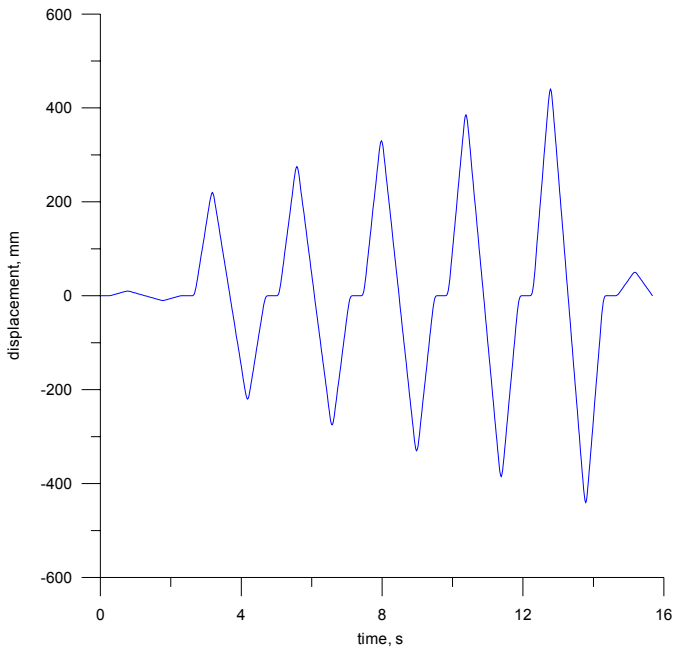

Figure 3.21 a. Displacement time history of the additional excitation

In Figure 3.21 b the recorded hysteretic loop is shown, which exhibits considerable strength degradation during the last two cycles.

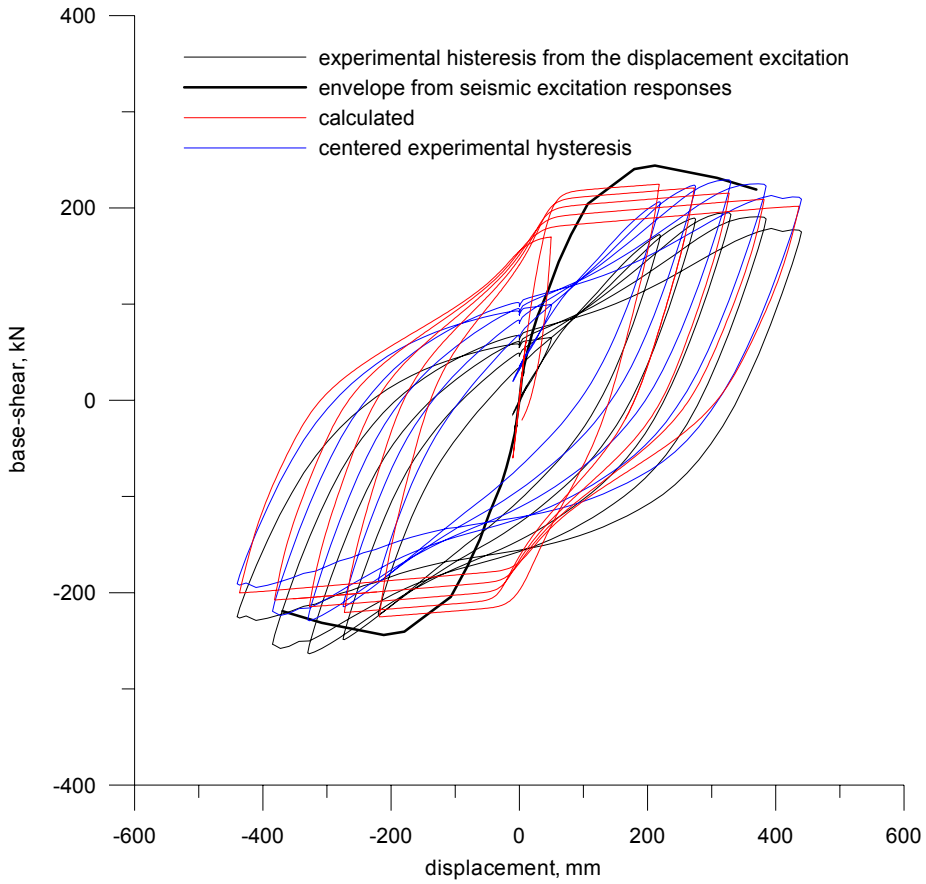

Figure 3.21 b. Experimental and simulated hysteresis loops for the displacement excitation

Despite the imposed large displacements (8.1% storey drift) no visual evidences of the failure of the structural members (such as crushing of the concrete or buckling of the longitudinal bars) were observed. The comparison of the recorded hysteresis with the envelope from the seismic excitation tests (Figure 3.21 b) shows the shifting of the hysteresis loops down due to the inelastic deformations accumulated during the seismic excitations. Because of this, it is impossible to use directly the experimental results from the displacement cyclic test for the estimation of the ultimate capacity.

The numerical simulation of the dynamic behaviour of the structure under the displacement excitation starting from the non-cracked initial conditions (see Figure 3.21 b) demonstrated that in such a case it would exhibit symmetric hysteretic loops and no failure of the structural members will occur. This fact gave reasons to take into account this experimentally recorded hysteretic loop for a more accurate determination of the envelope curve by eliminating the effect of the inelastic deformations accumulated during the seismic excitations. Since during one cycle the positive amplitude of the displacement excitation equals the subsequent negative amplitude, the hysteresis was 'centred' by supposing that the maximum positive and negative base-shears under equal displacements should be equal. The experimental hysteresis loops shifted in this way agree very well with the calculated ones, as shown in Figure 3.21 b.

The resulting capacity curve (envelope curve of the base-shear – storey displacement relationship), obtained by use of all the experimental data is shown in Figure 3.22.

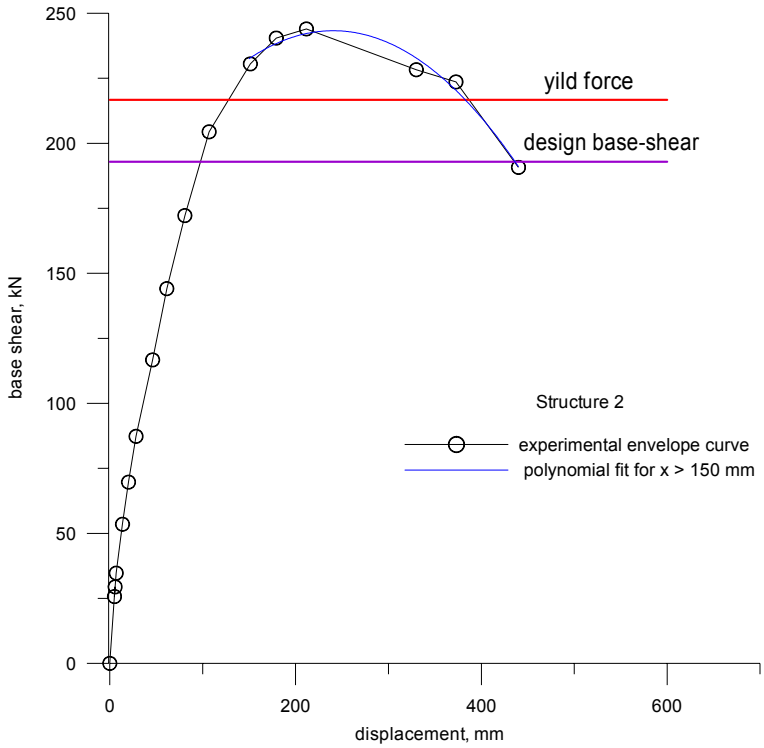

Figure 3.22. Capacity curve of Structure A

As shown in Figure 3.22, for storey displacements larger than 150 mm the data points are fitted by the equation:

$$F(x) = -0.00131x^2 + 0.631x + 167.39 \qquad (3.4)$$

where:

F is the base-shear in kN,
x is the storey displacement in millimetres.

The ultimate storey displacement x_u is determined as corresponding to a 15% drop of the peak base-shear force [16, 22, 23]. This definition is in agreement with the provisions of Eurocode 8 for the determination of the plastic rotation capacity of the R/C members. Since the experimentally measured maximum base-shear force F_{max} is 244 kN, from Eq.(3.4) x_u is calculated as 0.408 m.

The ultimate displacement was also estimated by use of empirical formulae for the ultimate chord rotation of RC members in terms of their geometric and mechanical characteristics. In Eurocode 8, part 3 [10] and in the new Italian code [15], the ultimate chord rotation θ_u is estimated as:

$$\theta_u = a_{st}(1-0.38a_{cyc})(1+\frac{a_{sl}}{1.7})(1-0.37a_{wall})(0.3^{\nu})\left[\frac{\max(0.01,\omega')}{\max(0.01,\omega)}f_c\right]^{0.2}\left(\frac{L_s}{h}\right)^{0.425} 25^{(\alpha\rho_{sx}\frac{f_{yh}}{f_c})}(1.45^{100\rho_d}) \quad (3.5)$$

where:

a_{st} is the coefficient for the type of steel, being equal to 0.016 for heat-treated (tempcore) steel,
a_{cyc} equals 1 for cyclic deformation,
a_{sl} is the coefficient for slip equal to 1 if there is slippage of the longitudinal bars from their anchorage beyond the section of maximum moment,
a_{wall} is zero for beams and columns and equals 1 for walls,
$\nu = N / A_g f_c$ is the axial force normalized to the product of the gross cross-sectional area of the concrete A_g and the strength of the concrete f_c,
ω and ω' are the mechanical reinforcement ratios, $\frac{\rho f_y}{f_c}$, of the tension and compression reinforcement, respectively, in which ρ is the ratio of the area of the tension or compression reinforcement and f_y is the yield strength of the reinforcement,
$L_s / h = M / Vh$ is the shear span ratio in the member end, in which M and V are the moment and shear force in the member end and h is the depth of the member cross-section,
α is the confinement effectiveness factor [16], defined as:

$$\alpha = \left(1-\frac{s_h}{2b_c}\right)\left(1-\frac{s_h}{2h_c}\right)\left(1-\frac{\sum b_i^2}{6h_c b_c}\right) \quad (3.6)$$

with b_c and h_c the width and depth of the confined core, respectively, b_i the distances between the longitudinal bars laterally restrained by at stirrup corners or by 135 degree hooks and s_h the spacing of the transverse reinforcement,
$\rho_{sx} = A_{sx} / b_w s_h$ is the ratio of the transverse steel parallel to the direction x of loading in which b_w is the width of the web,
f_{yh} is the yield stress of the transverse steel,
ρ_d is the steel ratio of the diagonal reinforcement in each diagonal direction.

Using a database of more than 1000 tests on specimens, representative for various types of RC members, Panagiotakos and Fardis [16] developed the following expression for the ultimate chord rotation θ_u

$$\theta_u = a_{st,cyc}(1+0.5a_{sl})(1-0.4a_{wall})(0.2^{\nu})(f_c)^{0.175}\left(\frac{L_s}{h}\right)^{0.4} 1.1^{(100\alpha\rho_{sx}\frac{f_{yh}}{f_c})}(1.3^{100\rho_d}) \quad (3.7)$$

where:

$a_{st,cyc}$ is the coefficient for the type of the steel equal to 1.125 for hot-rolled ductile steel, 1.0 for heat-treated (tempcore) steel and 0.8 for cold-worked steel,
all other denotations are similar to those of Eq. (3.5).

In Table 3.5 the ultimate chord rotations and ultimate storey displacements calculated according Eq. (3.5) and Eq.(3.7) are presented.

Table 3.5. Ultimate chord rotations and storey displacements

	Eurocode 8 and Italian code		Panagiotakos and Fardis	
	θ_u	x_u, m	θ_u	x_u, m
lateral columns	0.0784	0.427	0.0838	0.456
central columns	0.0755	0.412	0.0797	0.434

The results obtained show that the ultimate limit state is defined by the failure of the central columns. The x_u = 0.412 m calculated according to Eurocode 8 [10] and the new Italian code [15] is in a very good agreement with the experimentally determined one (1% difference). The ultimate storey displacement x_u = 0.434 m according to [16] relates well with the experimental ultimate storey displacement under the assumption of 20% decrease of the peak base-shear force, which, according to Eq.(3.4) is 0.433 m. In this way, the results from the empirical formulae provide an estimation of the ultimate state, which is very close to the experimental results. They could be recommended for validation of the results from the push-over and non-linear time history analyses.

3.4.2 Evaluation of the yield displacement

The storey displacement x_{1y} corresponding to the first yielding in the structure was estimated from the experimental data by use of the strains in the longitudinal reinforcement of the columns. The mean strains were obtained from the records of the relative displacements along the instrumented segments. These strains were corrected for the depth of the concrete cover. The tension strain in the longitudinal bars ε_{1y} corresponding to the first yield was calculated by use of the Eq. (3.2) under the assumption that the shear and the pull-out effects are concentrated along the plastic hinge length, as:

$$\varepsilon_{1y} = \varepsilon_y + \frac{0.25\varepsilon_y d_b f_y}{L_p\sqrt{f_c}} + \frac{0.0025(d-d')}{L_p} \qquad (3.8)$$

where

L_p = 0.3 is the plastic hinge length,

the other denotations are given in section 3.2.

The tension strain in the longitudinal bars ε_{1y} = 0.00705 calculated from Eq.(3.8) is compared to the strains measured during the test with PGA of 32% *g*. In Figures 3.23 a and 3.24 b the mean strains measured at the bottom of columns NW and NC, respectively, are shown. The mean strains measured at the top of columns NW and NC are not presented, since in all the segments they are substantially smaller than ε_{1y}.

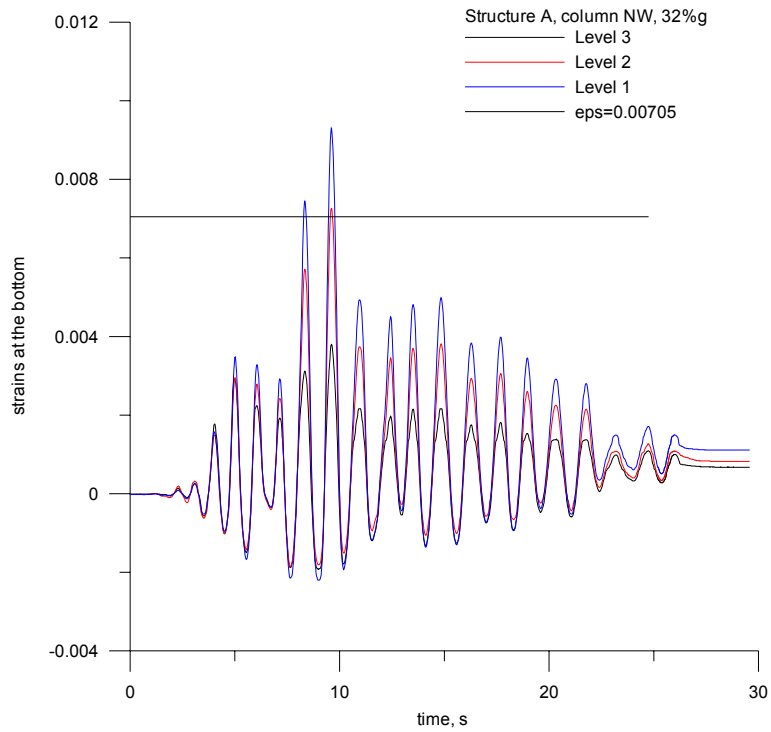

Figure 3.23 a. Mean strains at the bottom of column NW

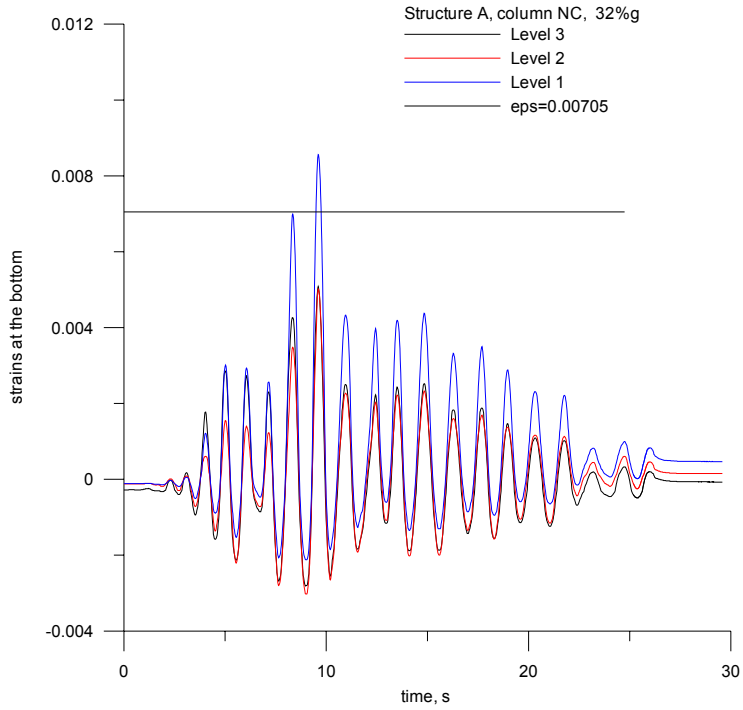

Figure 3.23 b. Mean strains at the bottom of column NC

The time point of the first yielding was estimated from the condition that the mean tension strains at Level 2 reach ε_{1y}. The mean strains in the segment closer to the joint are not considered due to the considerable influence of the deformations of the adjacent element, as discussed in section 3.3.5. As it can be seen from the above figures, only the lateral columns reach the first yielding at PGA of 32% *g*. The mean strains in the segment at Level 2 reach ε_{1y} for t = 9.56 s. At this time the recorded storey displacement is x_{1y} = 0.131 m and the recorded base shear corresponding to the first yielding is F_{1y} = 214 kN. There is a good agreement between F_{1y} and the yielding force estimated from the calculated yielding moments (see section 3.3.5) F_y = 214.7 kN. F_y is a little larger because it was determined under the assumption that all the columns reach the yielding simultaneously.

Yield displacements according to the criteria for the reduced stiffness equivalent elasto-plastic yield [23] (shown in Figure 3.24 a) and equivalent elasto-plastic energy absorption [23, 9] (shown in Figure 3.24 b) are applied to the experimental envelope of the base-shear – storey displacement relationship and shown in Table 3.6. These criteria are widely used for the estimation of the yield displacement from the experimental data when no special instrumentation is supplied for estimation of the deformations in the structural members. The present experimental study gives the possibility to calibrate them.

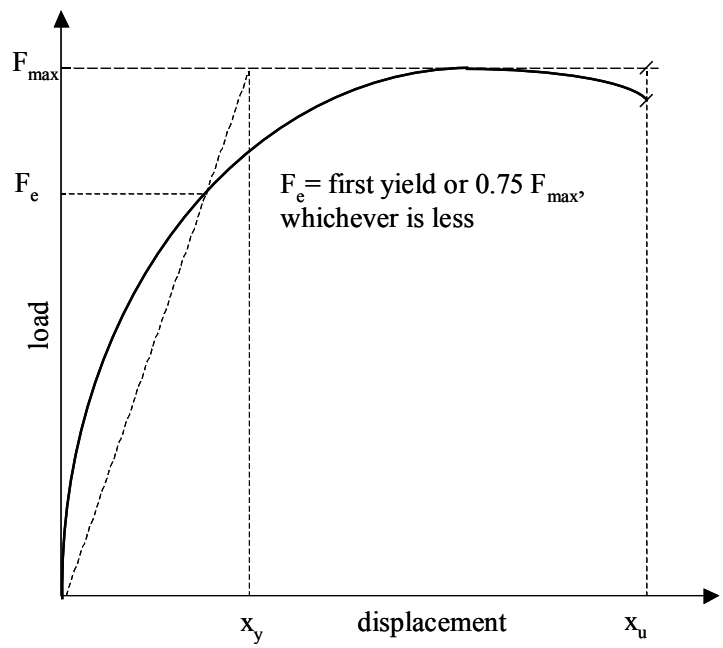

Figure 3.24 a. Reduced stiffness equivalent elasto-plastic yield

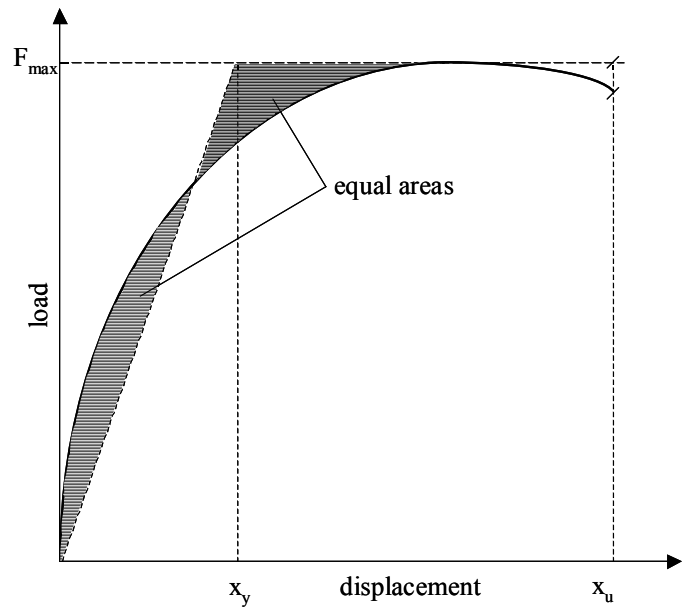

Figure 3.24 b. Equivalent elasto-plastic energy absorption

In Table 3.6 the yield displacements obtained from the experimental data are compared to the yield displacement obtained from the chord rotation at yield [15, 16], as specified by Eq. (3.2).

Table 3.6. Yield displacements and displacement ductility supplies

	method	x_y, m	F_y, kN	x_u, m	μ_δ
Experimental	x_y as first yield displacement.	0.131	214	0.408	3.11
	x_y from the equivalent elasto-plastic yield.	0.120	244	0.408	3.42
	x_y from the equivalent elasto-plastic energy absorption.	0.117	244	0.408	3.48
Use of formulae for θ_u and θ_y	Eurocode 8 and Italian code.	0.143	-	0.412	2.87
	Panagiotakos and Fardis.	0.143	-	0.434	3.03

As it can be seen from Table 3.6, the obtained experimental first yield displacement is larger than the experimental yield displacements estimated by use of the criteria for the equivalent elasto-plastic yield (8% difference) and the equivalent elasto-plastic energy absorption (11% difference). In this way, these criteria underestimate the capacity of the considered structure at yield. Alternatively, the yield displacement estimated from the chord rotation at yield overestimates by 9% the capacity of the considered structure at yield.

3.4.3 Ductility supply of the structure

The displacement ductility supply μ_δ of the structure is estimated as

$$\mu_\delta = x_u / x_y \qquad (3.9)$$

In Table 3.6 the experimentally obtained value of $\mu_\delta = 3.11$ is compared with the ductility supplies obtained by the other considered methods. The ductility supplies calculated from the experimental data by use of the criteria for the reduced stiffness equivalent elasto-plastic yield [23] and equivalent elasto-plastic energy absorption [23, 9] give a little larger estimate due to above discussed underestimation of the yield capacity of the considered structure. The implementation of the formulae in Eurocode 8 [10] and the new Italian Code [15], and Panagiotakos and Fardis [16] chord rotations at yield and at the ultimate provide slight conservative, but well coinciding with the experimental result estimates.

It should be noticed that the experimental structure is detailed for ductility class H and constructed under strict quality control. Also, no deficiencies in the construction were observed during the experimental testing. In this way the detailing and execution comply fully with the requirements of Eurocode 8 for ductility class H. According Eurocode 8, for structures with fundamental period $T > T_c$ (see section 2) the displacement ductility factor μ_δ corresponds to the basic value q_0 of the behaviour factor. For the considered structure the ductility demand according to Eurocode 8 is $q_0 = 4.95$ for ductility class H. However, the experimentally estimated displacement ductility supply is 3.11. A similar problem is discussed in [24], when comparing the displacement ductility supplies of two regular frame RC structures (12-story structure designed according to Eurocode 8 and 7-story structure designed according ATC [25]) with the corresponding code demands. The displacement ductility supplies calculated by means of sophisticated inelastic analyses were 22% and 10% smaller than the corresponding ductility demands and only the measured values of overstrength ensured the adequate seismic performance of the structures.

During the displacement excitation test presented in section 3.4.1 no relative displacements were recorded and therefore the curvature ductility supplies of the structural members cannot be estimated directly. In Table 3.4 the curvature ductility factors for the seismic excitation with PGA of 80% *g*, obtained on the basis of the experimental maximum curvature excursions and the yield curvatures used in the numerical model (see Table 3.1) are presented. Supposing that at this excitation the structure is close to its ultimate limit state, the curvature ductility factors reported in Table 3.4 could be considered as a lower bound of the curvature ductility factor supply. Having in mind the relationship between the local and global ductility factors for the

considered structure [26] as $\mu_\varphi = 2\mu_\delta - 1$ and the measured displacement ductility supply μ_δ = 3.11, the required minimum curvature ductility supply is μ_φ = 5.22. As it can be seen from Table 3.4, the curvature ductility measured in the segments complies with this requirement closer to the joints.

3.4.4 Behaviour factor supply

In the force-based seismic design methods the behaviour factor q is a force-reduction factor used to reduce the elastic response spectrum to obtain the inelastic response spectrum. According to Eurocode 8 'the behaviour factor q is an approximation of the ratio of the seismic forces that the structure would experience if its response was completely elastic with 5% viscous damping, to the minimum seismic forces that may be used in design – with a conventional elastic analysis model – still ensuring a satisfactory response of the structure'. This definition implies [22, 25]:

$$q = \frac{F_{el}}{F_d} = \frac{F_{el}}{F_y}\frac{F_y}{F_d} = q_\mu q_s \qquad (3.10)$$

where:

F_{el} is the 'would-be' base-shear force obtained by linear elastic analysis,
F_d is the design base-shear strength,
F_y is the yield base-shear force,
q_μ is the ductility dependent component of the behaviour factor,
q_s is the overstrength-dependent component of the behaviour factor.

For the considered structure with experimentally estimated fundamental period T_{1A} = 0.69 s ($T_{1A} > T_c$ for subsoils of classes A, B, C and E) Eurocode 8 prescribes the equal displacements approximation of the behaviour factor. The concept of this approach is shown schematically in Figure 3.24.

According to this approach $q_\mu = \mu_\delta$= 3.11 and the behaviour factor supply is q = 3.45 taking into account the design base-shear strength F_d = 192.9 kN [3]. Consequently, to meet the Eurocode 8 behaviour factor demand of q = 4.95, an overstrength factor q_s of 1.59 is needed. Since the experimentally estimated yield force is F_y = 214 kN, the design seismic force E_d should be $E_d = = F_y/ q_s$ = 134.56 kN. Having in mind the normalized spectral value of the experimental accelerogram $Sa\ (T = 0.69)/a_g$ =1.77, the considered structure would sustain the experimental excitation with PGA = a_g = 0.53 g. This value contradicts the perfectly ductile seismic behaviour of the structure observed during the test with PGA of 80% g.

The reason for this contradiction remains with the adoption of the secant stiffness at yield as initial stiffness of the structure when estimating the behaviour factor supply. As it can be seen from Figure 3.25, the lower the initial stiffness, the lower the 'would-be' base-shear force obtained by linear elastic analysis and the lower the estimated behaviour factor supply. In this way the behaviour factor supply is strongly dependent on the initial stiffness of the structure, which is much larger than the secant stiffness at yield.

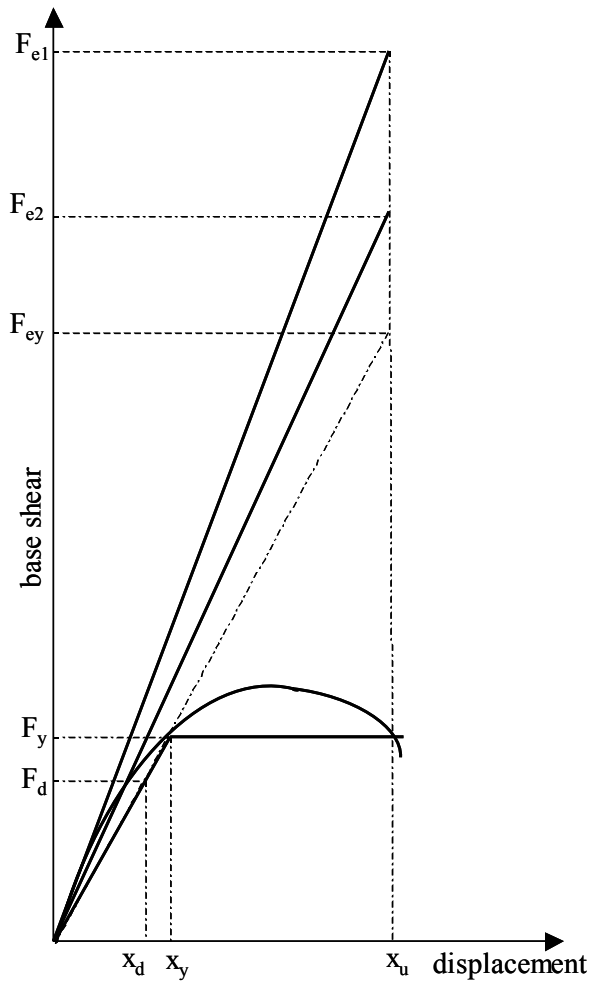

Figure 3.25. Equal displacements approximation of the behaviour factor

The behaviour factor supply is estimated by direct use of the Eurocode 8 definition, *i.e.* as

$$q = \frac{F_{el}}{F_d} \qquad (3.11)$$

The numerical simulation with the model built for the experiment with PGA of 80% *g* shows that the structure will reach the ultimate displacement x_u = 0.408 m at PGA of 87% *g*. Using the acceleration response spectrum of the experimental accelerogram for PGA of 87% *g*, the 'would-be' elastic base-shear forces F_{el} are calculated for the experimental initial stiffness k_e, for the initial stiffness k_d corresponding to the initiation of yielding of the reinforcement adopted in [3] and for the secant stiffness at yield k_y. Their values and the corresponding fundamental periods of the structure, the normalized spectral values of the experimental accelerogram and the behaviour factor supplies obtained from Eq.(3.11) are shown in Table 3.7.

Table 3.7. Behaviour factor supplies calculated from different initial stiffnesses

initial stiffness	fundamental period T, s	$Sa\ (T)/a_g$	F_{el}, kN	q
k_e = 5943 kN/m	0.69	1.77	1108	5.75
k_d = 2747 kN/m	1.01	1.26	789	4.09
k_y = 1634 kN/m	1.33	0.87	545	2.82

The results obtained show that only the consideration of the initial experimental stiffness k_e, which corresponds to the initiation of cracking (see Figure 3.4 a) gives the possibility of matching the behaviour factor demand in Eurocode 8. Consequently, the reduction of the design seismic loading due to underestimation of the structural stiffness leads to considerable decrease of the behaviour factor supply of the structure, which, as shown above, is dependent on its initial stiffness. In this context, when defining the structural model according to the prescriptions of Eurocode 8 concerning:

(i) designation of some structural members as 'secondary',

(ii) elimination of the contribution of the infills to the stiffness of the structure,

(iii) implementation of stiffness of the lateral load bearing elements, which corresponds to the initiation of yielding of the reinforcement,

the stiffness of the structure will be underestimated considerably, which might turn result into a significant underestimation of the design seismic loading and the corresponding behaviour factor supply.

3.5. Vulnerability analysis

3.5.1 Numerical formulation

The study is based on the use of reliability index, as first proposed by Kanda [27, 28] and developed by Hirata *et al.* [29,30,31]. The safety margin *Sf(y)* of a seismic response parameter *S(y)* with seismic capacity *R* for a given seismic intensity *y* is defined as:

$$Sf(y) = R / S(y) \qquad (3.12)$$

Under the assumption that *R* and *S* are log-normally distributed, the fragility (*i.e.* the conditional probability of failure) *Pf(y)* at any non-exceedance probability level *Q* following Kennedy and Ravindra [32] can be expressed as:

$$Pf(y) = \Phi\left(\frac{ln[Sm(y)/Rm] + \beta us\Phi^{-1}(Q)}{\beta z}\right) \qquad (3.13)$$

where:

Φ is the cumulative function of standard normal distribution;

Φ^{-1} is the inverse of the standard normal cumulative distribution function;

$S_m(y)$ and R_m are the median values of the seismic response *S(y)* and seismic capacity *R*, respectively;

$\beta z = \sqrt{\beta r^2 + \beta s^2}$;

in which βr and βs are the lognormal standard deviations of *R* and *S(y),* respectively,

β_{us} is the uncertainty in the median value of the capacity R_m that arises due to limitations in data and approximating in modeling.

Using Eq. (3.13) one can obtain a family of fragility curves corresponding to different non-exceedance probability levels *Q*. When there is no need to separate explicitly the uncertainty from the underlying randomness, the so-called 'total' [33] or 'composite' [32] variablity β_c is defined as:

$$\beta c = \sqrt{\beta z^2 + \beta us^2} \qquad (3.14)$$

The implementation of β_c instead of β_z provides a single fragility curve described as

$$Pf(y) = \Phi\left(\frac{lnSm(y) - lnRm}{\beta c}\right) \qquad (3.15)$$

3.5.2 Fragility estimation

The maximum storey drift was considered as a seismic response parameter, since it relates directly the ultimate limit state defined by the ultimate storey displacement x_u. The

seismic response parameter was calculated for seismic excitations compatible with the response spectrum of the experimental accelerogram, shown in Figure 3.4 c.

As it was mentioned in section 3.4.1, one of the reasons for the lack of high amplitude cycling in the structural experimental response is the relatively short duration of the active part of the seismic excitation (effective strong motion duration of 9.2 s according to Trifunac-Brady [20]). Since the ultimate limit state of the structure was defined by the decrease of its strength, seismic excitations with duration longer than that of the experimental accelerogram would give more conservative estimate of the vulnerability of the structure. Also, the studies on the European strong motion records [35, 36] show that most of them have effective duration longer than 10 s. For these reasons the accelerograms were generated with longer duration than the experimental one and had mean duration of 27.4 s.

PGA was chosen as seismic intensity parameter, since the experimental tests were related to its value. It should be noticed that when estimating the fragility of non-linear systems under spectrum compatible seismic excitations, one of the generated accelerogram could be designated as the 'mean seismic excitation', *i.e.* the excitation which affects the responses the closest to the mean values of the seismic response parameters under all the considered seismic intensities [37, 38]. Under this assumption, the mean values of all the seismic intensity parameters which are linearly proportional to PGA (spectral velocity, spectral displacement, Kappos intensity [39], *etc.*) will be proportional to the mean PGA and the fragility curves derived on such intensity parameters will coincide on the so called 'normalized fragility plot', where the respective seismic intensity parameter is divided to its 'design' value, i.e., value corresponding to a preset PGA [37, 38]. In this way, when estimating fragility for spectrum compatible seismic excitations, the PGA well represents the seismic intensity.

The response of the experimental structure was calculated for five different levels of seismic intensity: PGA of 5% *g*, 32% *g*, 64% *g,* 80% *g* and 90% *g*. The models of the structure created to best fit the experimental behaviour for the respective intensities were used. For PGA of 90% *g* the model created for PGA of 80%*g* was used. The number of the generated accelerograms considered proved to be sufficient, since the standard deviations of the studied seismic response parameter stabilize over such number of simulations, as shown in Figure 3.26 for all the considered PGA.

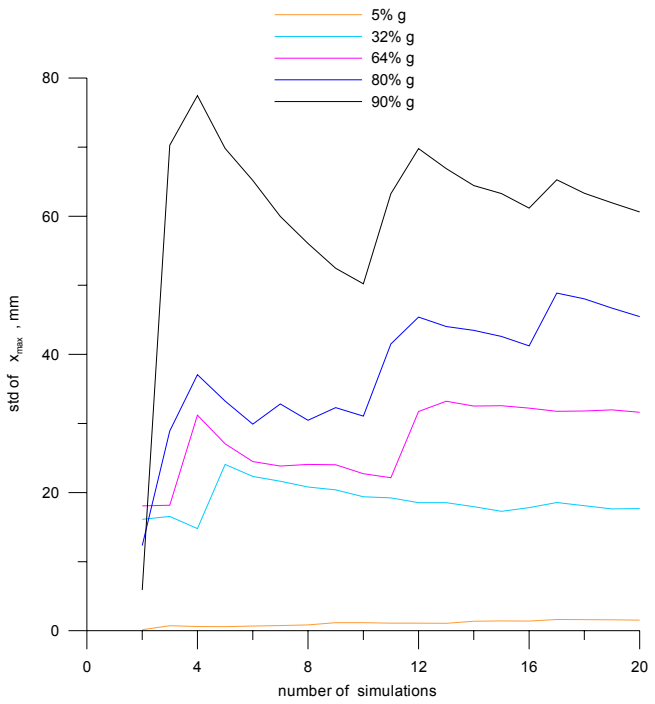

Figure3.26. Standard deviations of the seismic response parameter

The values of the seismic response parameter obtained by the numerical simulations are shown in Figure 3.27 a.

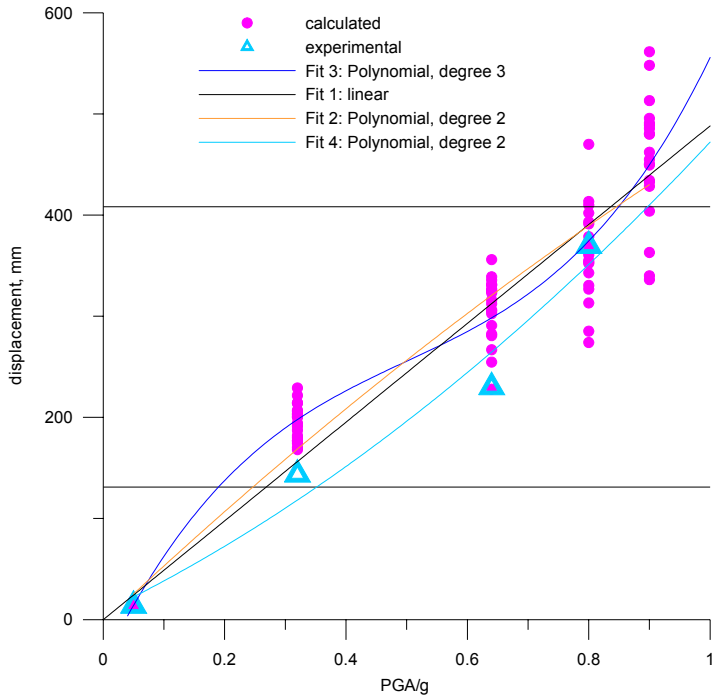

Figure 3.27 a. Maximum storey drifts at different PGAs

The functional relationship between the seismic response parameter and the seismic intensity is represented by three different fits (denoted by fit 1, fit 2 and fit 3) exhibiting high values of the coefficient of determination R_d^2, as shown in Table 3.8.

Table 3.8. Fits of the calculated responses

	Equation	R_d^2	Dimensions	
			argument	function
Fit 1	$x = 488.24y$	0.980	PGA/g	mm
Fit 2	$x = -92.940y^2 + 564.134y - 2.338$	0.928	PGA/g	mm
Fit 3	$x = 1226.404y^3 - 1829.505y^2 + 1195.272y - 38.5$	0.944	PGA/g	mm
Fit 4	$x = 174.904y^2 + 289.632y + 7.595$	0.966	PGA/g	mm
Fit 5	$F = 998.561y^3 - 1986.519y^2 + 1231.329y + 4.508$	0.998	PGA/g	kN
Fit 6	$OSDI = 2.012y^3 - 2.288y^2 + 1.306y - 0.026$	0.958	PGA/g	-
Fit 7	$DI_{hrc} = -0.477(ISD\%)^2 + 13.892ISD\% - 1.822$	0.997	-	-

All the three fits converge near the ultimate displacement at PGA of 0.83 *g*, As it can be seen in Figure 3.27 a. In the same figure and in Table 3.6 a fit of the experimental maximum displacements, denoted as fit 4 is presented. According to it, the structure reaches the ultimate displacement at PGA of 0.89 *g*. This value confirms the numerical result, according to which the structure would reach the ultimate displacement x_u = 0.408 m at PGA of 87% *g* (see section 3.4.4). At the same time this result shows the influence of the high amplitude cycling on the ultimate limit state, since under the generated accelerograms the structure reaches the ultimate displacement at a lower value of PGA (0.83 *g*).

Although the three fits of the simulated maximum displacement converge well at the ultimate displacement, they provide different representation of the structural response in the range of lower PGA. The estimation of the fit, which best represents the structural behaviour over a wider range of PGA is done on the basis of the estimation of the PGA at yielding. In Figure 3.27 b the maximum base-shear forces calculated for the generated accelerograms are presented.

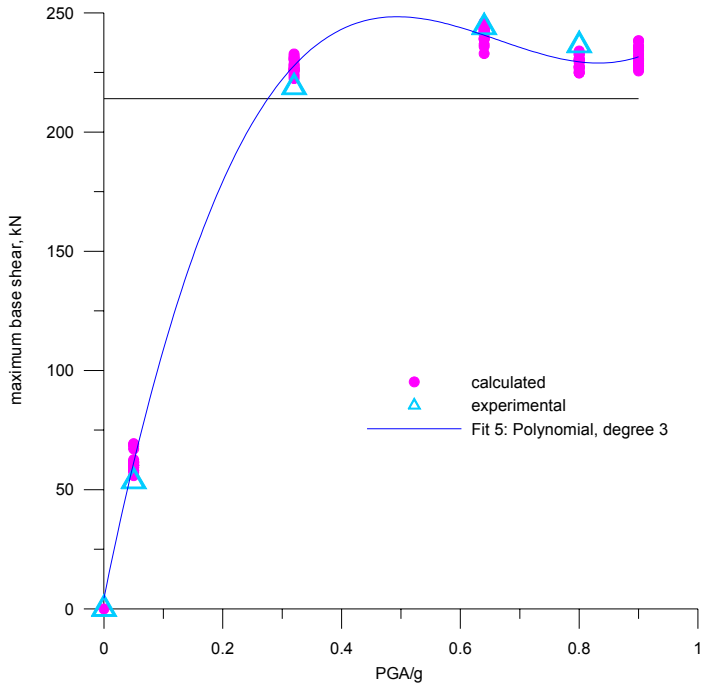

Figure 3.27 b. Maximum base-shear forces calculated from the generated accelerograms

The functional relationship between the maximum base-shear and PGA/*g* (denoted as fit 4), which exhibits $R_d^2 = 0.998$ is shown in Table 3.8. According to it, the maximum base-shear reaches $F_y = 214$ kN at PGA of 0.275 *g*. As it can be seen from Figure 3.27 a, the fit of the maximum storey displacement, which gives the most close result for the yield displacement is the linear fit ($x = 0.131$ m at PGA of 0.27 *g*). The non-linear fits provide lower PGA at yielding. In this way the linear functional relationship between the maximum storey displacement and the seismic intensity, represented by fit 1, is chosen as predictive equation for the fragility analysis.

In Table 3.9 the mean values, the standard deviations (st.d.), the coefficients of variation (c.o.v.), the median values and the lognormal standard deviations (l.st.d.) of the simulated maximum storey displacements for the considered different levels of PGA are shown.

Table 3.9. Statistical characteristics of the simulated seismic response parameter

PGA/*g*	mean, m	st.d., m	c.o.v.	median, m	l.st.d.
0.05	0.0149	0.00153	0.1028	0.015	0.1025
0.32	0.1954	0.01804	0.0923	0.195	0.0921
0.64	0.3069	0.03162	0.103	0.305	0.1028
0.8	0.3626	0.04546	0.1254	0.36	0.1249
0.9	0.455	0.06062	0.1332	0.451	0.1327

The coefficients of variation and the lognormal standard deviations exhibit almost equal values for all the considered seismic intensities. For this reason a constant lognormal

standard deviation equal to its mean value of 0.111 was considered in the fragility analysis. Since the models of the structure were obtained by fitting the experimental data, no uncertainty in the median value of the capacity R_m due to limitations in data and approximating in modeling is to be taken into account in the fragility estimation, *i.e.* β_{us} = 0. Similarly, since the characteristics of the materials were estimated experimentally, the randomness of the seismic capacity β_r is also zero. In this way, in the present experiment-based study only the randomness in the seismic response parameter affected by the randomness of the seismic excitation is considered, by setting β_s = 0.111. The resulted fragility curve is shown in Figure 3.28.

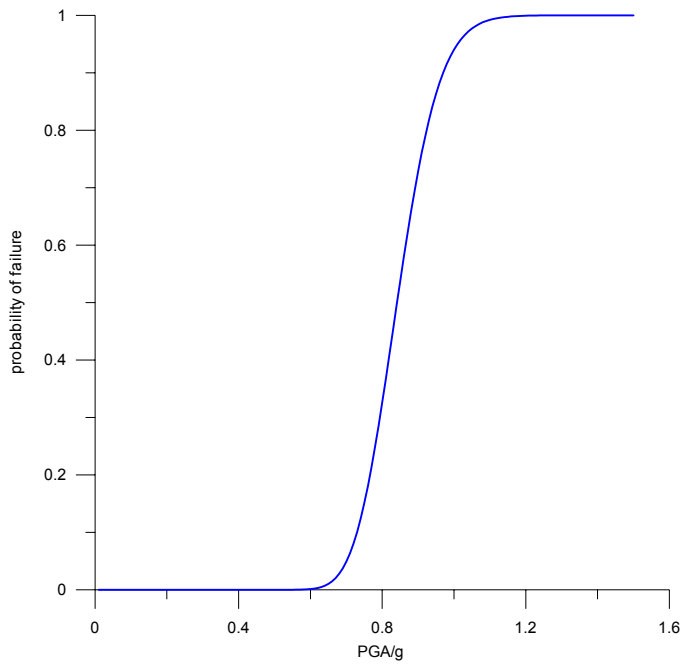

Figure 3.28. Fragility of the considered structure

As it can be seen from Figure 3.28, the experimental structure exhibits very reliable seismic behaviour, since the conditional probability of failure is less than 1% for PGA < 0.65 *g*. The frame will reach the ultimate limit state with provability of 95% at PGA of 1 *g*.

3.6 Qualification of the damage grade

The experimental test and the numerical models of the structure based on it give the possibility of adjusting some of the widely-used damage indices to the observed degree of damage. During the numerical simulations with IDARC 5.5, the overall structural damage index (OSDI) [13, 40, 42] was calculated for the experimental and generated accelerograms. According to the procedure implemented in such programme, the global damage is obtained as a weighted average of the local damage at the ends of each element, with the dissipated energy as a weight factor. The local damage index is described by the following relation:

$$DI_L = \frac{\theta_m - \theta_r}{\theta_u - \theta_r} + \frac{\beta}{M_y \theta_u} E_T \qquad (3.16)$$

where:

DI_L is the local damage index;
θ_m is the maximum rotation attained during the load history;
θ_u is the ultimate rotation capacity of the cross-section;
θ_r is the recoverable rotation at unloading;
β is a strength degrading parameter;
M_y is the yield moment of the cross-section;
E_T is the dissipated hysteretic energy.

The obtained values of OSDI for the generated accelerograms are shown in Figure 3.29 a. The functional relationship between OSDI and the seismic intensity is presented in Figure 3.29 a and described as fit 6 in Table 3.8.

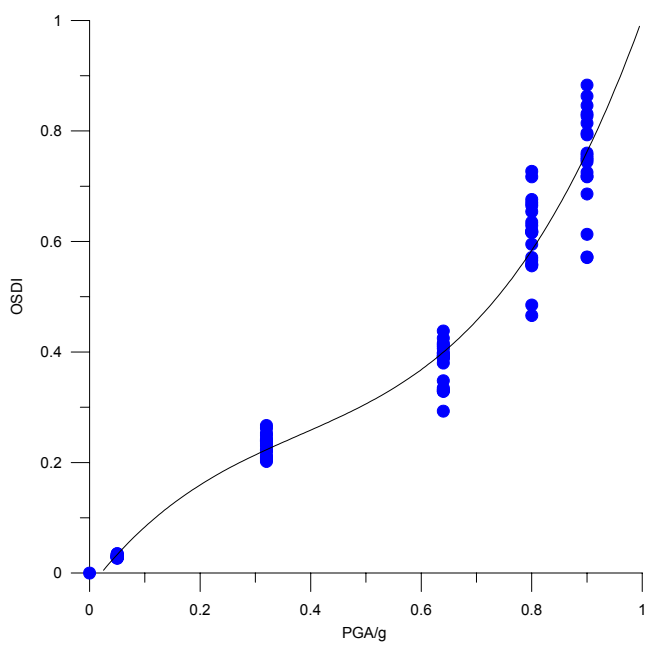

Figure 3.29 a. OSDI for the generated accelerograms

Another widely used overall damage index is the maximum interstorey drift (ISD%), expressed in per-cents of the storey height. As reported in section 3.5, ISD (in this particular case equal to the storey displacement) was used as a seismic response parameter for the fragility analysis. ISD is related to the PGA of the generated accelerograms as described in Table 3.8 (fit 1).

In connection with the derivation of vulnerability functions for European-type RC structures based on observational data, a new damage scale named the homogenized reinforced concrete damage scale (HRC scale) was proposed and used to generate vulnerability curves [41]. The scale is subdivided into seven damage states, each of which is defined in terms of the typical expected structural and non-structural damage, as shown in Appendix B for ductile moment resisting frames (MRF). The limit states are defined in terms of HRC-damage index (DI_{hrc}), which provides a numerical reference scale for experimental calibration. According to the damage observed during the experimental tests, the values of 0, 30, 50 and 70 are assigned to DI_{hrc} for the tests with PGA of 5% *g*, 32% *g*, 64% *g* and 80% *g*, respectively. In Figure 3.29 b these values of DI_{hrc} are related to ISD% measured during the respective tests. The functional relationship between DI_{hrc} and ISD% obtained by non-linear regression is described in Table 3.8 as fit 7. Further, it is used to convert the predictive equation for ISD over PGA to DI_{hrc} over PGA obtained from the generated accelerograms and in this way to relate the calculated damage indices with the index, based on observational data.

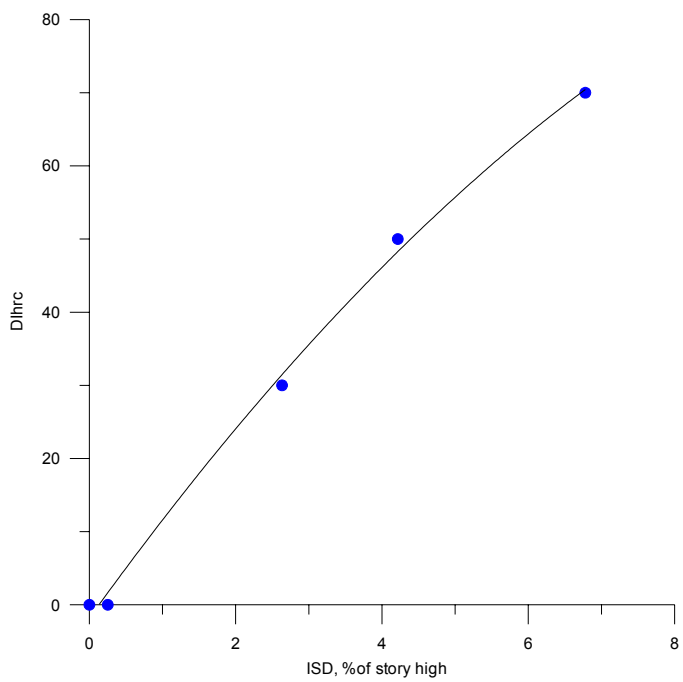

Figure 3.29 b. Relation between DI_{hrc} and ISD%

In the present study an attempt is made to associate the damage indices with the conditional probability of failure and to express the damage states of the studied structure in terms of its fragility. In Figure 3.30 the predictive equations for the considered damage indices over PGA are compared with the structural fragility. Aiming at a more

homogeneous representation of the damage indices, the ISD% is divided by 10 and DI_{hrc} is divided by 100.

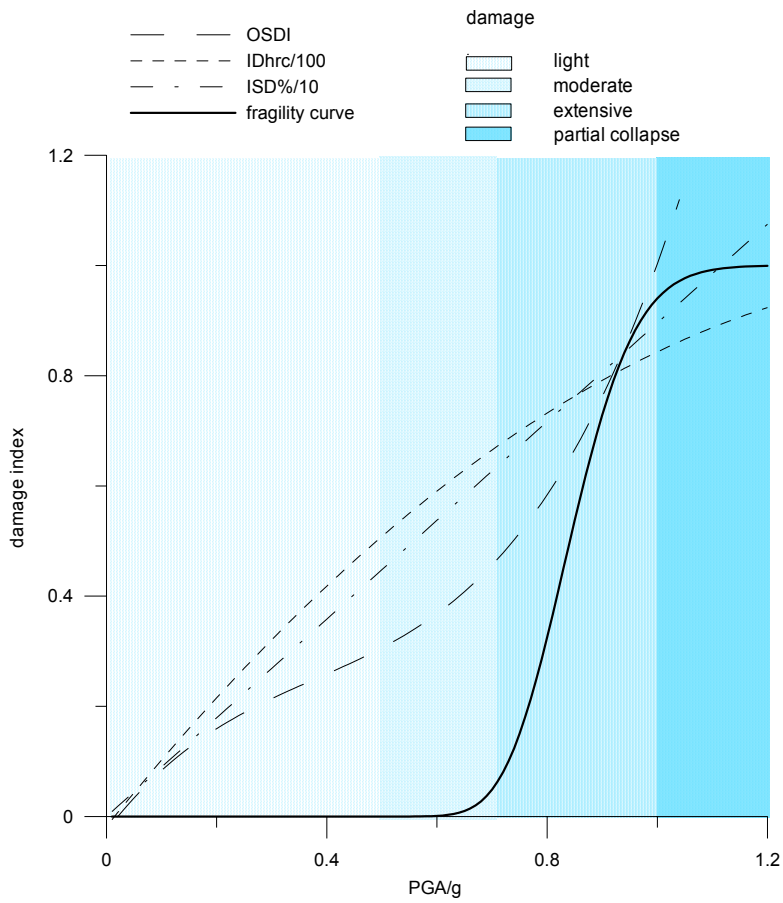

Figure 3.30. Qualification of structural damage grade

As it can be seen from Figure 3.30, conditional probability of failure of 0.1% corresponds to PGA = 0.6 *g*, OSDI = 0.37, ISD% = 5.4 and DI_{hrc} = 59. Such combination of small probability of failure and high values of the damage indices is caused by two main reasons:

(i) the experimental structure was designed and detailed according to Eurocode 8 provisions for ductility class H and the ductility enhancement measures allow high inelastic excursions to occur. In this way relatively higher values of the damage indices are related to relatively lower damage states,

(ii) the fragility curve has a relatively steep ambiguous part due to the fact that it is based on an experimental study and the randomness in the seismic response parameter is affected only by the randomness of the seismic excitation.

The relation of the rounded-off values of the studied damage indices with the probability of failure *Pf*, PGA and structural damage is presented in Table 3.10. The description of the damage grade is the same, as in [41](see Appendix B).

Table 3.10. Qualification of the structural damage

Pf	PGA/*g*	OSDI	ISD%	DI_{hrc}	Damage grade	EMS, vuln. class E	EMS intensity
$< 10^{-6}$	< 0.5	< 0.3	< 4.5	< 50	Light	Grade 1	≤ IX
10^{-6}- 10^{-1}	0.5 – 0.7	0.3 – 0.5	4.5 – 6.5	50 - 70	Moderate	Grade 2	X
0.1 –0.95	0.7 – 1.0	0.5 – 0.95	6.5 - 9	70 - 90	Extensive	Grade 3	XI
> 0.95	> 1.0	> 0.95	> 9	> 90	Partial collapse	Grade 4	> XI

For the considered structure the light and moderate damage grades are connected to practically no probability of failure. The extensive damage corresponds to the ambiguous part of the fragility curve and the partial collapse would take place at very high probability of failure (*Pf* > 0.95).

Based on experimental observations [42, 43, 44], it was assumed that OSDI < 0.3 corresponds to minor damage, for which usually no repair measures are needed. This conclusion coincides with the definition of the light damage in terms of OSDI and *Pf* given in Table 3.8. According to [42, 43, 44], the moderate damage in buildings for which repair need to be carried out is characterized by 0.3 <OSDI < 0.6, and the extensive damage, for which repair is not economically justified correspond to 0.6 <OSDI < 1. These values also agree well with the definitions of the moderate and extensive damage for the experimental structure. Consequently, there is very good coincidence between the OSDI defined damage grades and the homogenized reinforced concrete damage scale damage index DI_{hrc}.

According to the European Macroseismic Scale (EMS) [45], the studied industrial structure belongs to vulnerability class E as a frame structure with high level of earthquake resistant design. The structural damage grade is related to the EMS classification of the damage of buildings of RC, as presented in Table 3.8. On this basis, the expected EMS intensity is associated to the probability of failure and damage indices. The structure will suffer light damage from earthquakes with EMS intensity ≤ IX, corresponding to PGA/*g* < 0.5. The extensive damage would take place only during devastating earthquake with EMS intensity of XI.

4. STRUCTURE B

4.1. Experimental programme for Structure B

The experimental programme included pseudodynamic tests for the dynamic response of Structure B under seismic excitations with PGA of 5% *g*, 32% *g* and 64% *g*, as well as a repeated test with PGA of 64% *g*. The experimental accelerogram was the same as in case of Structure A. The acceleration response spectrum of the accelerogram is shown in Figure 2.3.

Similarly to the case of Structure A, the control measurement comprised the applied displacements and the related reaction forces. As shown schematically in Figure 4.1, relative displacements transducers were placed at six levels on the north and south faces at the bottom of two lateral columns (further referred to as column NE and NW) and the two central columns (further referred to as column NC and SC).

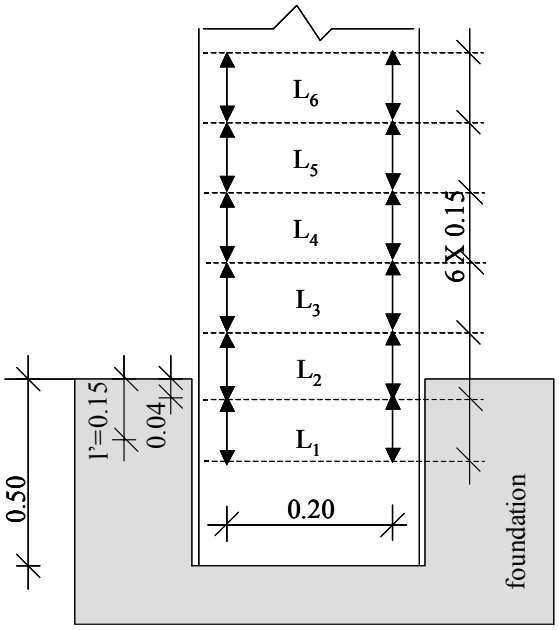

Figure 4.1. Instrumentation of the bottom part of columns NC, SC, NE and NW

In Figure 4.2 the plan of the experimental structure with denotation of the position of the columns is presented.

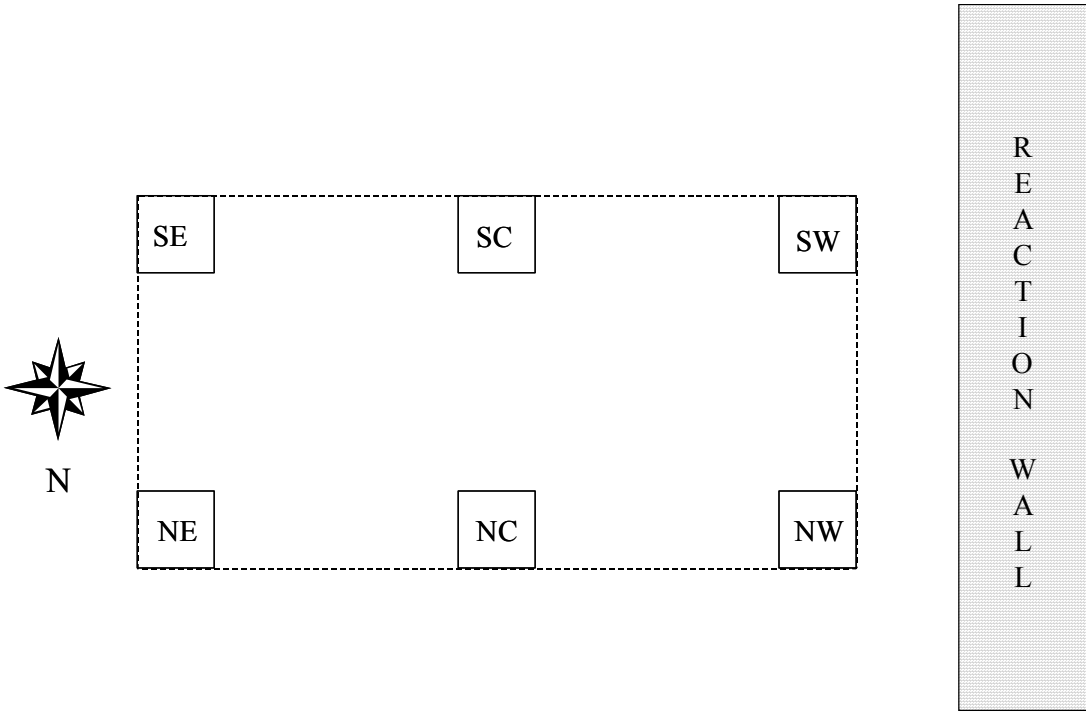

Figure 4.2. Plan of the experimental structure

The absolute rotations of the top part of columns NE, NC and NW were recorded by inclinometers placed at 0.2 m from the bottom of the beams, as shown in Figure 4.3.

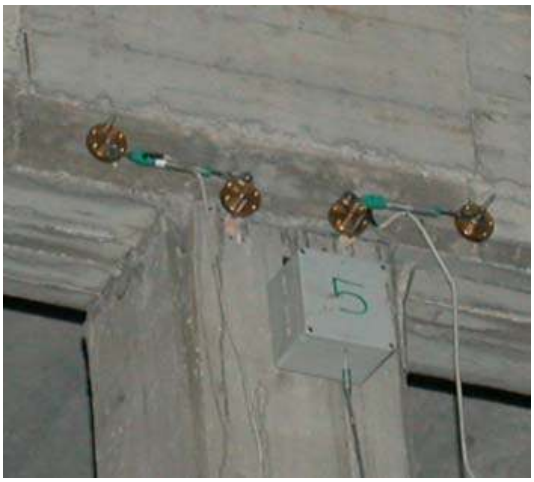

Figure 4.3. Disposition of the inclinometers

4.2 Deficiencies observed in the construction of Structure B

As it was mentioned, no special survey measures were taken during the construction, other than acceptance procedures for the materials and check of the quantities of rebars (and not of their positioning), relying on what could have been intended as 'standard construction practice'. As a result, a number of inaccuracies and mistakes in the practical arrangement of the rebars took place, the effect of which is the main subject of this report. The following inaccuracies in the execution of the structure were observed after removing the concrete cover at the end of the test programme:

(i) inaccurate spacing of the stirrups. In the critical regions of the structure the design project envisaged spacing of the stirrups at 50 mm spacing, as shown in Figure 2.2. The actual spacing measured after the testing was 90-150 mm, as shown in Figure 4.4 a for the bottom of column NE. It is worth mentioning that this was solely due to the movements of the stirrups during the compaction of the concrete, since it was reported that all stirrups were in their exact position before casting.

Figure 4.4 a. Spacing of stirrups at the bottom of column NE

(ii) wrong anchoring of longitudinal reinforcement of the columns into the beams, which, together with the insufficient thickness of the concrete cover, caused the premature separation of the longitudinal reinforcement from the concrete during the tests. In Figure 4.4 b the disposition of the straight lead embedment in the beam-column joint of column NE is shown. The design envisaged their

positioning within the rebars of the beam (Figure 2.2), and the mistake originated either from a wrong interpretation of the construction drawings, or from the sought ease in assembling the pre-arranged rebars of columns and beams.

Figure 4.4 b. Anchoring of longitudinal reinforcement in the beam-column joint of column NE.

(iii) inaccurate placing or lack of stirrups in the beam-column joints. In the beam-column joint of column SE shown in Figure 4.4 c the stirrups are missing. Positioning of the stirrups inside the joint was omitted by the construction workmanship, since the stirrups would have made it impossible to connect the pre-assembled rebars of columns and beams.

Figure 4.4 c. Lack of stirrups in the beam-column joint (column SE)

These inaccuracies were considered in the numerical modelling of the seismic behaviour of Structure B as follows:

(i) the increased strength of concrete due to confinement was not taken into account when estimating the moment-curvature relationships of the structural members (section 4.3.1). For comparison, in case of correct spacing of stirrups at 50 mm the strength of concrete would have increased by 25 %, as demonstrated in the modelling of Structure A.

(ii) the beam-column joints were considered as semi-rigid. Based on the experimental data for the absolute rotations of the top parts of the columns, the curvatures corresponding to the cracking and yielding moments were determined, as described in section 4.3.2.

(iii) the inelastic buckling of the longitudinal reinforcement was considered as a possible failure criterion.

4.3. Modelling of the seismic response of Structure B

4.3.1 Background assumptions

The properties of the concrete and steel of Structure B are shown in Appendix A. The cross-section capacities were calculated by taking into account the hardening of the steel and the properties of the unconfined concrete. The moment – curvature relationships of the columns were estimated with reference to the values of axial forces N, obtained during the seismic design - N = 221 kN for the central columns and N = 100 kN for the lateral columns [3]. The yielding moments M_y were calculated assuming that the reinforcement bars located at the middle of the cross-section were still not yielded in tension. Having in mind the observed inaccuracies in the construction, the depth of the concrete cover *d'* in column NC was taken as *d'*= 20 mm. For the other columns the design thickness of the concrete cover *d'*= 30 mm was considered.

In Table 4.1 the moment-curvature characteristics of the bottom cross-sections of the columns and of the beams, obtained by a fibre model [14] based on the cross-section parameters and material properties, are shown. The yielding curvatures φ_y do not account for the fixed-end rotations, due to the bar pull-out and the shear distortion of the shear span at flexural yielding. Similarly to the case of Structure A, the yielding curvatures φ_{yp}, which account for the above phenomena were obtained based on Eq. (3.2) (see section 3.2.1).

The yielding curvatures φ_y, shown in Table 4.1 are obtained by a fibre model [14] based on the cross-section parameters and material properties and did not account for the fixed-end rotations due to the bar pull-out and for the shear distortion of the shear span at flexural yielding. Yielding curvatures φ_{yp}, which account for the above phenomena were obtained based on the relationship for the yielding chord rotation given in [15, 16] as described in details in section 3.2.1.

The resulting moment–curvature relationships are shown in Table 4.1, where the following tations are used:

M_{cr} and φ_{cr} are the moment and curvature at cracking,
M_y and φ_y are the moment and curvature at yielding,
M_u and φ_u are the ultimate moment and curvature,
M_{des} is the design value of the resistant bending moment,
φ_{yp} is the curvature at yielding taking into consideration the pull-out of the reinforcing bars and shear effects, as considered below in the current section.

Table 4.1. Cross-section characteristics

		M_{cr}, kNm	φ_{cr}, rad/m	M_y, kNm	φ_y, rad/m	φ_{yp}, rad/m	M_u, kNm	φ_u, rad/m	M_{des}, kNm	M_y/M_{des}
	Beams	94.	$7.95\ 10^{-4}$	179.	$7.4\ 10^{-3}$	$22.\ 10^{-3}$	219.	$73.\ 10^{-3}$	154.4	1.16
Bottom	Col. NE, NW, SE, SW	25.	$1.33\ 10^{-3}$	82.	$12.7\ 10^{-3}$	$19.7\ 10^{-3}$	73.	$151.\ 10^{-3}$	78.6	1.04
	Col. NC	32.	$1.67\ 10^{-3}$	97.	$12.6\ 10^{-3}$	$19.2\ 10^{-3}$	90.1	$103.\ 10^{-3}$	92.6	1.05
	Col. SC	32.	$1.67\ 10^{-3}$	96.	$13.9\ 10^{-3}$	$20.8\ 10^{-3}$	85.	$103.\ 10^{-3}$	92.6	1.04
Top	Col. NE	25.	$1.71\ 10^{-3}$	82.	$22.9\ 10^{-3}$	-	73.	$151.\ 10^{-3}$	78.6	1.04
	Col. NW, SE, SW	25.	$3.78\ 10^{-3}$	82.	$31.1\ 10^{-3}$	-	73.	$151.\ 10^{-3}$	78.6	1.04
	Col. NC	32.	$2.35\ 10^{-3}$	97.	$23.2\ 10^{-3}$	-	90.1	$103.\ 10^{-3}$	92.6	1.05
	Col. SC	32.	$2.35\ 10^{-3}$	96.	$23.2\ 10^{-3}$	-	90.1	$103.\ 10^{-3}$	92.6	1.05

The comparison of the strengths of the bottom cross-section of Structure B with those for Structure 1 shows a decrease of about 10% as a consequence of the reduced strength of the concrete due to the insufficient confinement.

The properties of the top cross-sections of the columns were determined by taking into account the semi-rigidity of the beam-column joints caused by the improper anchoring of the columns longitudinal reinforcement in the beams and by the lack of stirrups, as described in section 4.3.2.

The seismic behaviour of the structure was modelled by means of the computer code IDARC 5.5 [13], taking into account the P-delta effects. The effective length of the columns l_e = 5.45 m was assumed, as determined in section 4.3.3. The initial stiffness *EI* of the members was determined by the ratio of the cracking moment and the curvature at cracking [13]. The hysteretic behaviour of the elements was modelled by using the smooth hysteretic model, which offers better possibilities to model the elastic-yield transition, the shape of unloading and the slip in comparison with the tri-linear hysteretic model. Separate hysteresis models for the columns were defined for each test in order to describe as better as possible the seismic behaviour of the structure. To take into account the effects of the previous excitations, acceleration spikes with the maximum amplitude of the previous excitation were imposed so to reach during them the maximum and minimum displacements experienced during the previous excitation, as illustrated in section 3.2.1.

As proved in section 3.2.2, the genealogy of the hysteresis parameters is a prerequisite for the correctness of the numerical models, when using different models for description the seismic response of a structure to excitations of different intensities. The parameters

describing the strength deterioration and the stiffness degradation used in the numerical simulations of the seismic response of the columns of Structure B are shown in Table 4.2. The notations are given in section 3.2.2.

Table 4.2. Characteristics of the hysteresis models of Structure B

PGA	HC	HBD	HBE	NTRANS	ETA	HSR	HSS	HSM
5% *g*	20	0.1	0.01	3	0.5	0.3	0.3	0.46
32% *g*	2.	0.3	0.01	3.5	0.2	0.3	0.9	0.16
64% *g*	1.5	0.3	0.2	8	0.8	0.16	0.15	0.16

The gradually-changing hysteresis parameters supplied correct simulations of the dynamic behaviour of the system under the experimental spectrum-compatible simulated accelerograms with longer effective duration used in the fragility analysis of Structure B (section 4.6). As shown in Table 4.3, there is no incompatibility of the results in the context of the case considered in section 3.2.2, since the maximum displacements calculated for the all of the generated accelerograms for PGA of 64% *g* are larger than the respective values for PGA of 32% *g*.

Table 4.3. Maximum simulated storey displacements (in mm) for PGA of 32% *g* and 64%*g*

Generated accelerogram №	PGA of 32% *g*	PGA of 64% *g*	Difference, mm
1	125.81	295.01	169.2
2	154.18	364.51	210.33
3	153.41	277.16	123.75
4	154.91	339.39	184.48
5	175.38	377.67	202.29
6	179.49	328.06	148.57
7	168.18	403.52	235.34
8	160.3	355.86	195.56
9	176.4	418.93	242.53
10	157.91	319.61	161.7
11	111.99	248.22	136.23
12	165.45	273.54	108.09
13	158.14	405.54	247.4
14	125.99	351.8	225.81
15	177.54	330.05	152.51
16	147.17	251.2	104.03
17	142.84	409.52	266.68
18	123.63	341.21	217.58
19	175.46	396.14	220.68
20	132.11	248.93	116.82

4.3.2. Semi-rigidity of the beam-column joints

The semi-rigidity of the beam-column joints was taken into account in the numerical model by considering the presence of moment-rotation springs between the top of the columns and the beam ends. These rotational springs act in series with the columns, thus:

$$M_{rs} = M_{tc} = M \qquad (4.3.1)$$

$$\rho_{tot} = \rho_{tc} + \rho_{rs} \qquad (4.3.2)$$

where:

M is the moment at the top cross-section of the column, ,

M_{rs} and ρ_{rs} are the moment and rotation of the rotational spring, *i.e.* of the beam-column joint,

M_{tc} and ρ_{tc} are the moment and rotation of the top of the column due to deformation of column, respectively,

ρ_{tot} is the absolute (total) rotation of the top of the column.

Since in the used computer code the plastic hinges at the ends of the columns are defined by introducing the moment-curvature relationship, Eq. (4.3.2) could be presented in the form:

$$\varphi_{tot} = \varphi_{tc} + \varphi_{rs} \qquad (4.3.3)$$

where:

$\varphi_{tc} = \rho_{tc} / L_p$ is the curvature in the plastic hinge zone due to deformation of the column,

$\varphi_{rs} = \rho_{rs} / L_p$ is the curvature in the plastic hinge zone due to semi-rigidity of the beam-column joint,

φ_{tot} is the absolute curvature in the plastic hinge zone at the top of the column,

L_p is the plastic hinge length, equal to the depth of the member [17].

The above consideration gave the possibility of defining the moment-curvature relationships at the top of the columns by using the moments at cracking and at yielding shown in Table 4.1. The corresponding curvatures φ_{cr} and φ_y were defined by using the records of the absolute rotations at the top of columns NE, NC and NW. It is accepted that the deformation of the beam-column joint does not influence the post-yield stiffness, the ultimate moments and the curvatures.

The absolute rotations at cracking $\rho_{tot,cr}$ were estimated from the records of the test with PGA of 5% *g*. The lateral force F_{cr}, which causes cracking in the frame could be approximately computed as [3]:

$$F_{cr} = \sum 2M_{cri} / l_e \qquad (4.3.4)$$

where

M_{cri} is the cracking moment of the *i-th* column,
l_e is the effective length of the column.

By using the cracking moments corresponding to the actual material properties (shown in Table 4.1) and l_e = 5.45 m, F_{cr} was estimated as 60.18 kN. During the test with PGA of 5%, the base shear of Structure B reached F_{cr} at t = 7.48 s. In Table 4.4 the corresponding values of $\rho_{tot,cr}$ and the absolute curvatures in the plastic hinge zone at cracking $\varphi_{tot,cr}$ calculated as $\varphi_{tot,cr} = \rho_{tot,cr} / L_p$ are shown.

Table 4.4. Rotations and curvatures at the top of the instrumented columns

column	$\rho_{tot,cr}$, rad	$\varphi_{tot,cr}$, rad/m	$\rho_{tot,y}$, rad	time, s	$\varphi_{tot,y}$, rad/m
NE	0.513 10^{-3}	1.71 10^{-3}	6.88 10^{-3}	7.54	22.9 10^{-3}
NC	0.705 10^{-3}	2.35 10^{-3}	6.97 10^{-3}	8.31	23.2 10^{-3}
NW	1.135 10^{-3}	3.78 10^{-3}	9.32 10^{-3}	7.56	31.1 10^{-3}

Similarly to F_{cr}, the approximate lateral force at yielding F_y = 191.6 kN was calculated by substituting the yielding moments corresponding to the actual material properties shown in Table 4.1 in Eq. (4.3.4.). The base-shear of Structure B reached F_y during the test with PGA of 32% *g* at t = 7.56 s. The absolute rotations at yielding $\rho_{tot,y}$ at the top of columns NE, NC and NW were estimated from the records of the absolute rotations. It was assumed that the moments at the top of the columns were proportional to the horizontal displacement of the floor slab up to the first yielding. This consideration gave the possibility of determining the absolute rotations at yielding $\rho_{tot,y}$ as corresponding to the substantial change of the slope of the displacement-rotation diagram. In Figures 4.5 a,b,c the experimental relationships floor slab displacement – rotation at the top of the column, are shown for columns NE, NC and NW, respectively. The considered points of substantial change of the slope are marked in the Figures 4.5 a,b,c. The respective values of the absolute rotations at yielding $\rho_{tot,y}$ and absolute curvatures in the plastic hinge zone at yielding $\varphi_{tot,y}$ calculated as $\varphi_{tot,y} = \rho_{tot,y} / L_p$ are shown in Table 4.4, as well as the moment of their appearance during the test with PGA of 32% *g*.

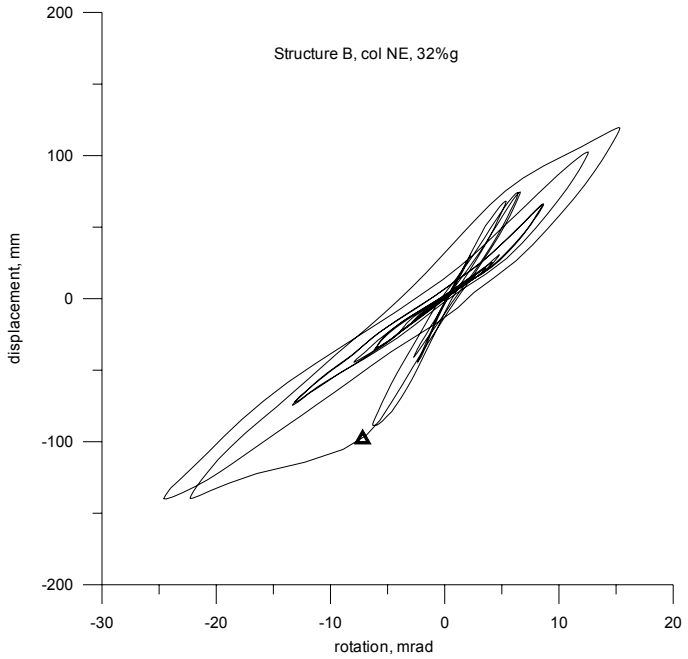

Figure 4.5 a. Storey displacement – top rotation relationship for column NE

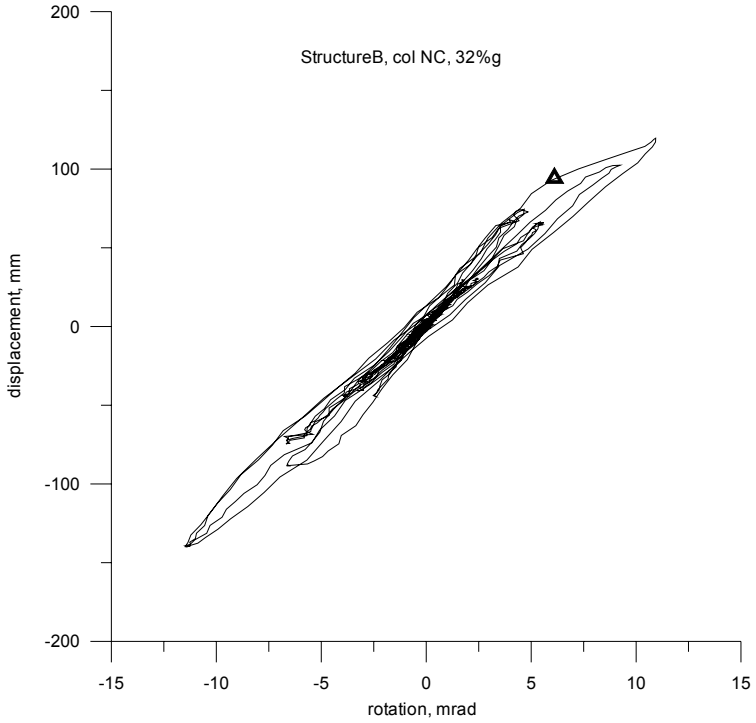

Figure 4.5 a. Storey displacement – top rotation relationship for column NC

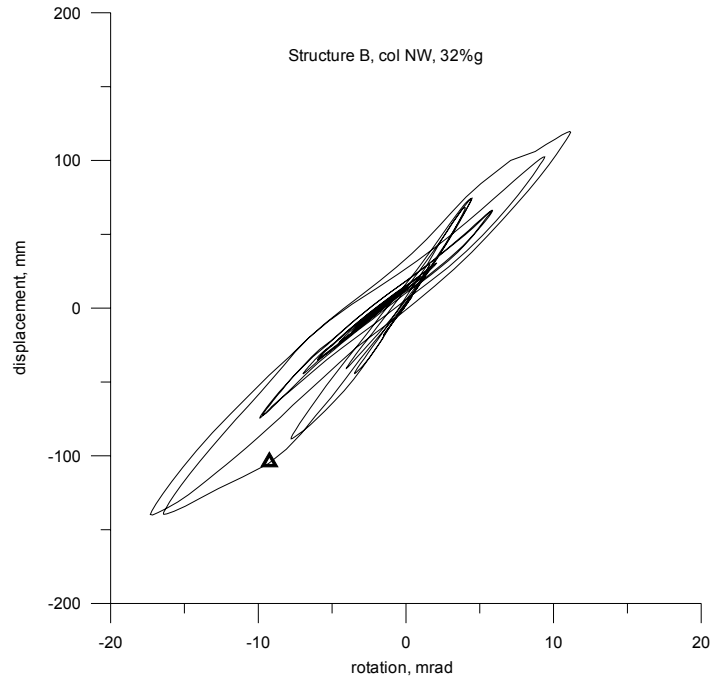

Figure 4.5 a. Storey displacement – top rotation relationship for column NW

As it can be seen from Table 4.4, the obtained values of $\varphi_{tot,cr}$ and $\varphi_{tot,y}$ are larger than the corresponding values for the bottom of the columns shown in Table 4.1. They prove that the improper reinforcing of the beam-column joints contributes considerably their deformability. As a consequence, the curvature of the top cross-sections at yielding increases up to 2.5 times, as in the case of column NW. As it can be seen in Figure 4.5 a, the post-yielding branch of the storey displacement – top rotation relationship for column NE exhibits the smallest stiffness in comparison with the post-yielding branches of the other joints. This substantial decrease of the post-yielding stiffness is most probably caused by the onset of separation of the longitudinal reinforcement from the concrete. As a consequence, the wrong anchoring of the longitudinal bars and the insufficient cover of the reinforcement (see Figure 4.4 b) substantially decreased the post-yield stiffness of the top cross-sections of the columns.

Having in mind the results of the observation of the status of the reinforcement after the tests, the values of $\varphi_{tot,cr}$ and $\varphi_{tot,y}$ obtained for column NW were also assigned to the lateral columns SE and SW, non-instrumented by inclinometers. The values of $\varphi_{tot,cr}$ and $\varphi_{tot,y}$ obtained for the column NC were assigned to the other central column SC, as shown in Table 4.1.

4.3.3 Determination of the effective length of the columns

For the determination of the curvatures in the critical zones at the bottom of the columns, Structure B was instrumented by relative displacements transducers placed at six levels

on the north and south faces at the bottom of columns NE, NC, NW and SC. As shown in Figure 4.1, the relative displacements were also measured below the top level of the foundation blocks within the e foundation 'pockets'. In Figures 4.6 a,b the mean curvatures obtained at Level 1 and Level 2 (see Figure 4.1) of column NW during the tests with PGA of 32% *g* and 64% *g*, respectively, are shown.

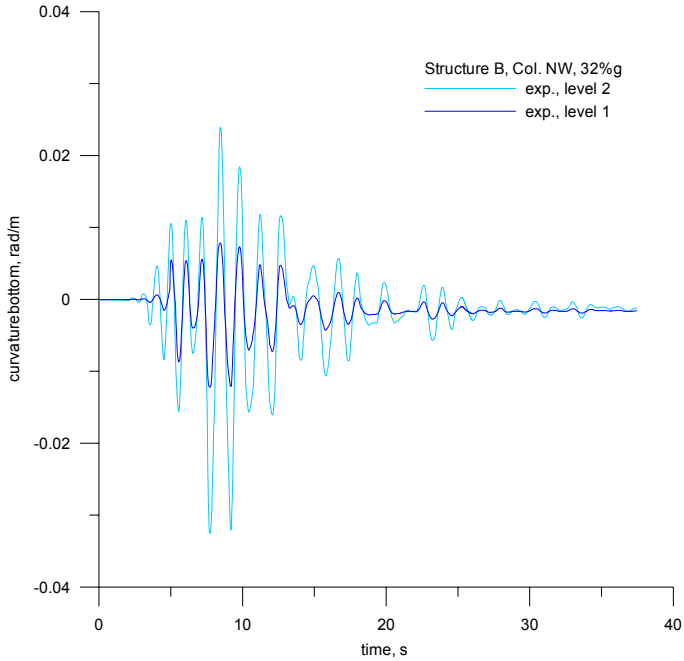

Figure 4.6 a. Curvatures at the bottom part of column NW during the test with PGA of 32% *g*

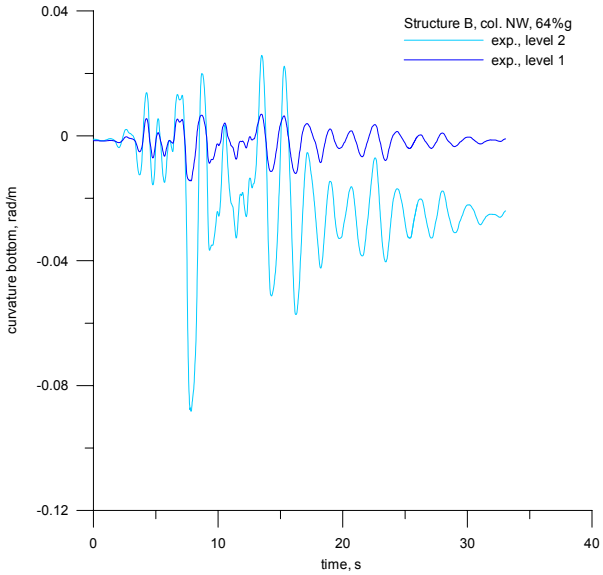

Figure 4.6 b. Curvatures at the bottom part of column NW during the test with PGA of 64% *g*

As it can be seen from these figures, the obtained curvatures of the zones of the columns embedded into the foundation are not negligible and give reason and possibility to estimate the length *l'* of part of the columns embedded into the foundation which reacts during the dynamic excitations. This part, together with the design length of the column *l* was considered to form the effective length of the column l_e:

$$l_e = l + l' \qquad (4.3.5)$$

The length *l'* was estimated by use of the experimental data for Level 1 corresponding to the fully embedded part of the columns and Level 2 corresponding to the partially embedded part of the columns. Based on these two estimates, the curvature - length *l'* relationship could be represented by a first order polynomial. In this way a liner relationship was assumed for the second derivative of such function, which describes the deformed shape of the embedded part of the column. The length *l'* was estimated as the interception of the obtained line with the longitudinal axis of the column. The data from the test with PGA of 32% g were used to obtain the length *l'* for each time point, and the mean values were calculated for the time interval during which the structure exhibited linear behaviour as well as for the whole duration of the test, as presented in Table 4.5.

Table 4.5. Estimated length *l'* of the part of the columns embedded into the foundation

	l' from the linear behaviour		*l'* from the whole duration	
	Mean value, m	Standard deviation, m	Mean value, m	Standard deviation, m
Col. NE	0.157	0.048	0.108	0.094
Col. NC	0.121	0.098	0.138	0.095
Col. NW	0.178	0.062	0.209	0.098
Col. SC	0.132	0.052	0.141	0.085
Mean *l'*	0.147		0.149	

As it can be seen from Table 4.5, the estimated mean lengths of the embedded part of the columns from the time-interval with linear response and from the whole duration of the test are almost equal. In the numerical model was accepted *l'* = 0.15m, thus l_e = 5.3 +0.15 = 5.45 m.

In Figure 4.7 the displacement time histories of Structure B during the test with PGA of 5% *g,* obtained with- and without consideration of the effective length of the columns l_e, are compared.

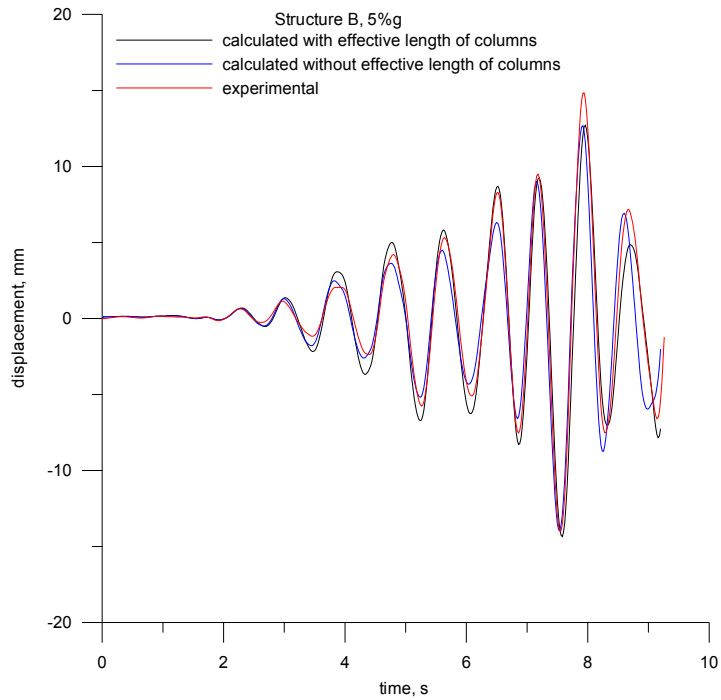

Figure 4.7. Influence of the effective length on calculated displacement time histories

The structural response calculated with consideration of l_e matches better the experimental displacement time history. Also, the natural period of Structure B estimated with consideration of l_e is 0.73 s and coincides fully with experimental one, whereas the natural period calculated without taking into account l_e is 0.70 s.

4.4. Experimental tests and their numerical simulations

4.4.1 Experimental test with PGA of 5% g

The recorded restoring force – displacement relationship shows considerable effects of cracking of the concrete, as shown in Figure 4.8 a. The maximum storey displacement was 0.27% of the storey height.

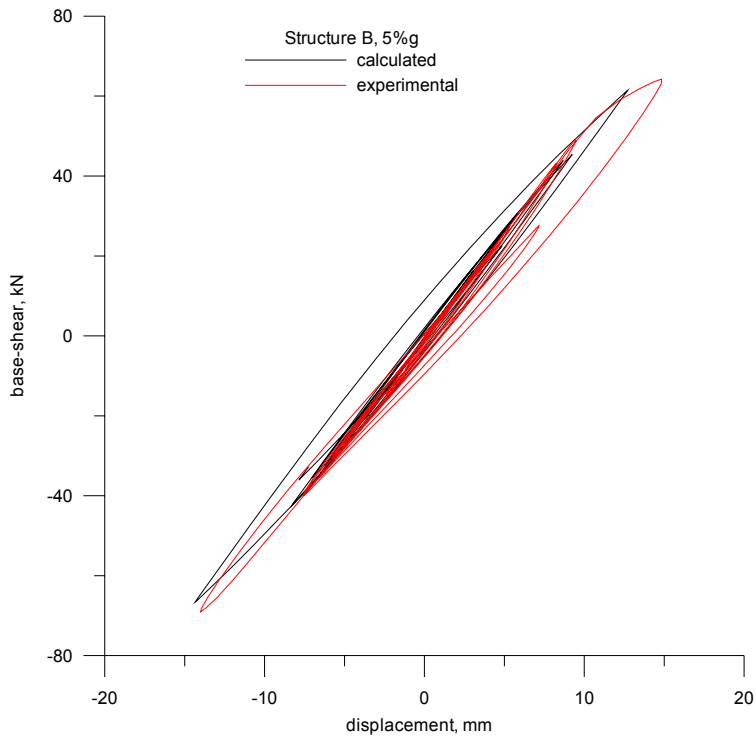

Figure 4.8 a. Hysteresis loop of Structure B for PGA of 5% *g*

The fundamental period of the structure was estimated as T_{1B} = 0.73 s using the part of the experimental relationship base-shear - storey displacement which corresponds to the non-degraded stiffness ($t \leq 4.80$ s). The natural period of 0.73 s, calculated by considering the effective length of the columns and the semi-rigidity of the bean-column joints coincides very well with T_{1B}. The calculated displacement time history shown in Figure 4.8 b as well as the calculated hysteresis loop of Structure B presented in Figure 4.8 a exhibit very good coincidence with the experimentally recorded ones.

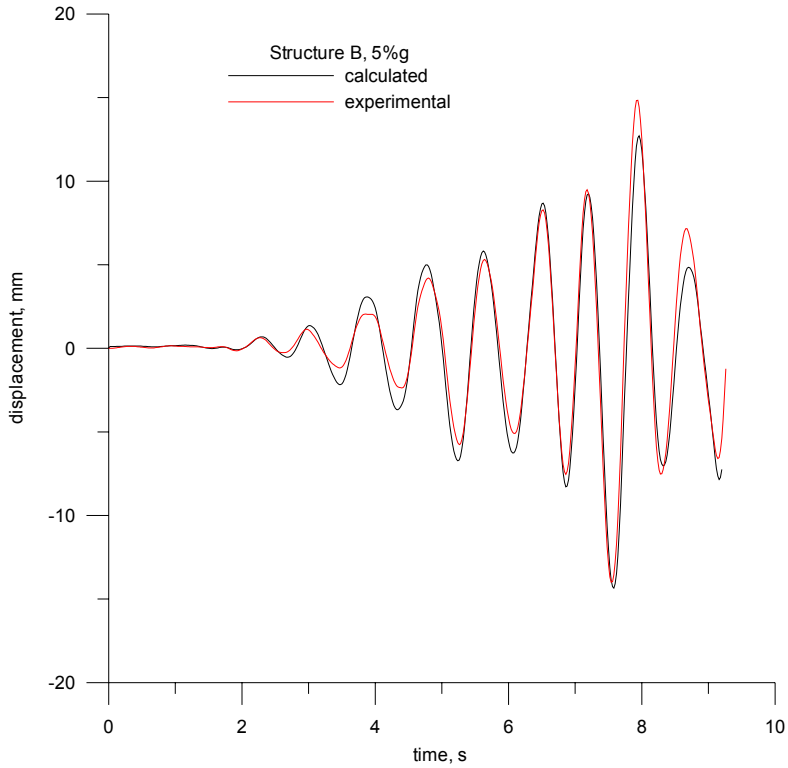

Figure 4.8 b. Displacement time history of Structure B for PGA of 5% *g*

The comparison of T_{1B} with the estimated fundamental period of Structure A (T_{1A} = 0.69 s) shows that the defects in the execution did affect the dynamic response of the structure even at the stage of elastic response, since the not well executed reinforcement of the beam-column joints caused additional rotations in them.

4.4.2. Experimental test with PGA of 32% g

The maximum storey displacement was 2.6% of the storey height. It was almost the same as in the case of Structure A, but, as shown in Figure 4.9, it corresponded to a large plastic excursion. Large flexural cracks appeared in the plastic hinge regions of the columns. No visible cracks appeared in the beams.

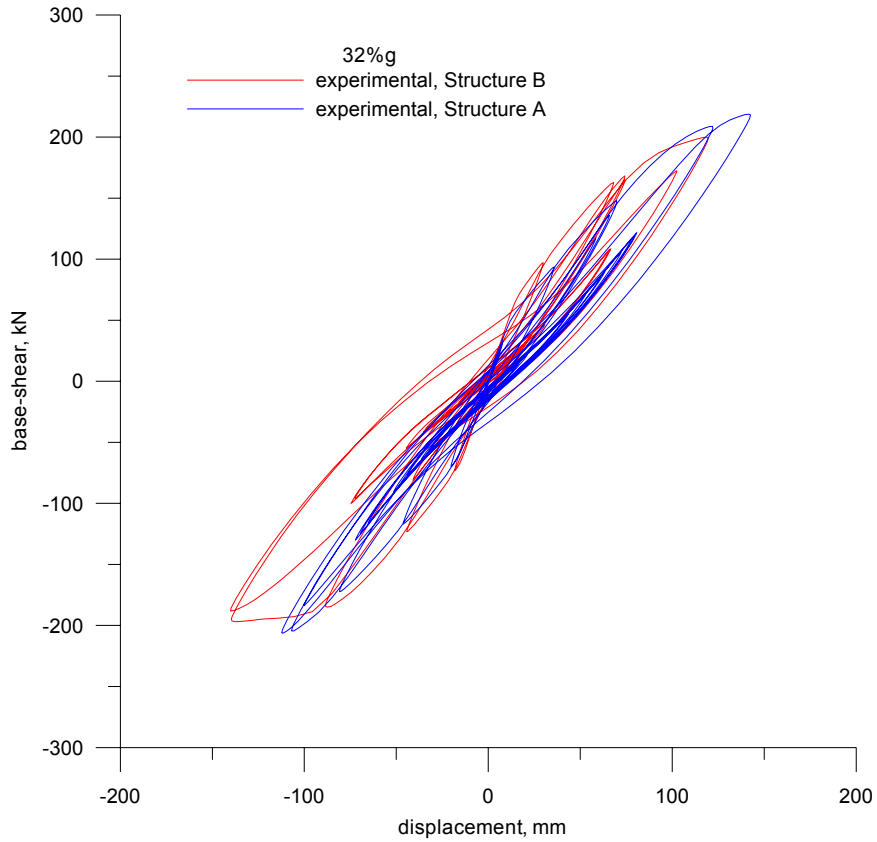

Figure 4.9. Experimental base-shear – storey displacement relationships at PGA of 32% *g*

At PGA of 32% *g,* Structure A reached the first yielding at the bottom of the lateral columns and, As it can be seen from Figure 4.9, neither substantial stiffness degradation, nor strength deterioration could be observed. As proven in section 4.3.2 from the records of the absolute rotations at the top of the columns, yielding appeared in all the columns of Structure B. The status of the bottom cross-sections of the columns of Structure B was estimated from the records of the relative displacements. The mean strains in the longitudinal reinforcement at Level 2 and Level 3 were obtained from the records of the relative displacements corrected for the depth of the concrete cover. The tension strain in the longitudinal bars ε_{1y} corresponding to the first yield was calculated by using Eq. (3.8) as 0.0075 for column NC, the concrete cover of which had a reduced depth of 0.02m, and 0.00733 for all the other columns. These yield strains were compared with the strains measured during the test at all the four sides of columns NE, NC, NW and SC. The results reported in Table 4.6 show the point when the first yielding (if any) appears.

Table 4.6. Appearance of the first yielding at the bottom cross-sections of the instrumented columns

column	level	side	$t_{\varepsilon=\varepsilon_{1y}}$, s	column	level	side	$t_{\varepsilon=\varepsilon_{1y}}$, s
NE	2	NW	-	NC	2	NW	7.58
		SW	-			SW	7.57
		NE	8.40			NE	8.33
		SE	8.35			SE	8.36
	3	NW	-		3	NW	7.55
		SW	-			SW	7.55
		NE	-			NE	8.31
		SE	-			SE	8.29
NW	2	NW	7.62	SC	2	NW	-
		SW	7.62			SW	-
		NE	-			NE	-
		SE	-			SE	8.37
	3	NW	7.68		3	NW	7.57
		SW	-			SW	7.57
		NE	-			NE	8.37
		SE	-			SE	8.42

As it can be seen from Table 4.6, yielding appeared at the bottom cross-sections of all the instrumented columns, being spread along the whole plastic hinge length of column NC, whereas in the other central column it was observed mainly at Level 3. This fact could be explained by the different position of the stirrups along the bottom part of the columns. The different degree of 'hinging' of the beam-column joints of the lateral columns caused their non-equal deformation and respectively – the different time moments, places and extent of yielding, as shown in Table 4.4.

The numerical model of the seismic response of Structure B exhibits good coincidence with the experimental global response characteristics, As it can be seen in Figures 4.10 a, b for the displacement time history and the base shear-story displacement relationship, respectively.

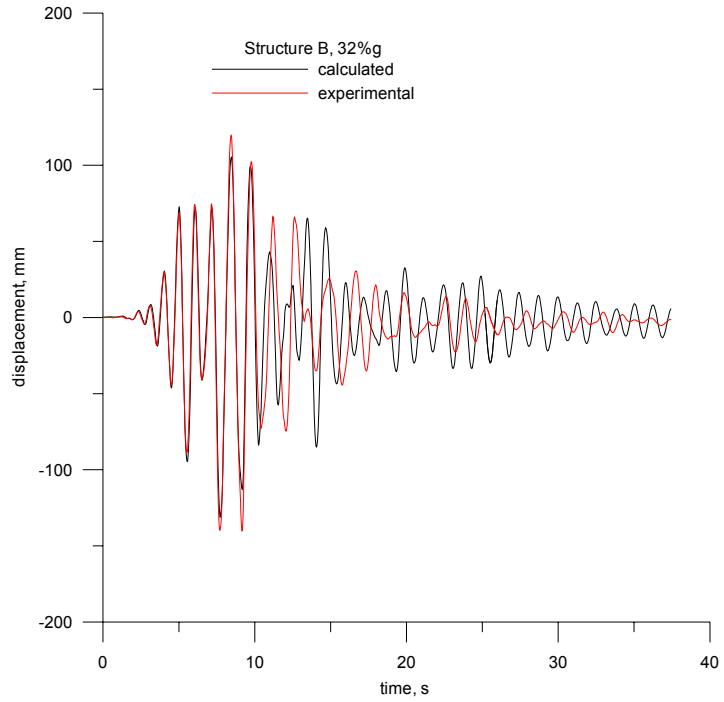

Figure 4.10 a. Displacement time history of Structure B for PGA of 32% *g*

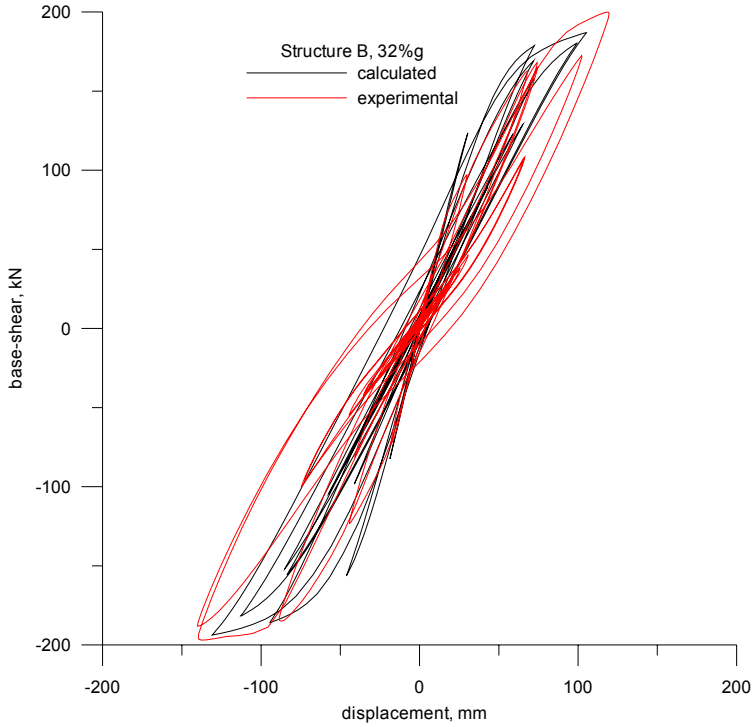

Figure 4.10 b. Hysteresis loops of Structure B for PGA of 32% *g*

In Figures 4.11.a, b, c, d the calculated curvatures at the bottom of the columns are compared to the experimentally obtained mean curvatures Level 2, Level 3 and Level 4 for columns NE, NC, NW and SC, respectively.

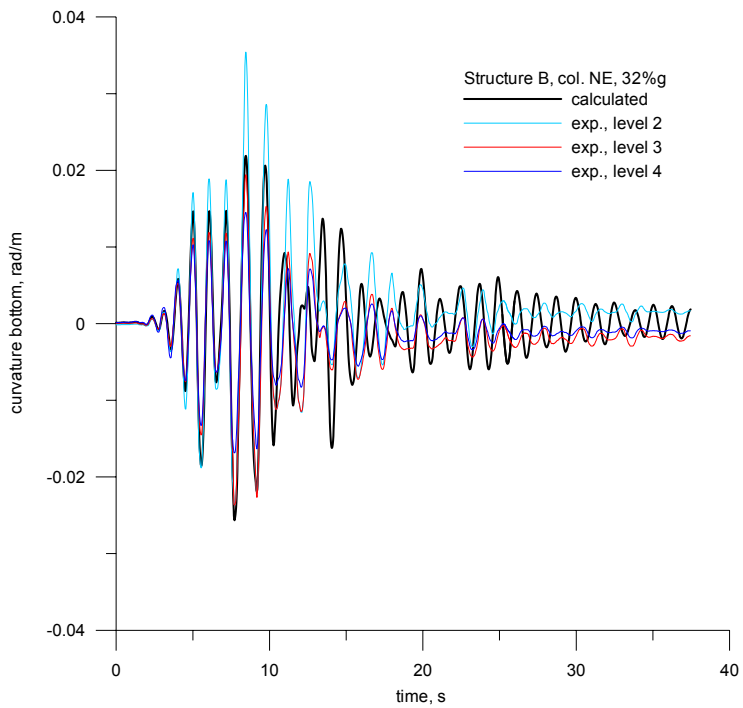

Figure 4.11 a. Curvatures at the bottom of column NE for PGA of 32% *g*

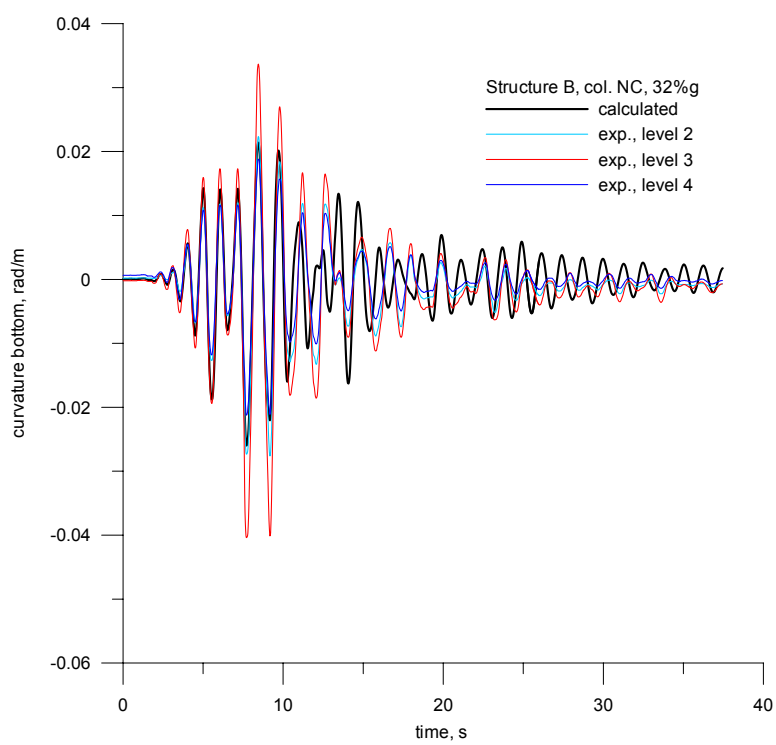

Figure 4.11 b. Curvatures at the bottom of column NC for PGA of 32% *g*

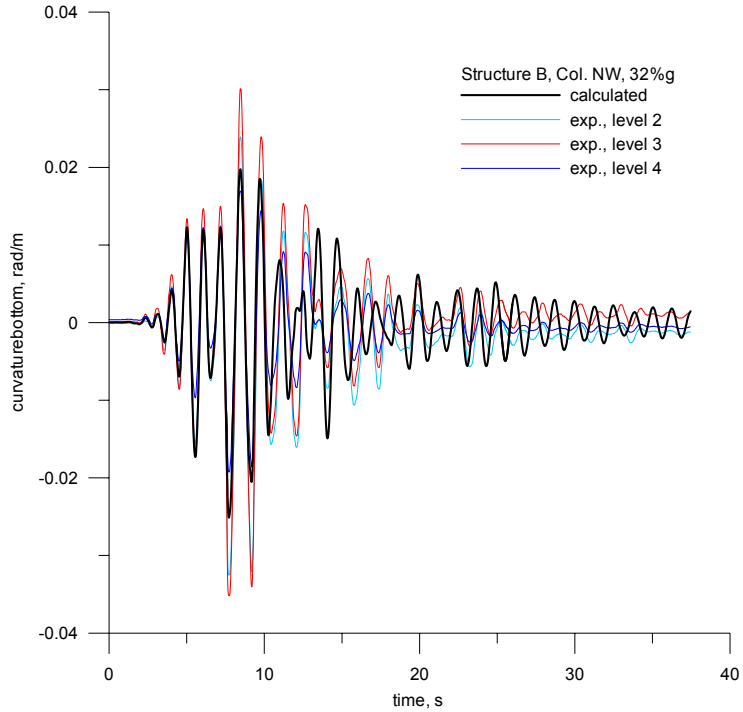

Figure 4.11 c. Curvatures at the bottom of column NW for PGA of 32% *g*

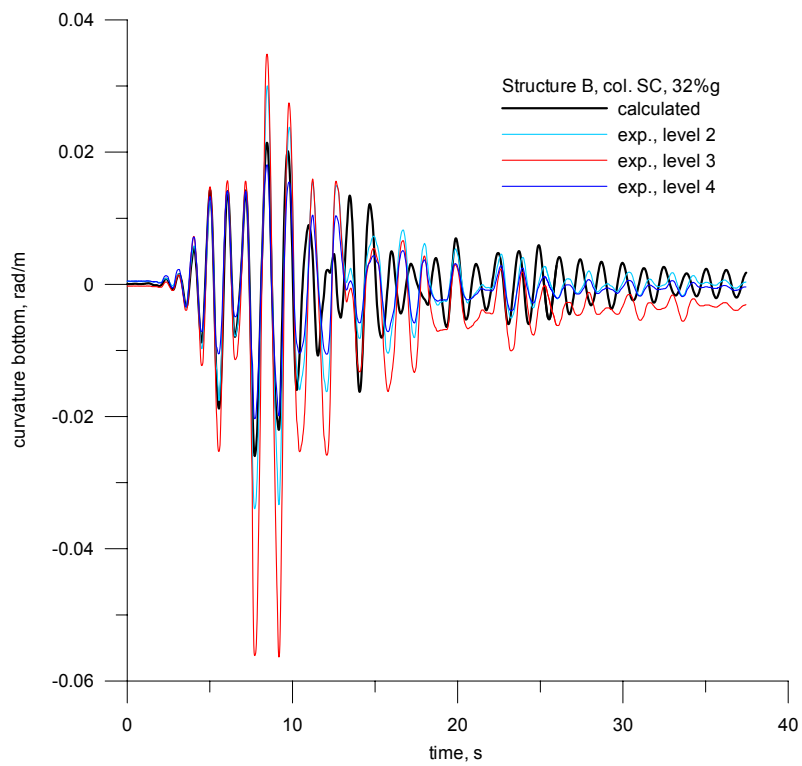

Figure 4.11 d. Curvatures at the bottom of column SC for PGA of 32% *g*

As it can be seen from Figures 11 a, b, c, d, the calculated curvatures coincide well with the experimental ones up to the appearance of yielding. The non-uniform spacing of the confinement contributed to the presence of different curvature excursions at Level 2 and Level 3 – in column NE. The largest excursions are at Level 2, in column NW the curvature excursions at Level 2 are almost equal to those at Level 3, whereas in columns NC and SC the curvature excursions at Level 3 are much larger than those at Level 2.

In Figures 4.12 a, b, c the calculated rotations at the top of the columns NE, NC and NW are compared with the experimental ones.

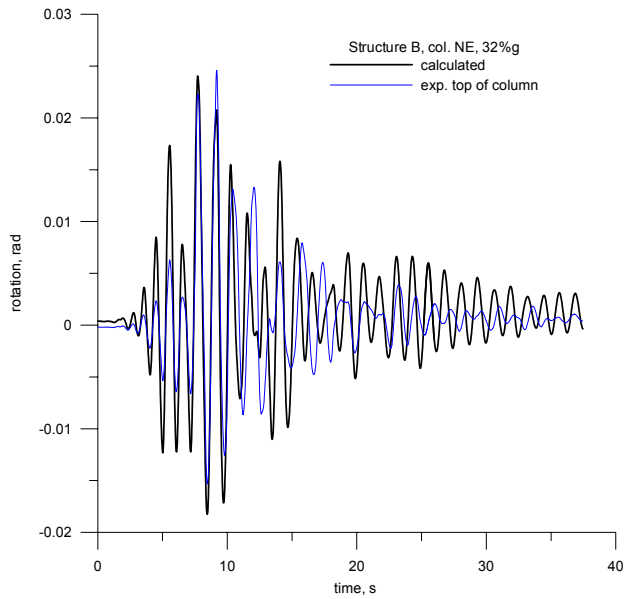

Figure 4.12 a. Rotation at the top of column NE for PGA of 32% *g*

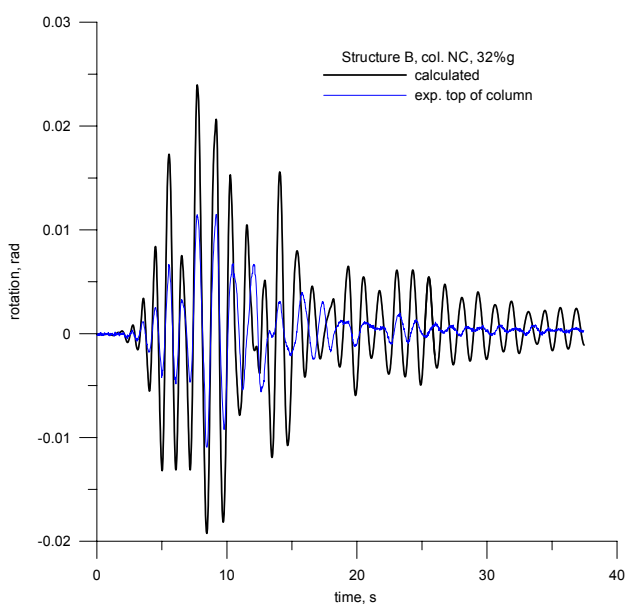

Figure 4.12 b. Rotation at the top of column NC for PGA of 32% *g*

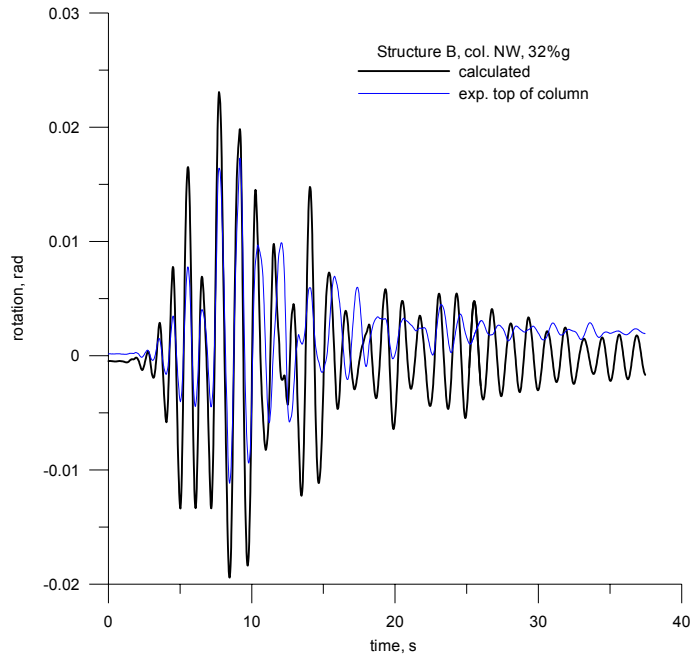

Figure 4.12 c. Rotation at the top of column NW for PGA of 32% *g*

As it can be seen from Figures 4.12 a, b, c column NE experienced the largest top rotations during the test PGA of 32% *g*, caused by wrong anchoring and insufficient cover of the longitudinal reinforcement in the beam-column joint.

4.4.3 Experimental test with PGA of 64% g

During this test the maximum storey displacement of Structure B was 5.6% of the storey height, whereas the corresponding maximum storey displacement of Structure A was 4.2%. As it can be seen from Figure 4.13, the restoring force of Structure B was smaller than that of Structure A due to the smaller strength of the concrete caused by the defective confinement and due to the stiffness degradation and the strength deterioration suffered by the structure during the test with PGA of 32% *g*. The flexural cracks from the previous test enlarged, and new ones appeared in the columns near the plastic hinge regions. No shear cracks or crushing of the concrete was observed. No visible cracks in the beams appeared and no buckling of the longitudinal reinforcement of the columns were observed.

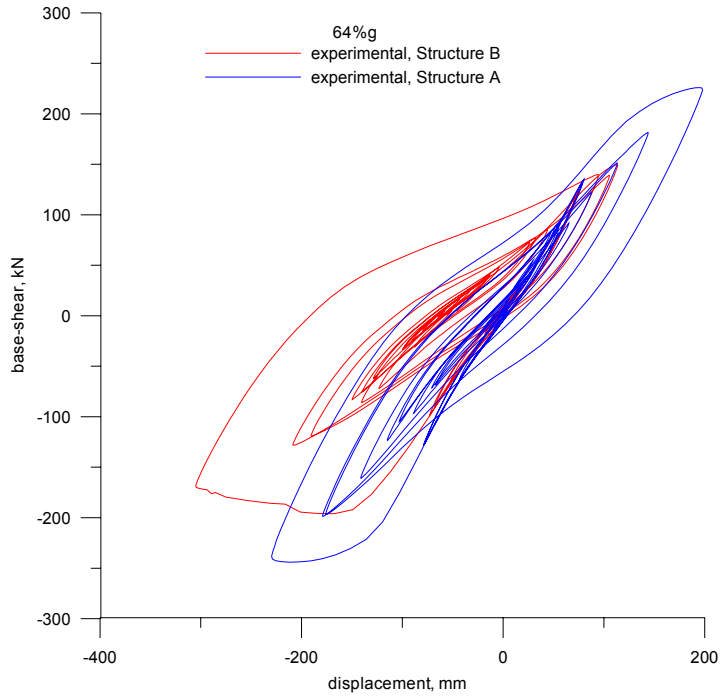

Figure 4.13. Experimental base-shear – storey displacement relationships at PGA of 64% *g*

In Figures 4.14 a and 4.14 b the calculated displacement time history and base shear-storey displacement relationship are compared to the experimental ones, showing good agreement.

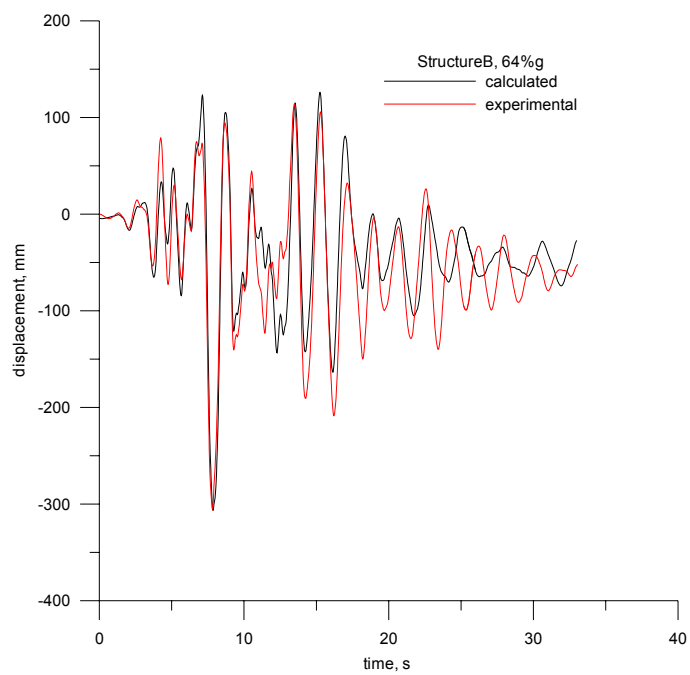

Figure 4.14 a. Displacement time history of Structure B for PGA of 64% *g*

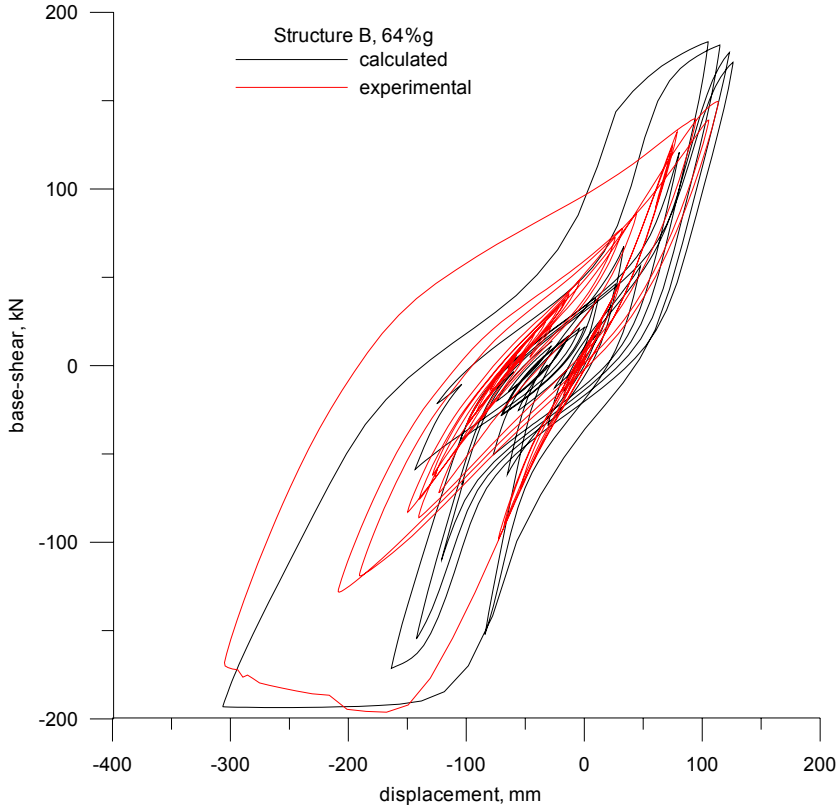

Figure 4.14 b. Hysteresis loops of Structure B for PGA of 64% *g*

In Figures 4.15 a,b,c,d the calculated curvatures at the bottom of the columns are compared with the experimentally obtained mean curvatures at Level 2, Level 3 and Level 4 of columns NE, NC, NW and SC, respectively.

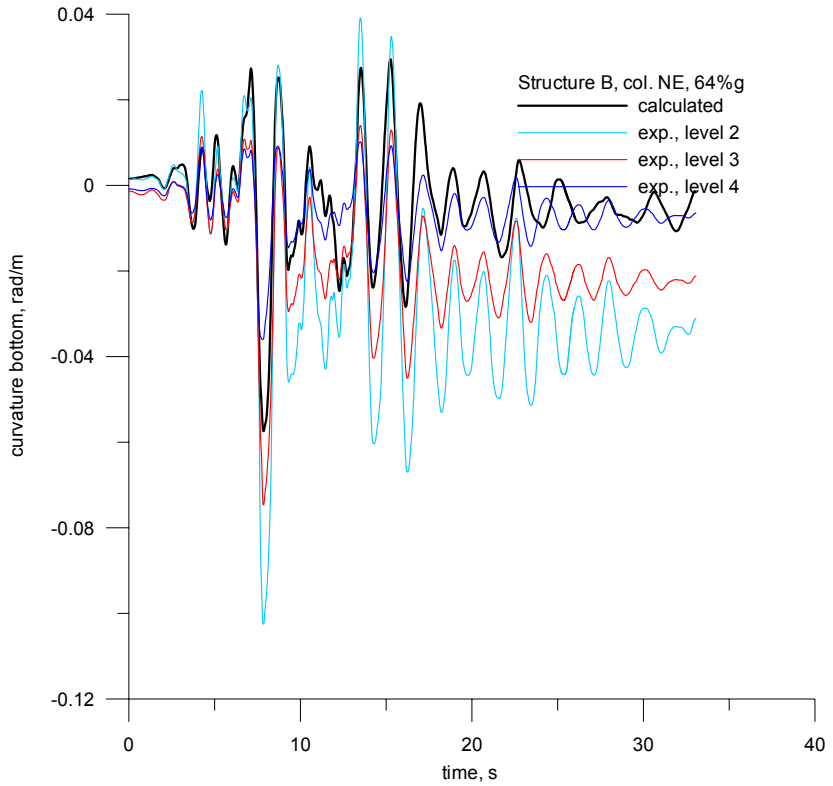

Figure 4.15 a. Curvatures at the bottom of column NE for PGA of 64% *g*

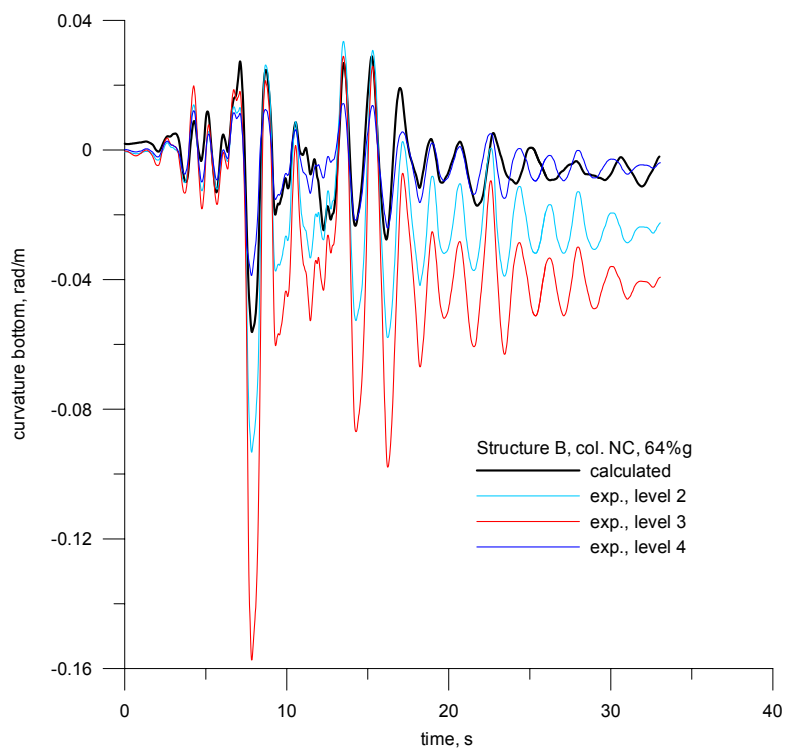

Figure 4.15 b. Curvatures at the bottom of column NC for PGA of 64% *g*

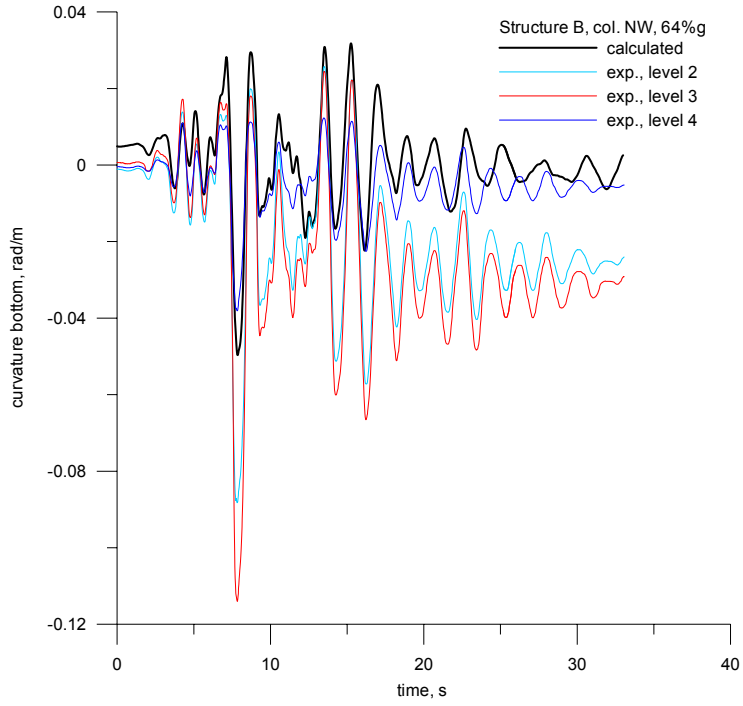

Figure 4.15 c. Curvatures at the bottom of column NW for PGA of 64% *g*

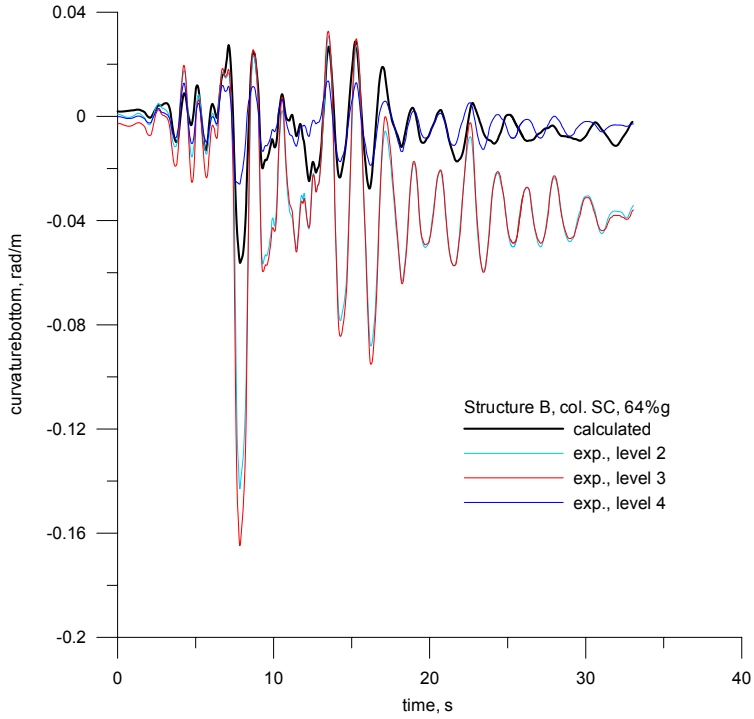

Figure 4.15 d. Curvatures at the bottom of column SC for PGA of 64% *g*

Similarly to the response to the excitation with PGA of 32% *g*, the random spacing of the stirrups caused different curvature excursions at Level 2 and Level 3. In column NE the largest excursions were at Level 2, whereas in columns NC, NW and SC the curvature excursions at Level 3 were larger than those at Level 2. It should be noticed that the maximum measured curvature excursions are close to the maximum measured curvature excursions obtained in Structure A under the excitation with PGA of 80% *g*.

As for the case of Structure A, the calculated curvatures in the advanced stages of structural damage did not coincide properly with the experimental curvatures, since the model did not account sufficiently precisely for the effects of bond deterioration in the joint cores, and also because the zones adjacent to the beam-column or beam-foundation joints were subjected to a strain 'interference' due to the deformation of the adjacent elements.

In Figures 4.16 a, b, c the calculated rotations at the top of the columns are compared with the experimental rotations.

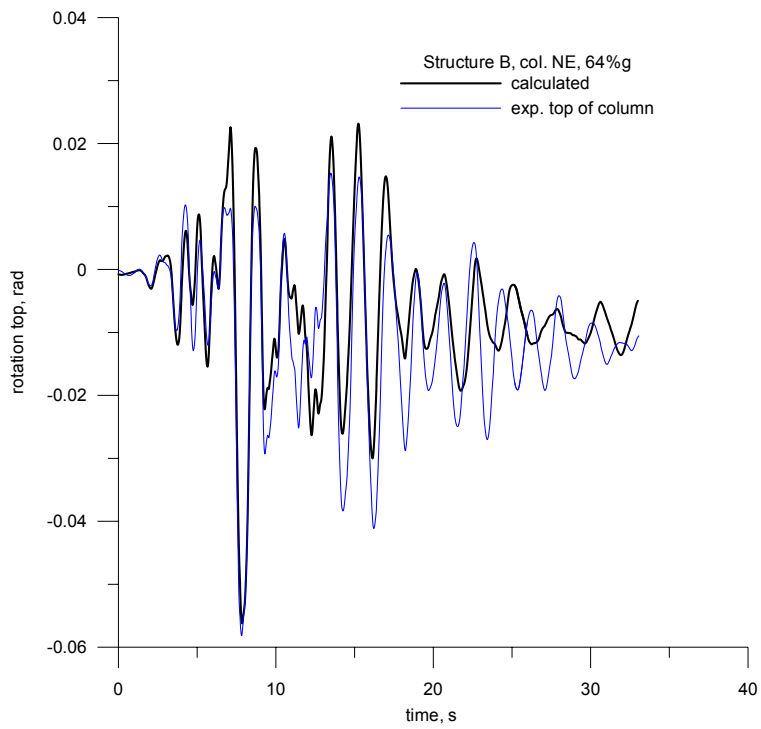

Figure 4.16 a. Rotation at the top of column NE for PGA of 64% *g*

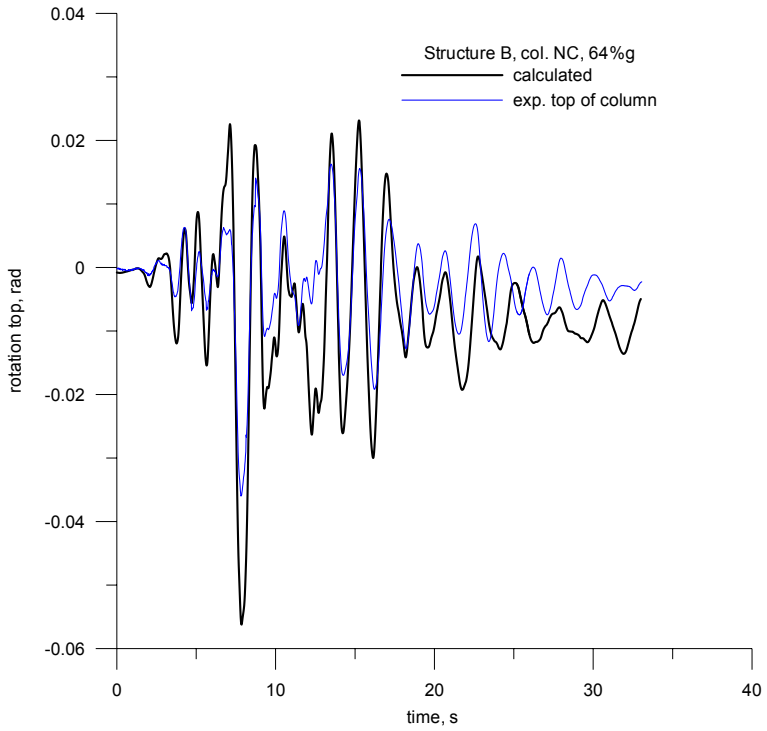

Figure 4.16 b. Rotation at the top of column NC for PGA of 64% *g*

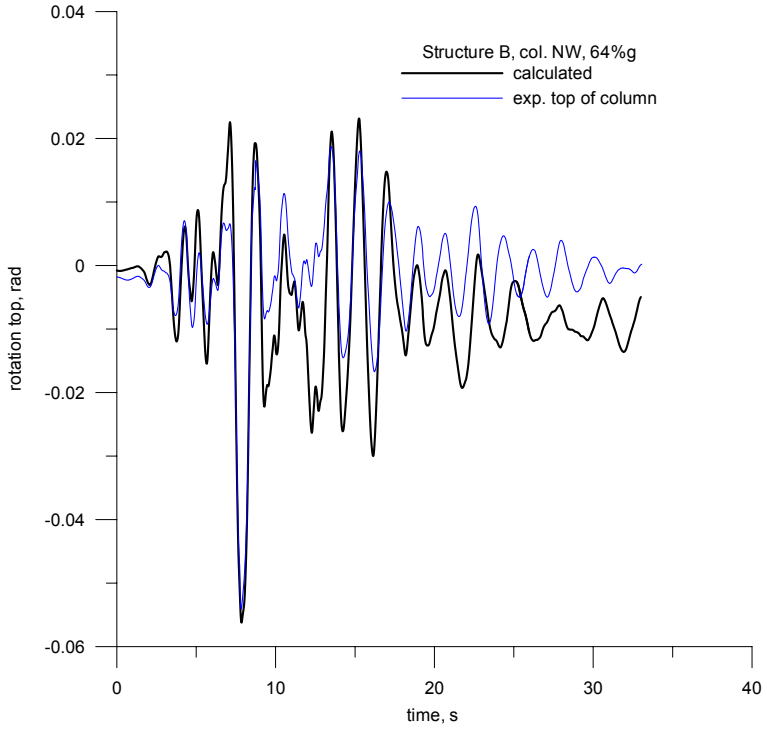

Figure 4.16 c. Rotation at the top of column NE for PGA of 64% *g*

The calculated rotations at the top of the columns coincide relatively well with the experimental rotations, in spite of the case of PGA of 32% *g*. This could be attributed to the modelling assumption that that the deformation of the beam-column joints does not influence the post-yield stiffness of the columns. Obviously, it holds only in case of substantial bond deterioration in the beam-column joints, as in the cases of the response to the excitation with PGA of 64% *g* and the response of column NE to the excitation with PGA of 32% *g*.

4.4.4 Repeated experimental test with PGA of 64% g

During this test the structure was damaged extensively - spalling of the concrete cover and crushing of the concrete in the compression zones were observed, moreover, buckling of the longitudinal reinforcement occurred at the bottom of the central columns on their west sides and at the top of all the columns except column NE. The latter developed a 'hinge' mechanism due to the total disintegration of the longitudinal reinforcement from the concrete in the east face of the beam-column joint. The maximum storey displacement was 7.3% of the storey height. It was close to the value of the maximum storey displacement of Structure A during the test with PGA of 80% *g* (6.8% of the storey height). In Figure 4.17 the recorded hysteresis loops of Structure A and Structure B during the seismic excitation by which they were subjected after the test with PGA of 64% *g* are compared. Being subjected to an excitation with higher intensity (PGA of 80% *g)*, Structure A exhibited much hysteretic energy dissipation capacity, whereas under the repeated excitation with PGA of 64% *g* Structure B demonstrated a substantial reduction in maximum resisting force, reloading slope and hysteretic energy dissipation capacity in comparison to Structure A.

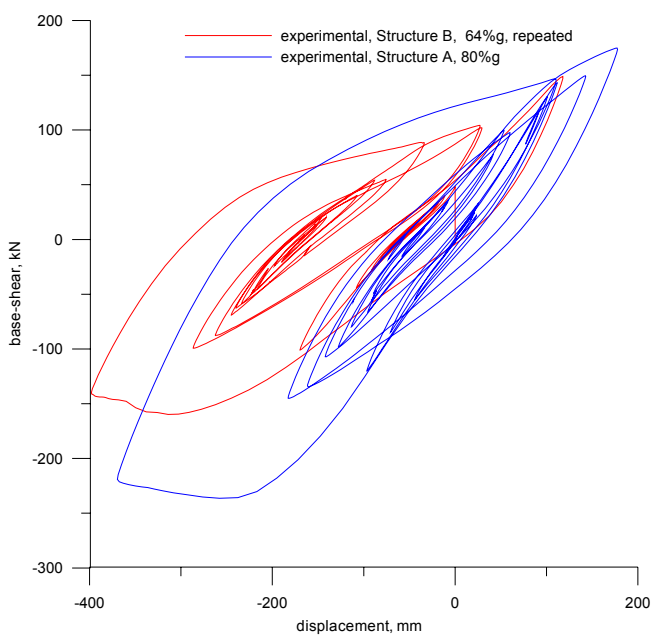

Figure 4.17. Experimental base-shear – storey displacement relationships at PGA of 64% *g* (Structure B) and 80% *g* (Structure A)

The records of the relative displacements available for the bottom of the instrumented columns were used to examine the buckling of the longitudinal reinforcement. Since buckling occurred at Level 2 and Level 3 (see Figure 4.1), the data were considered jointly and are marked by 'Level 2-3'. From the relative displacements (corrected for the level of the longitudinal reinforcement) the strain time histories were obtained and the strain-stress relationships for the longitudinal reinforcement were calculated using the experimental properties of the steel (see Appendix A). The maximum inelastic excursions $\varepsilon_{i\max}$, the moments of their onset (t_{beg}) and end (t_{end}) and the duration (t_{dur}) are shown in Table 4.7. The cases of buckling are marked by shading.

Table 4.7. Maximum inelastic strain excursions of the longitudinal reinforcement at Level 2-3.

Column	Side	$\varepsilon_{i\max}$	t_{beg},s	t_{end},s	t_{dur},s
		East side			
NE	NE	-0.00203	7.46	7.64	0.18
NE	SE	-0.00509	7.44	8.1	0.66
NC	NE	-0.00706	7.42	8.12	0.7
NC	SE	-0.00193	7.44	7.62	0.64
NW	NE	-0.00121	7.5	7.6	0.09
NW	SE	-0.00097	7.5	7.58	0.07
SC	NE	-0.00906	7.4	8.08	0.68
SC	SE	-0.0039	7.44	8.12	0.68
		West side			
NE	NW	-0.0085	8.38	8.98	0.6
NE	SW	-0.0086	8.4	8.98	0.58
NC	NW	-0.0178	8.34	8.98	0.64
NC	SW	-0.0172	8.34	9	0.66
NW	NW	-0.0109	8.36	8.98	0.62
NW	SW	-0.0033	8.52	8.98	0.46
SC	NW	-0.0236	8.3	8.96	0.66
SC	SW	-0.0225	8.32	8.98	0.66

The comparison of the maximum inelastic strain excursions shows that the occurrence of buckling could be correlated to the plastic strain excursions in the order of 0.017 and higher. These excursions appeared during the time period 8.3 s $\leq t \leq$ 8.98. The part of the base-shear – storey displacement hysteresis relationship corresponding to this time period is marked in Figure 4. 18.

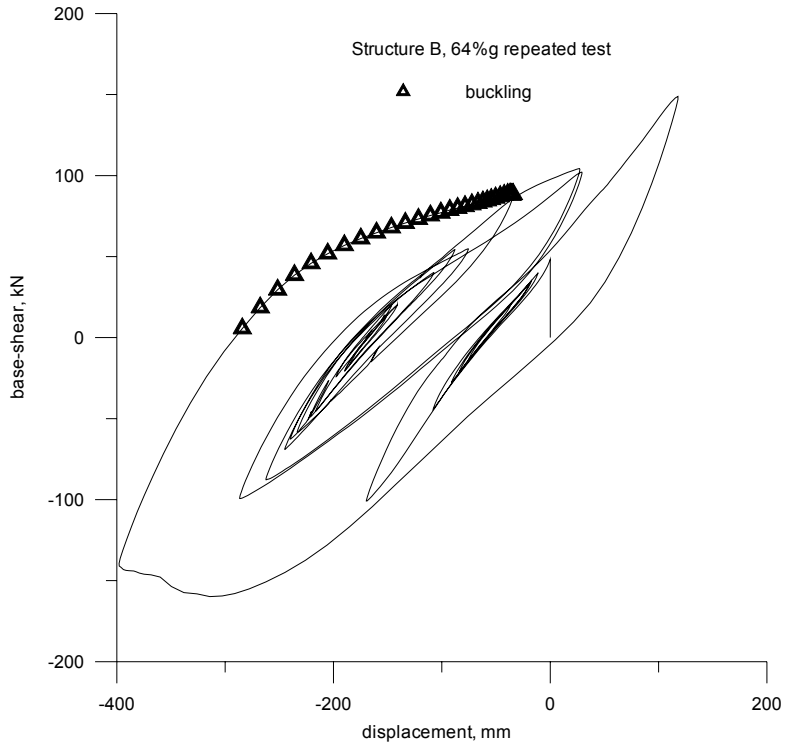

Figure 4.18. Buckling at the bottom of central columns

As it can be seen from Figure 4.18, the occurrence of inelastic buckling of the longitudinal bars at the bottom of the central columns cannot be correlated to the maximum structural response. It is associated with low values of the base shear, ranging between 18 and 81 kN, as well as with values of the storey displacement ranging between 0.284 and 0.037 m.

4.5. Ductility supply and behaviour factor for Structure B

4.5.1 Evaluation of the yield displacement

The storey displacement x_{1y} corresponding to the first yielding in the structure was estimated from the experimental data by use of the records of the relative displacements in the bottom part of the columns and the rotations recorded in top of the columns during the test with PGA of 32% *g*. The mean strains at Level 2 and Level 3 at the bottom of the columns were obtained from the records of the relative displacements corrected for the depth of the concrete cover and compared to the yielding strain in the longitudinal bars ε_{1y} calculated by use of Eq. (3.8), as described in section 4.4.2. The results show that the first yielding appeared at t = 7.55 s at the bottom of the column NC. The absolute rotations at yielding at the top of columns NE, NC and NW were estimated from the records of the absolute rotations, under the assumption that the moments at the top of the columns are proportional to the horizontal displacement of the floor slab up to the first yielding, as described in section 4.3.2. It was proved that the first yielding appeared at t = 7.54 s at the top cross-section of column NE. In this way, the first yielding in Structure B appears at t = 7.54 s and at this moment the recorded storey displacement is x_{B1y} = 0.0956 m and the recorded base shear corresponding to the first yielding is F_{B1y} = 188.7 kN. It should be underlined that the design base-shear strength F_d = 192.9 kN [3] is larger than F_{B1y} and this means that Structure B exhibits 'understrength'. The comparison of x_{B1y} and F_{B1y} to the respective values for Structure A shows that in the considered case the deficiencies of construction decreased the first yield displacement by 27% and the corresponding base shear force by 12%.

Yield displacements according to the criteria for the reduced stiffness equivalent elasto-plastic yield [23] (shown in Figure 27 a) and equivalent elasto-plastic energy absorption [23, 9] (shown in Figure 27 b) were applied to the experimental capacity curve and shown in Table 4.8. There the yield displacement obtained from the expression for the chord rotation at yield [15,16] specified by Eq. (3.2) is also presented. The results obtained from Eq. (3.2) show that the column NC had the smallest chord rotations at yield.

Table 4.8. Yield displacements and displacement ductility supplies

Method		x_y, m	F_y, kN	x_u, m	μ_δ
Experimental	x_y as first yield displacement.	0.0956	188.7	0.304	3.18
	x_y from the equivalent elasto-plastic yield.	0.0793	199.9	0.304	3.83
	x_y from the equivalent elasto-plastic energy absorption.	0.0746	199.9	0.304	4.08
Use of formulae for θ_u and θ_y	Eurocode 8 and Italian code.	0.0883	-	0.390	4.42
	Panagiotakos and Fardis.	0.0883	-	0.373	4.22

As it can be seen from Table 4.8, the obtained experimental first yield displacement is larger than the experimental yield displacements estimated by use of the criteria for the equivalent elasto-plastic yield (17% difference) and the equivalent elasto-plastic energy absorption (22% difference). As in the case of Structure A, these criteria underestimate the capacity of the considered structure at yield. The yield displacement estimated from the chord rotation at yield underestimates the experimental first yield displacement by 8% and gives the result closest to the experimental data.

4.5.2 Estimation of structural ultimate capacity

In Figure 4.19 the envelope of the base-shear – storey displacement relationships, recorded during the experimental tests is shown.

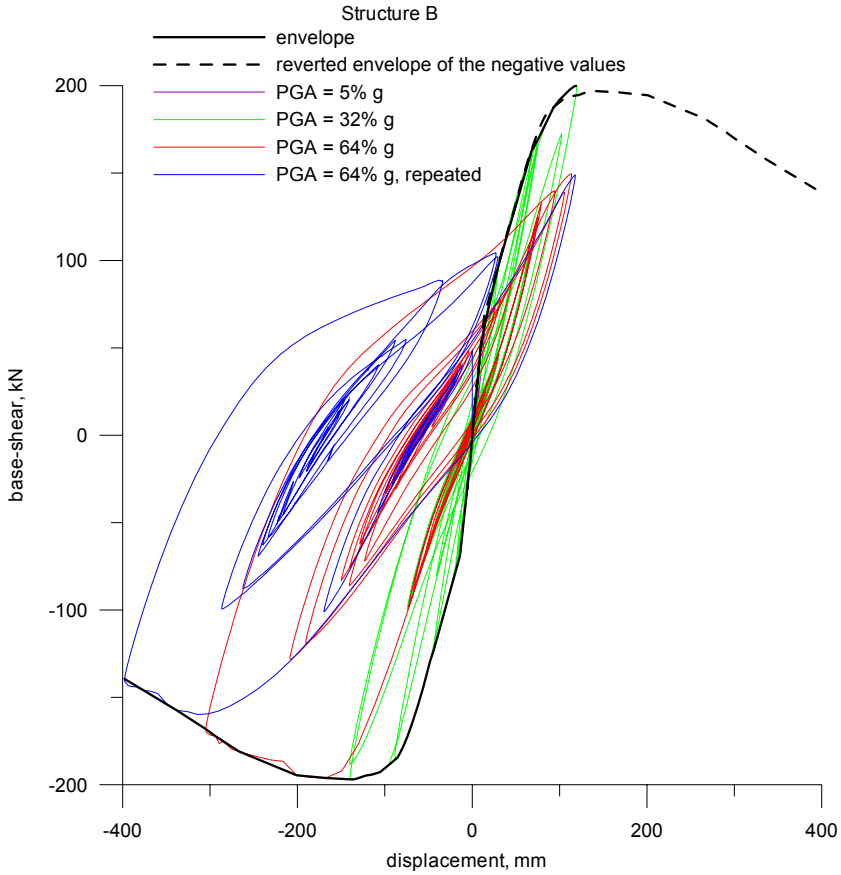

Figure 4.19. Envelope of the recorded hysteresis loops

Similarly to the case of Structure A, during the seismic excitations with highest intensity (PGA of 64% *g* and PGA of 64% *g* repeated) Structure B exhibited only one large hysteretic loop, due to the relatively short effective duration of the seismic excitation and due to the influence of the P-delta effects. Despite the lack of high amplitude cycling, considerable strength degradation took place during the tests with PGA of 64% *g*. The capacity curve (envelope curve of the base-shear – storey displacement relationship), obtained by use of all the experimental data is shown in Figure 4.20.

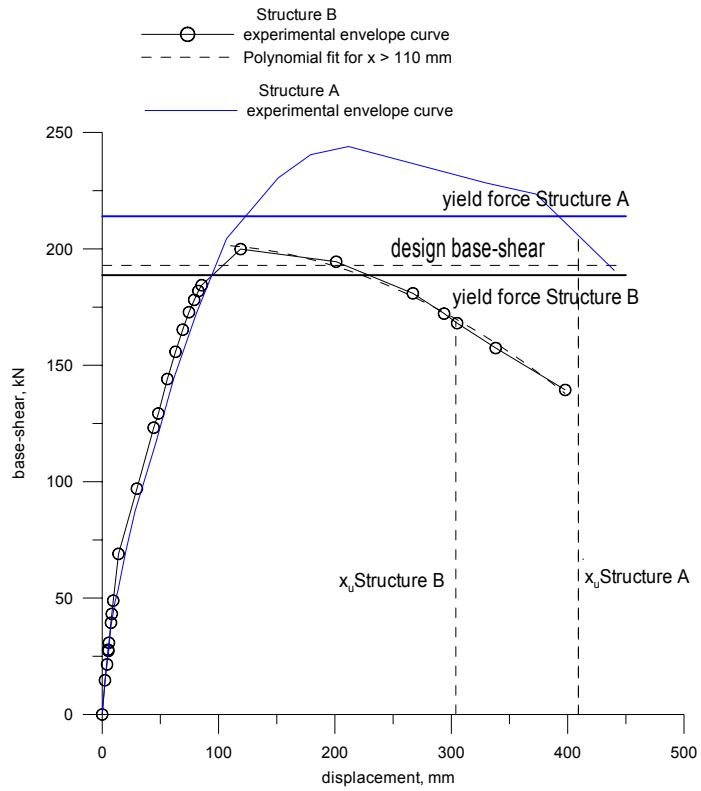

Figure 4.20. Capacity curves of Structure A and Structure B

As shown in Figure 4.20, the data points of the descending branch (x < 110 mm) are fitted by the equation:

$$F(x) = -0.00062x^2 + 0.0943x + 198.5 \qquad (4.4.1)$$

where

F is the base-shear in kN,
x is the storey displacement in millimetres.

The ultimate storey displacement x_u was estimated as corresponding to a 15% drop in the peak base-shear force [16, 22, 23]. Since the experimentally measured maximum base-shear force F_{max} was 199.9 kN, from Eq.(4.4.1) x_u was calculated as 0.304 m. As it can be seen from Figure 4.19, the ultimate displacement belongs to the part of the capacity curve determined by the test with PGA of 64% g. The inelastic buckling of the longitudinal reinforcement appeared during the repeated test with PGA of 64% g. Consequently, the determination of the ultimate displacement as corresponding to 15% decrease of the peak base-shear force provides a conservative estimate of the ultimate state of the structure with respect to the appearance of inelastic buckling.

In Figure 4.20 the experimental capacity curves of Structure A and Structure B are compared. In the range of base shear of order of 20 kN, the stiffness of Structure B is a little smaller than that of Structure A, mainly because of the additional rotations of the

beam-column joints. For base-shear larger than 20 kN up to yield force of Structure B, the difference in the stiffness of the two structures is dictated mainly by the influence of the confinement in the strength and stiffness of the concrete. Similar differences of the experimental capacity curves of two-story RC frames with different levels of confinement of the concrete were obtained in [22]. The maximum base-shear of Structure B was 22% smaller than that of Structure 1, and the ultimate storey displacement of Structure B was 34 % smaller than that of Structure B.

The ultimate displacement of Structure B was also estimated by use of empirical formulae for the ultimate chord rotation of RC members in terms of their geometric and mechanical characteristics. The ultimate chord rotation θ_u according to Eurocode 8 [10] and new Italian Code [15] was estimated by use of Eq.(3.5) and according to Panagiotakos and Fardis [16] by use of Eq. (3.7). In Table 4.9 the ultimate chord rotations and ultimate storey displacements calculated according to Eq. (3.5) and Eq.(3.7) are presented.

Table 4.9. Ultimate chord rotations and storey displacements

	Eurocode 8 and Italian code		Panagiotakos and Fardis	
	θ_u	x_u, m	θ_u	x_u, m
lateral columns	0.0745	0.406	0.0838	0.393
central columns	0.0717	0.390	0.0685	0.373

The smaller concrete cover of column NC influenced insignificantly the calculated ultimate chord rotations. Similarly to the case of Structure A, the ultimate limit state was defined by the failure of the central columns. The ultimate storey displacement x_u = 0.373 m calculated according to Panagiotakos and Fardis [16] is closer to the experimentally determined one than those according to [10,15], showing a 23% difference. Recalling the results for Structure A, the empirical formulae exhibited very good coincidence with the experimental results (1% difference with the formula of [10,15]). The above comparison shows that the considered empirical formulae for ultimate chord rotation of RC members provide very good estimate of the ultimate state for structures with good quality of construction. In case of structures with serious deficiencies in the execution the considered empirical formulae overestimate the ultimate capacity of RC members.

4.5.3 Ductility supply of the structure

The displacement ductility supply μ_δ of the structure was estimated by Eq. (3.9) as the ratio between the ultimate and yield displacements. The experimentally obtained displacement ductility supply is μ_δ = 3.18. It should be noticed that it almost coincides with the displacement ductility supply of Structure A (μ_δ = 3.18), but in the considered case such a value is obtained as the ratio of two smaller quantities, the ultimate and the yield displacement. In Table 4.8 the experimental μ_δ is compared to the ductility supplies obtained by the other methods considered. The displacement ductility supplies obtained by use of the criteria for the reduced stiffness equivalent elasto-plastic yield [23] and

equivalent elasto-plastic energy absorption [23, 9] gave larger estimates due to the underestimation of the yield displacement of Structure B discussed in section 4.5.1. The use of the formulae given in Eurocode 8 [10] and the new Italian Code [15] and Panagiotakos and Fardis [16] chord rotations at yield and at the ultimate provided slightly conservative, but well coinciding with the experimental result estimates for Structure A. As it can be seen from Table 4.8 the above expressions overestimate by 39% and 33%, respectively, the experimentally obtained displacement ductility supply of Structure B.

In Table 4.10 the curvature ductility factors of the bottom cross-sections of the columns for the seismic excitation with PGA of 64% *g* are presented.

Table 4.10. Curvature ductility factor supply at the bottom cross-sections of the columns

Column	Segment	maximum curvature excursions (rad/m)	curvature ductility
NE	Level 2	0.1306	6.629
	Level 3	0.08515	4.322
	Level 4	0.04514	2.291
NW	Level 2	0.10815	5.49
	Level 3	0.1320	6.701
	Level 4	0.0490	2.487
NC	Level 2	0.1195	6.224
	Level 3	0.1788	9.313
	Level 4	0.0512	2.667
SC	Level 2	0.1663	7.995
	Level 3	0.1904	9.154
	Level 4	0.0374	1.798

They are obtained on the basis of the experimental maximum curvature excursions and the yield curvatures used in the numerical model (see Table 4.1). In view of the fact that at this excitation level Structure B reached its ultimate limit state, the curvature ductility factors shown in Table 4.10 could be considered as the curvature ductility factor supply. Since the relationship between the local and global ductility factors according to [26] is $\mu_\varphi = 2\mu_\delta - 1$, and the measured displacement ductility supply is μ_δ = 3.18, the required minimum curvature ductility supply is μ_φ = 5.36. As it can be seen from Table 4.10, for all the columns the curvature ductility supply measured at Level 2 comply with this requirement.

4.5.4 Behaviour factor supply of the structure

The behaviour factor supply was estimated according to the direct use of the Eurocode 8 definition discussed in section 3.4.4, *i.e.* as the ratio of the 'would-be' base-shear force obtained by linear elastic analysis F_{el} to the minimum seismic force that may be used in design – with a conventional elastic analysis model – still ensuring a satisfactory response of the structure. The considered structure exhibited 'understrength', i.e., the experimental base shear corresponding to the first yielding F_{B1y} was 188.7 kN, whereas the design base-shear strength F_d was 192.9 kN. For this reason F_{B1y} was considered as the minimum seismic force still ensuring a satisfactory response of the structure. Since during the experimental test with PGA of 64% *g* the maximum displacement was $x_{\max} = 0.305m \approx x_u$, it can be accepted that Structure B reaches x_u at PGA of 64% *g*. Using the value of the acceleration response spectrum of the experimental accelerogram for the experimental natural period of 0.73 s and PGA of 64% *g,* the 'would-be' elastic base-shear force F_{el} was estimated as 805.5 kN. The corresponding value of the behaviour factor supply of Structure B is q = 4.27. It is 35% less than the behaviour factor supply of Structure A and does not match the behaviour factor demand of 4.95 of Eurocode 8. Consequently, the behaviour factor supply of structures decreases substantially due to the deficiencies of the construction, therefore the modern codes for seismic design, which imply high behaviour factor demands should provide special requirements for the quality of construction. Eurocode 8 prescribes that 'in cases, where a special and formal Quality System Plan is applied to design, procurement and construction in addition to normal quality control schemes, increased basic values of the behaviour factor may be allowed. The increased values are not allowed to exceed the values given by more than 20%.' The present study proves that the lack of special control only during the construction resulted into a reduction by 35% the behaviour factor supply. In this context, it would be reasonable to introduce in Eurocode 8 a requirement for special measures concerning the quality of construction, when implementing the ductility class 'High'.

4.6. Vulnerability analysis

Fragility of Structure B was estimated by use of the method described in section 3.5.1 and the twenty accelerograms generated for fragility analysis of Structure A. Similarly to the case of Structure A, the maximum storey displacement was considered as seismic response parameter, since it relates directly the ultimate limit state defined by the ultimate storey displacement x_u. PGA was chosen as seismic intensity parameter, since the experimental tests were related to its value. The response of Structure B was calculated for three different levels of seismic intensity: PGA of 5% *g*, 32% *g* and 64% *g* by use of the models of the structure created to best fit the experimental behaviour for the corresponding intensities. In Figure 4.21 the standard deviations of the studied seismic response parameter for all the considered PGA are shown. They stabilize over the chosen number of generated accelerograms thus demonstrating that such number is sufficient.

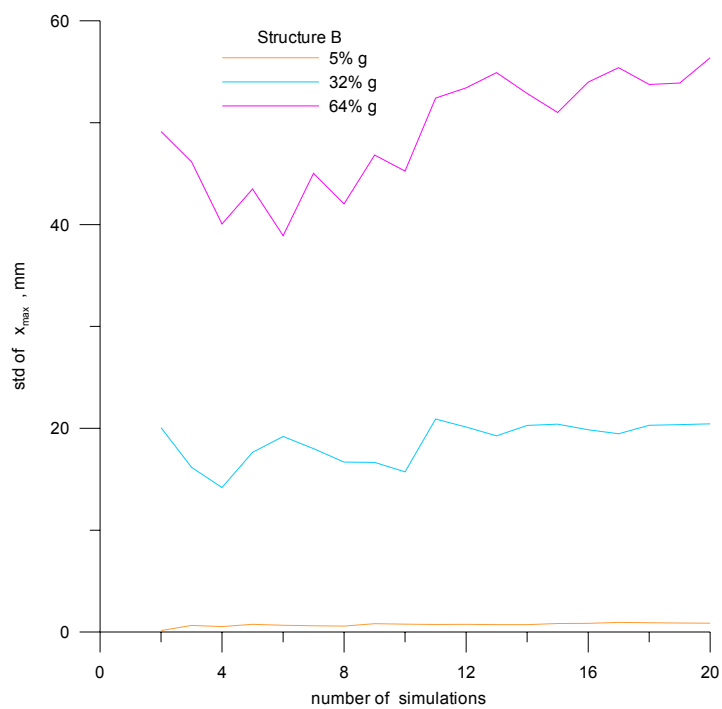

Figure 4.21. Standard deviations of the seismic response parameter

In Figure 4.22 a the values of the seismic response parameter obtained by the numerical simulations are shown.

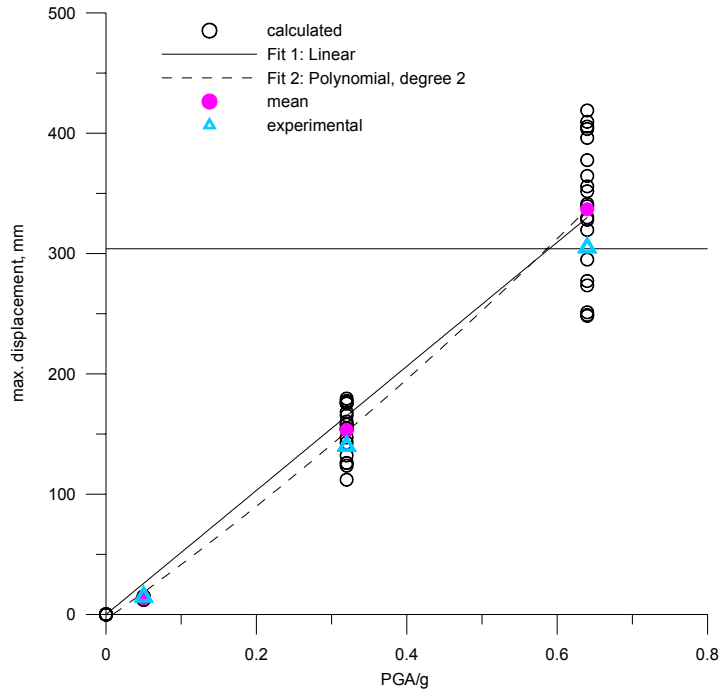

Figure 4.22 a. Maximum storey drifts at different PGAs

The functional relationship between the seismic response parameter and the seismic intensity is represented by two different fits (denoted by fit 1 and fit 2) exhibiting high values of the coefficient of determination R_d^2, as shown in Table 4.11.

Table 4.11. Fits of the calculated responses

	Equation	R_d^2	Dimensions	
			argument	function
Fit 1	$x = 515.61y$	0.973	PGA/g	mm
Fit 2	$x = 143.024y^2 + 441.535y - 4.046$	0.955	PGA/g	Mm
Fit 3	$OSDI = 1.973y^2 + 0.1585y + 0.0111$	0.976	PGA/g	-
Fit 4	$DI_{hrc} = -0.7086(ISD\%)^2 + 17.339ISD\% + 0.1523$	0.999	-	-

The two fits exhibit close values near the ultimate displacement at PGA of 0.0.59 *g*, as it can be seen in Figure 4.22a. The comparison of the two fits with the experimental maximum displacements demonstrates the influence of the high amplitude cycling on the ultimate limit state, since under the generated accelerograms the structure reaches the ultimate displacement at lower value of PGA (0.59 *g*), than during the experimental tests (0.64 *g*).

For the case of Structure A, the assessment of the fit, which represents better the structural behaviour over a wider range of seismic intensity was done on the basis of the estimation of the PGA at yielding. The simulations of the response of Structure B to the generated accelerograms did not supply a reliable estimate of the PGA at yielding. The most probable reason for this is the smaller number of seismic intensities in comparison with structure A, at which the response to the generated accelerograms was calculated.

Finally, the non-linear functional relationship between the seismic response parameter and the seismic intensity (fit 2) was chosen as predictive equation for the fragility analysis, since it matches better the mean displacements at all the considered seismic intensities (see Figure 4.22 a).

In Figure 4.22 b the functional relationships between the maximum storey displacement and PGA for Structure A and Structure B are compared.

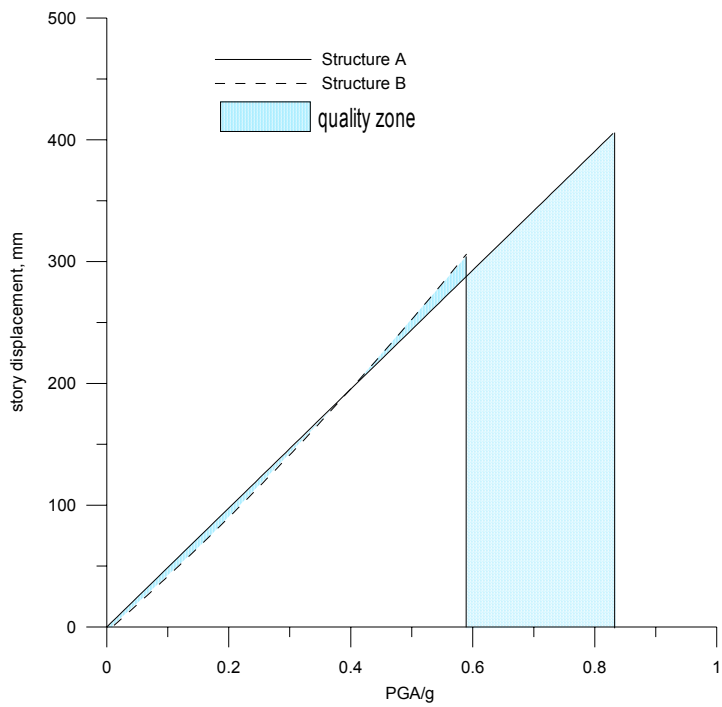

Figure 4.22 a. Maximum storey displacements of Structure A and Structure B over PGA

As it can be seen from this figure, the quality of construction does not influence substantially the maximum structural response. Up to the PGA for which Structure B reaches the ultimate limit state, the largest difference between the responses of the two structures is in the order of 5%. However, there is a significant difference between the capacities of the two structures to sustain high intensity seismic excitations. The enhanced ductility of Structure A supplies much larger ultimate storey displacement, and in this way made it possible to sustain 40% larger PGA.

The mean values, the standard deviations (st.d.), the coefficients of variation (c.o.v.), the median values and the lognormal standard deviations (l.st.d.) of the simulated maximum storey displacements for the considered levels of PGA are presented in Table 4.12.

Table 4.12. Statistical characteristics of the simulated seismic response parameter

PGA/*g*	mean, m	st.d., m	c.o.v.	median, m	l.st.d.
0.05	0.0134	0.00087	0.0646	0.0134	0.0646
0.32	0.1533	0.02438	0.1590	0.1514	0.1581
0.64	0.3368	0.05638	0.1674	0.3322	0.1662

As it can be seen from Table 4.12, the coefficients of variation and the lognormal standard deviations exhibit different values for the considered seismic intensities. As shown in Figure 4.22 c, the functional relationship between the coefficients of variation and the seismic intensity could be represented by a logarithmic fit (denoted by fit 3 in Table 4.11), which exhibits coefficient of determination R_d^2= 0.963.

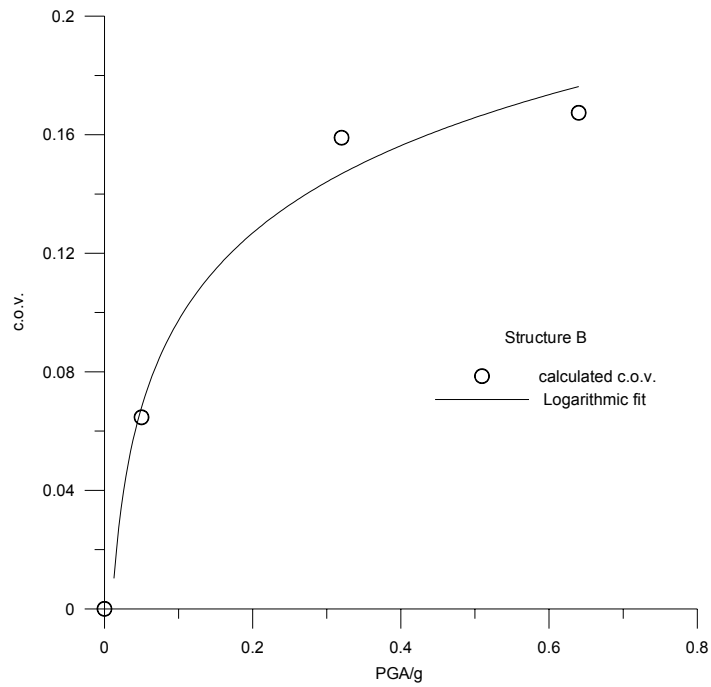

Figure 22 c. Coefficients of variation at different PGAs

Using the above functional relationship, the values of coefficient of variation and the respective lognormal standard deviation were calculated in each intensity step of the fragility analysis of Structure B.

As for the case of Structure A, the models of structure B were obtained by fitting the experimental data and no uncertainty in the median value of the capacity R_m due to limitations in data and approximating in modeling was taken into account in the fragility estimation, *i.e.* β_{us} = 0 (see section 3.5). Also, since the characteristics of the materials were estimated experimentally, the randomness of the seismic capacity β_r was taken as zero. Consequently, in the fragility analysis the randomness in the seismic response parameter affected by the randomness of the seismic excitation was taken into account by considering the intensity dependent coefficient of variation of the seismic response parameter.

In Figure 4.23 the obtained fragility curve of Structure B is presented.

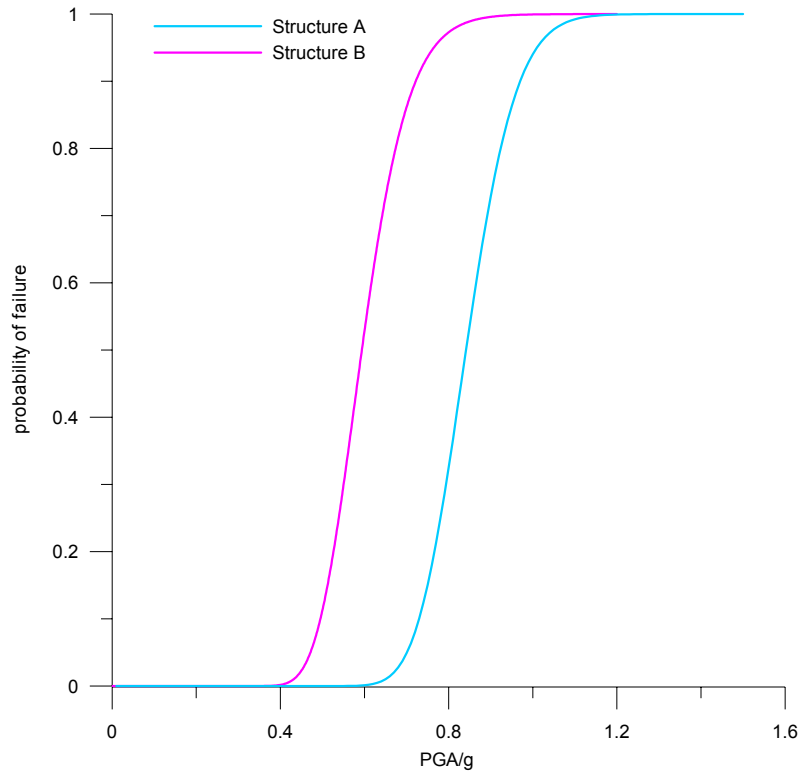

Figure 4.23. Fragility of the considered structures

As it can be seen from Figure 4.23, the conditional probability of failure of Structure B is less than 1% for PGA < 0.431*g*. Structure B will reach the ultimate limit state with provability of 95% at PGA of 0.76 *g*. The comparison of the fragility curves of Structure A and Structure B shows that the deficiency in the construction increased considerably the vulnerability of the structure, since the PGA corresponding to equal probability of failure decreased approximately by 0.25 *g*.

4.7. Qualification of damage grade

The overall structural damage index (OSDI) was obtained during the numerical simulations by IDARC 5.5 on the basis of the modified Park and Ang damage model [13, 40, 42], as described in section 3.6.

In Figure 4.24 a the values of OSDI obtained for the generated accelerograms are shown. The functional relationship between OSDI and the seismic intensity index PGA is presented in Figure 4.24 a, and described as fit 3 in Table 4.11.

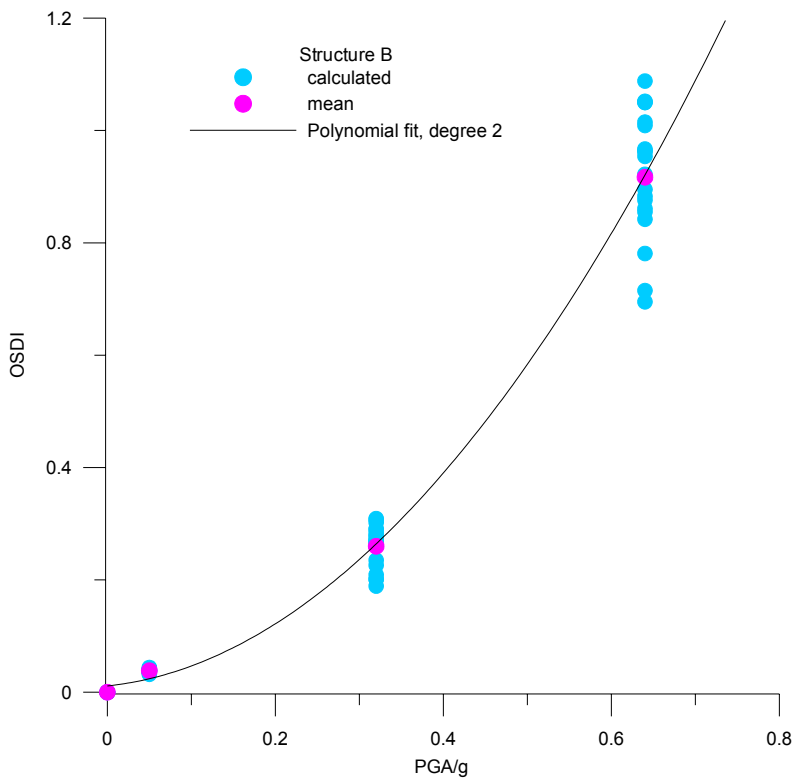

Figure 4.24 a. OSDI for the generated accelerograms

Similarly to the case of Structure A, the maximum interstorey drift (ISD%), expressed in per-cents of the storey height, is considered as another overall structural damage index. In section 4.6, the maximum storey displacement (in the particular case equal to the interstorey drift) is related to PGA of the generated accelerograms and described in Table 4.11 as fit 2.

The damage observed during the experimental tests was related to the homogenized reinforced concrete damage scale damage index (DI_{hrc}) (see for more details section 3.6). Values of 5, 40 and 80 are assigned to DI_{hrc} for the tests with PGA of 5% *g*, 32% *g* and 64% *g*, respectively, according to the homogenized reinforced concrete damage scale for

ductile moment resisting frames shown in Appendix B. In Figure 4.24 b these values of DI_{hrc} are related to ISD% measured during the respective tests. The functional relationship between DI_{hrc} and ISD% obtained by non-linear regression is described in Table 4.11 as fit 4. This functional relationship was used to convert the predictive equation for ISD over PGA obtained from the generated accelerograms to DI_{hrc} over PGA. In this way the calculated damage indices were related to the index, based on observational data.

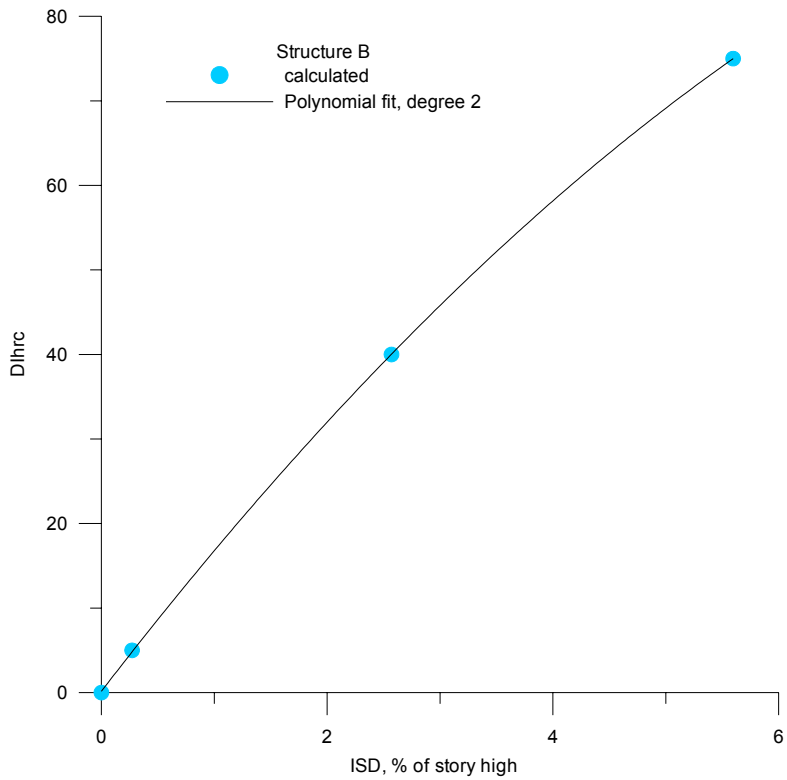

Figure 24 b. Relation between DI_{hrc} and ISD%

The considered damage indices are related to the conditional probability of failure and the damage states of Structure B are expressed in terms of its fragility. The predictive equations for the considered damage indices over PGA are compared to the structural fragility in Figure 4.25. Aiming at a more homogeneous representation of the damage indices, the ISD% is divided by 10 and DI_{hrc} is divided by 100.

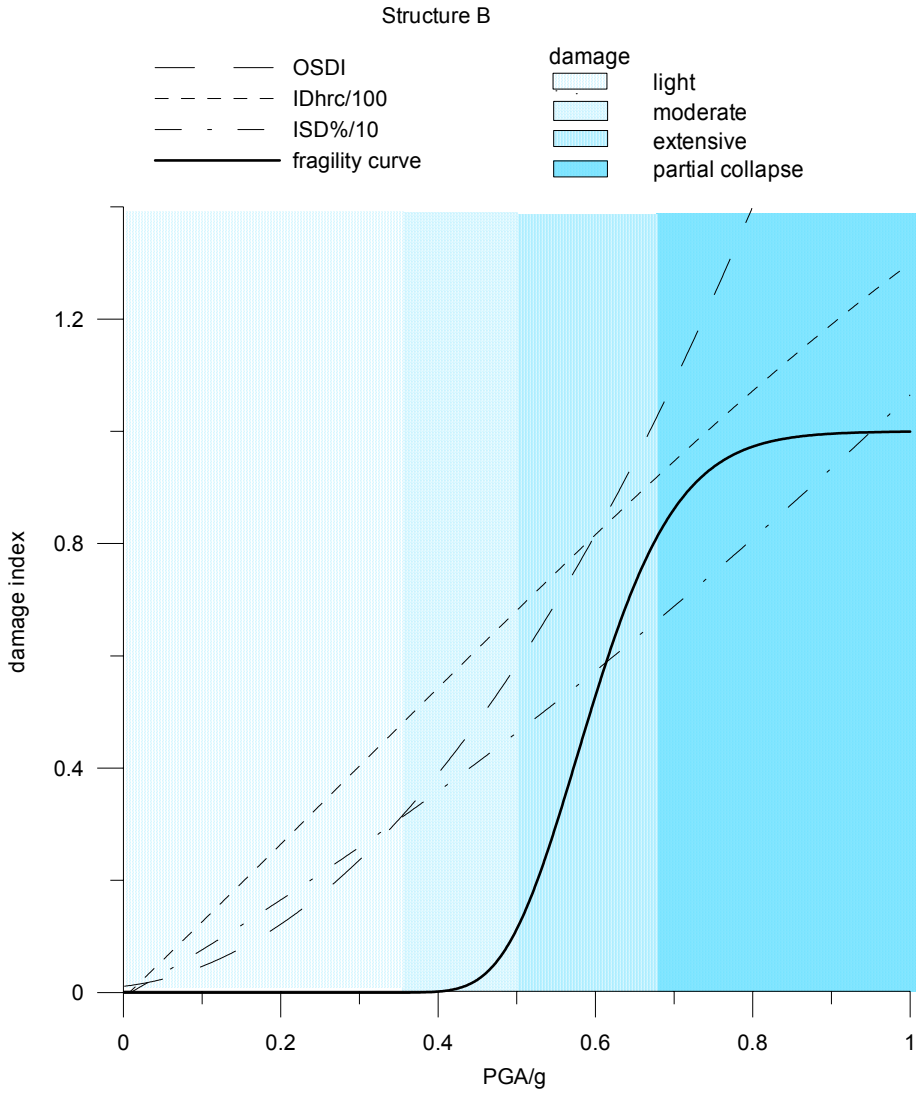

Figure 4.25. Qualification of structural damage grade

As it can be seen from Figure 4.25, a conditional probability of failure of 0.1% corresponds to PGA = 0.39 *g*, OSDI = 0.38, ISD% = 3.5 and DI_{hrc} = 53. As in the case of Structure A, this small probability of failure is related to large values of the damage indices. This result could be explained by the relatively large displacement ductility available (μ_δ = 3.18) and by the relatively steep ambiguous part of the fragility curve, due to the fact that the randomness in the seismic response parameter is affected only by the randomness of the seismic excitation.

In Table 4.13 the relation of the rounded-off values of the studied damage indices is shown, along with probability of failure *Pf*, PGA and structural damage. The description of the damage grade is the same as in [41](see Appendix B).

Table 4.13. Qualification of the structural damage

Pf	PGA/*g*	OSDI	ISD%	DI_{hrc}	Damage grade	EMS, vuln. class D	EMS intensity
$< 10^{-4}$	< 0.35	< 0.3	< 3.2	< 50	Light	Grade 1	≤ VIII
10^{-4} - 10^{-1}	0.35– 0.5	0.3 – 0.6	3.2 – 4.6	50 - 70	Moderate	Grade 2	IX
0.1 – 0.8	0.5–0.67	0.6 – 1.0	4.6 – 6.6	70 - 90	Extensive	Grade 3	X
> 0.80	> 0.67	> 1.0	> 6.6	> 90	Partial collapse	Grade 4	> X

For the considered structure the light and moderate damage levels are connected with very low probability of failure ($Pf < 10^{-4}$). The extensive damage corresponds to the ambiguous part of the fragility curve and the partial collapse would take place at high probability of failure, namely $Pf > 0.8$. This value is smaller than the probability of failure delimiting the partial collapse state of Structure A ($Pf > 0.95$). Since the fragility was estimated taking the storey drift as seismic response parameter, this result could be attributed to the larger values of OSDI and DI_{hrc} for Structure B for one and the same ISD%. The relations of both OSDI and DI_{hrc} , with the storey drift calculated for the generated accelerograms presented in Figure 4.26 show that the deficiencies in the construction affect considerably larger values OSDI and DI_{hrc}.

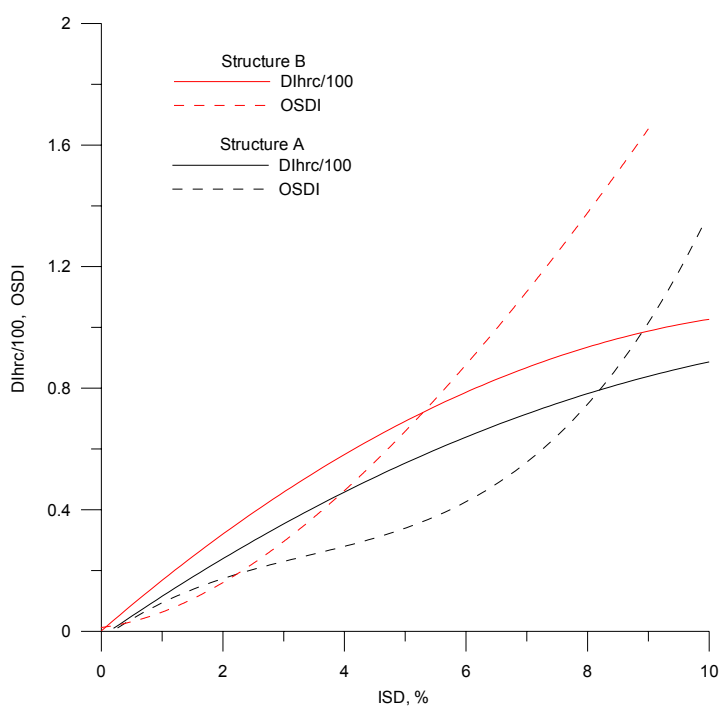

Figure 4.26. Comparison of damage indices

Similarly to the case of Structure A, the values of OSDI connected to the different damage grades agree very well with the definitions of damage state in terms of OSDI based on experimental observations [42, 43, 44]. The values of OSDI delimiting the light, moderate, extensive and partial collapse damage states shown in Table 4.13 fully coincide with the values defined in [42, 43, 44]: OSDI < 0.3 for minor damage, 0.3 <OSDI < 0.6 for moderate damage and 0.6 <OSDI < 1 for extensive damage. Since the description of the damage grade in the present work was based on DI_{hrc} , the above good coincidence proves the existence of a strong correlation between DI_{hrc} and OSDI. In Figure 4.27 the relations between DI_{hrc} and OSDI for Structure A and Structure B obtained from the simulations with the generated accelerograms are shown.

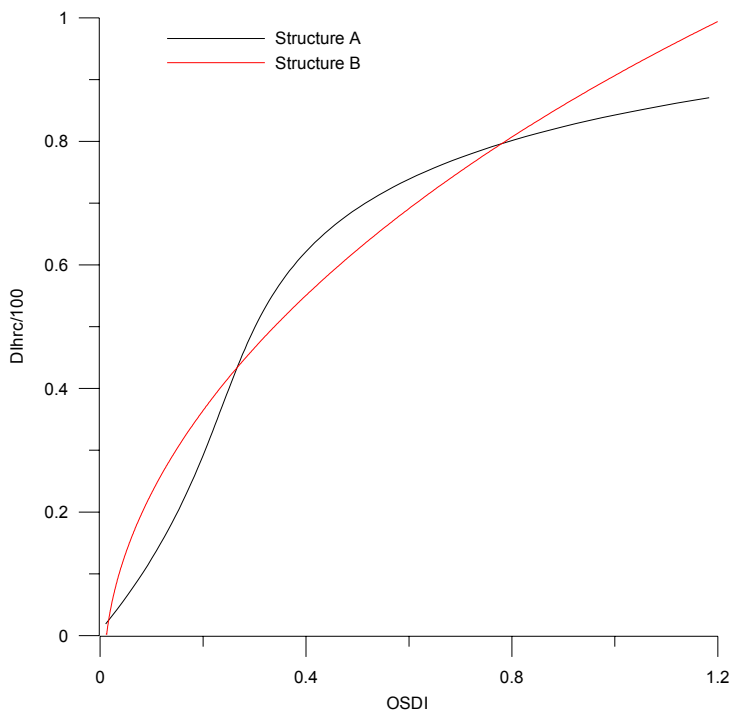

Figure 4.27. Relations between DI_{hrc} and OSDI

The good coincidence between the relationships for the two structures gives reasons for a wider implementation of the calculated values of OSDI for the prediction of the eventual observational damage.

According to the European Macroseismic Scale (EMS) [45], the most likely vulnerability class for the studied industrial structure (frame structure with high level of earthquake resistant design) is the vulnerability class E. This vulnerability class is assigned to Structure A due to its good quality of construction. The obtained damage grades in function of PGA for Structure A and Structure B are compared in Figure 4.28.

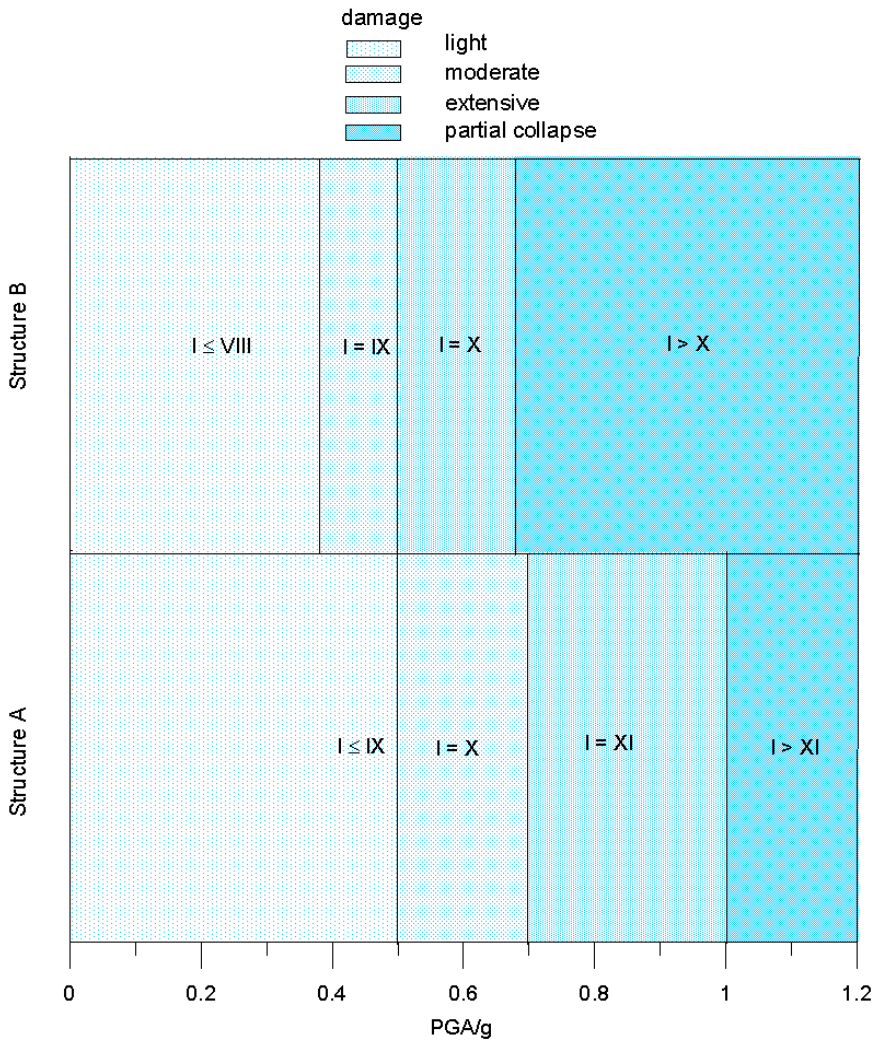

Figure 4.28. Comparison of damage grades of Structure A and Structure B

It can be seen from Figure 4.28 that the deficiencies in the construction increased the EMS-defined damage state of Structure B by one degree. In this way the most appropriate vulnerability class for Structure B is the vulnerability class D. It should be mentioned that the deficiencies in the construction of Structure B are caused by the poor execution of the reinforcement. The concrete and the steel were of good quality, as presented in Appendix A. In case of combination of bad quality of both materials and the execution of the reinforcement, an increase of the damage grade of Structure B of more than one degree might be expected. Consequently, the quality of construction does influence considerably the estimated seismic intensity and should be taken properly into account when applying the macroseismic intensity scales.

In Table 4.13 the expected EMS intensity is associated to the probability of failure and the damage indices. The structure would become light damaged from earthquakes with EMS intensity ≤ VIII, corresponding to PGA/g < 0.35. The partial collapse would take place during devastating earthquake with EMS intensity of XI and the corresponding PGA/g > 0.67.

5. **CONCLUDING REMARKS**

Based on the results of the experimental test on the two models of one storey cast-in-situ industrial frame and the numerical modelling of their seismic response, the main conclusions could be summarized as follows:

I. Seismic vulnerability of a one storey industrial frame designed according to Eurocode 8:

1. Under the imposed large storey-drift demands (up to 8.1%) visual evidences neither for flexural failure, nor for brittle failure of the structural members were observed. The substantial dissipation of hysteretic energy was supplied by spreading the ductility demands in large parts of the columns, as proved during the test with PGA of 80% *g*. In this way, the entire test verifies the adequacy of the detailing rules in Eurocode 8 for the critical confining reinforcement.

2. The experimental structure exhibited very reliable seismic behaviour, since the conditional probability of failure was less than 1% for PGA < 0.65% *g*. The frame would reach the ultimate limit state with provability of 95% at a PGA of 1 *g*. For the considered structure the light and moderate damage levels are connected to practically no probability of failure. The extensive damage level corresponds to the ambiguous part of the fragility curve and the partial collapse would take place at very high probability of failure ($Pf >$ 0.95). The structure will become light damage from earthquakes with European Macroseismic Scale intensity ≤ IX, corresponding to PGA < 50% *g*. The extensive damage would take place during devastating earthquakes with European Macroseismic Scale intensity of XI.

3. The displacement ductility supplies calculated from the experimental data by use of the criteria for the reduced stiffness equivalent elasto-plastic yield and equivalent elasto-plastic energy absorption gave a sligthly unconservative estimate due to the underestimation of the yield capacity of the considered structure. The implementation of the formulae in Eurocode 8 and in the new Italian Code and Panagiotakos and Fardis chord rotations at yield and at the ultimate provide slight conservative, but well coinciding with the experimental result estimates of the displacement ductility. The latter expressions could be recommended for validation of the results from push-over and non-linear time history analyses.

4. The calculated overall characteristics of the structural response, such as the displacement time history and the base-shear – storey displacement relationship coincided very well with experimental ones. At the same time the 'local' response characteristics, such as the curvatures, did not show good coincidence for all the tests. The larger values of the measured curvatures in the tests with high seismic intensity could be explained by the bond deterioration inside the joint core, which required more refined description in the numerical model. For all the tests the nominal curvature measured over the plastic hinge length showed satisfactory coincidence with the computed one, since the plastic hinge zones adjacent to the beam-column or beam-foundation joints were subjected to a strain 'interference' due to the deformation of the adjacent elements.

5. When using different models for the description of the seismic response of structures to different intensities, the genealogy of their hysteresis parameters is a prerequisite for their correctness. Simulations with accelerograms with longer effective duration could be recommended for the validation of such models.

6. The reduction of the design seismic loading due to underestimation of the structural stiffness leads to considerable decrease of the behaviour factor supply, which is dependent on the initial stiffness of the structure. The Eurocode 8 behaviour factor demand of 4.95 for ductility class 'High' could be matched for the studied structure only by consideration of initial stiffness corresponding to the initiation of cracking and not by the stiffness corresponding to the initiation of yielding of the reinforcement. In this context, when building structural model according to the prescriptions of Eurocode 8 concerning designation of some structural members as 'secondary', elimination of the contribution of the infills to the stiffness of the structure, implementation of stiffness of the lateral load bearing elements, which corresponds to the initiation of yielding of the reinforcement, the actual stiffness of the structure will be underestimated considerably. To improve this situation, a reconsideration of the abovementioned formulations in Eurocode 8 is needed.

II. Influence of the quality of construction on the seismic vulnerability of the experimental structure:

1. The deficiencies of the construction caused by the inaccurate execution of the reinforcement decreased considerably the seismic capacity of the structure as follows:

(i) the first yield displacement by 27% and the corresponding base shear force by 12%,
(ii) the ultimate storey displacement by 34 %,
(iii) the maximum base-shear force by 22%,
(iv) the behaviour factor supply by 35%,

2. The strongly decreased behaviour factor supply does not match the behaviour factor demand of 4.95 adopted by Eurocode 8. Consequently, the modern codes for seismic design, which imply large behaviour factor demands should provide the corresponding requirements for the quality of construction. In this context, it would be reasonable to introduce in Eurocode 8 a requirement for special measures concerning the quality of construction, when implementing the ductility class 'High'.

3. In the considered case, the quality of construction did not influence substantially the maximum structural response. Up to the peak ground acceleration for which the structure with the construction deficiencies reached the ultimate limit state, the larger difference with respect to the responses of the structure with good quality of construction was in the order of 5%. However, the enhanced ductility of the structure with good quality of construction supplied much larger ultimate storey displacement and therefore made it possible to sustain 40% larger peak ground acceleration.

4. The construction deficiencies increased the European Macroseismic Scale defined damage grade of Structure B by one degree. Accordingly, the appropriate vulnerability class is D instead of E. Consequently, the quality of construction influences considerably

the estimated seismic intensity and should be taken properly into account when applying the macroseismic intensity scales.

5. The deficiencies in the construction increased considerably the vulnerability of the structure, since the peak ground acceleration corresponding to equal probability of failure was decreased by approximately 0.25 *g*. The structure will become light damaged by earthquakes intensity ≤ VIII, corresponding to PGA/*g* < 0.35. The partial collapse would take place during devastating earthquake with EMS intensity of XI and the respective peak ground acceleration larger than 0.67 *g*.

6. For the both the structure with good quality of construction and the structure with deficiencies in execution strong correlation was proved between the overall structural damage index based on the modified Park and Ang damage model and the homogenized reinforced concrete damage scale damage index. This gives reasons for further implementation of the calculated values of the above overall structural damage index for prediction of the eventual observational damage.

7. The determination of the ultimate displacement as corresponding to 15% decrease of the peak base-shear force provides a conservative estimate of the ultimate state of the structure with deficiencies in execution with respect to the appearance of inelastic buckling.

8. The empirical formulae of Eurocode 8, new Italian Code and Panagiotakos and Fardis ultimate chord rotation of RC members provide very good estimates of the ultimate state for structures with good quality of construction. In the case of structures with serious deficiencies in the execution the considered empirical formulae overestimate the ultimate capacity of RC members by more than 20%.

REFERENCES

1. EN1992-1-1. Eurocode 2: Design of concrete structures. Part 1-1: General rules and rules for buildings. Commission of the European Communities, European Committee for Standardization, Draft January 1993.

2. ENV 1998-1-1. Eurocode 8: *Design of structures for earthquake resistance. Part 1: General rules, seismic actions and rules for buildings.* Commission of the European Communities, European Committee for Standardization. pr Draft №3, May 2001.

3. L. Ferrara*, Design calculations*. ECOLEADER research project: Seismic behaviour of reinforced concrete industrial buildings, 2002.

4. F. J. Molina, G. Verzeletti, G. Magonette, Ph. Buchet and M. Géradin, 'Bi-directional pseudodynamic test of a full-size three-storey building', *Earthquake Engng. Struct. Dyn*. 28, 1541-1566, 1999.

5. F. J. Molina, G. Verzeletti, G. Magonette, Ph. Buchet, V. Renda, M. Geradin, A. Parducci, M. Mezzi, A. Pacchiarotti, L. Federici and S. Mascelloni, 'Pseudodynamic tests on rubber base isolators with numerical substructuring of the superstructure and strain-rate effect compensation', *Earthquake Engineering & Structural Dynamics*, Vol. 31, 1563-1582 (2002).

6. J. Molina, G. Magonette and P. Pegon, 'Assessment of systematic experimental errors in pseudodynamic tests', Proc. 12th European Conference on Earthquake Engineering, 2002, Elsevier Science, Paper 525.

7. F. Biondini, L Ferrara, P. Negro and G. Toniolo, 'Results of pseudodynamic test on the prototype of a precast RC frame', Proc. 14th C.T.E. Congress, Mantova, Italy, November 2002.

8. PrEN 1998-1. Eurocode 8: *Design of structures for earthquake resistance. Part 1: General rules, seismic actions and rules for buildings.* Commission of the European Communities, European Committee for Standardization. PT Draft preStage 49 (Draft № 5), May 2002.

9. PrEN 1998-1. Eurocode 8: *Design of structures for earthquake resistance. Part 1: General rules, seismic actions and rules for buildings.* Commission of the European Communities, European Committee for Standardization. Stage 49 (Draft № 6), January 2003.

10. PrEN 1998-1. Eurocode 8: *Design of structures for earthquake resistance. Part 3: Strengthening and repair of buildings.* Commission of the European Communities, European Committee for Standardization. Final PT Draft, Stage 34 (Draft № 3), January 2003.

11. S. Morita, and T. Kaku, 'Slippage of reinforcement in beam-column joints of reinforced concrete frames'. Proc. 8th World Conference on Earthquake Engineering, 6, 477-484, 1984.

12. G. G. Penelis and A. J. Kappos, *Earthquake-resistant Concrete Structures*. E & FN Spon, London, 1997.

13. R.E. Valles, A.M. Reinhorn, S.K. Kunnath, C. Li and A. Madan, *IDARC 2D. A computer program for the inelastic damage analysis of buildings.* Technical report NCEER-96-0010, University of New York at Buffalo, 1996.

14. E. Bentz and M.P. Collins, *RESPONSE 2000. Reinforced comcrete sectional analysis using the modified compression field theory*. University of Toronto, 2000.

15. *Norme technice per il progetto, la valutazione e l'adeguamento sismico degli edifici*, Rome, 2003.

16. T. B. Panagiotakos and , M. N. Fardis, 'Deformations of reinforced concrete members at yielding and ultimate', *ACI Structural Journal*, 98, 2, pp. 135-148, 2002.

17. P. Negro and A. Colombo, 'How reliable are global computer models? Correlation with large-scale tests'. *Earthquake Spectra*, 14, № 3, pp.441-467, 1998.

18. Y. Lu, E. Vintzileou, G.F. Zhang and T.P. Tassios, 'Reinforced concrete scaled columns under cyclic actions'. *Soil Dynamics and Earthquake Engineering*, 18, pp. 151-167, 1999.

19. D. Coronelli and M.G. Mulas, 'Local-global approach in the seismic analysis of RC frames including bond slip effects', *Engineering Structures*, 23, pp.911-925, 2001.

20. M.D. Trifunac and A.G. Brady, 'A study on the duration of strong earthquake ground motion'. *Bulletin of the Seismological Society of America,* 65, pp. 581-626, 1975.

21. M. J. N Priestley, *Myths and fallacies in earthquake engineering, revisited*. The Mallet Milne Lecture, European School for Advanced Studies in Reduction of Seismic Risk, Pavia, 2003.

22. Y. Lu, H. Hong, P.G. Carydis and H. Mouzakis, 'Seismic performance of RC frames designed for three different ductility levels'. *Engineering Structures*, 23, pp. 537-547, 2001.

23. R. Park, 'Evaluation of ductility of structures and structural assemblages from laboratory testing'. *Bulletin of the New Zealand National Society for Earthquake Engineering*, 22, 3, pp. 155-166, 1989.

24. ATC. *Guidelines and commentary for the seismic rehabilitation of buildings*, vol. 1 and 2. Fema 273 and 274 Report, Washington: Federal Emergency Management Agency, 1997.

25. B. Borzi and A. S. Elnashai, 'Refined force reduction factors for seismic design'. *Engineering Structures*, 22, pp.1244-1260, 2000.

26. F. Biondini and G. Toniolo, 'Seismic behaviour of concrete frames: experimental and analytical verification of Eurocode 8 design rules'. Proc. FIB 2003 Symposium, Athens, 2003.

27. J. Kanda, 'Probability-based seismic margin index for inelastic members of reactor buildings'. Trans. 8th SMiRT, M1K2/5, pp.353-359, 1985.

28. J. Kanda, R. Iwasaki and H. Sunohara, 'Stochastic evaluation of inelastic seismic response of a simplified reactor building model'. Trans. 9th SMiRT, K1, pp.403-408, 1987.

29. K. Hirata, Y. Kobayashi, H. Kameda and H. Shiojiri, 'Fragility of seismically isolated FBR structure'. *Nucl. eng. and design*, 128, 227-236, 1991.

30. K. Hirata, Y. Ootori and T. Somaki, 'Seismic fragility analysis for base-isolated structure'. *Journal of struct. constr.eng., AIJ*, 452, 11-19, 1993. (in Jap.)

31. K. Hirata and T. Somaki, 'Fragility estimation of an isolated FBR structure considering the ultimate state of rubber bearings'. *Nucl. eng. and design*, 147, 183-196, 1994.

32. R.P. Kennedy and M.K. Ravindra, 'Seismic fragilities for nuclear power plant risk studies'. *Nucl. eng. and design,* 79, pp. 47-681984.

33. B.R. Ellingwood, 'Issues related to structural aging in probabilistic risk assessment of nuclear power plants'. *Reliability Engineering and System Safety*, 62, 171-183,1998.

34. R.W. Clough and J. Penzien, *Dynamics of structures*. 2nd edition, Mc Graw Hill, New York, 1993.

35. A. J. Kappos and P. Kyriakakis, 'A re-evaluation of scaling techniques for natural records'. *Soil Dynamics and Earthquake Engineering*, 20, pp. 111-123, 2000.

36. A. Elenas, 'Interrelation between seismic acceleration parameters of European earthquakes and the structural behavior'. *European Earthquake Eng*. 12, pp. 56-63, 1998.

37. S.L. Dimova and K. Hirata, 'Simplified seismic fragility analysis of structures with two types friction devices'. *Earthquake Eng. Struct. Dyn*. 29, pp.1153-1175, 2000.

38. S.L. Dimova and A. Elenas, 'Seismic intensity parameters for fragility analysis of structures with energy dissipating devices'. *Structural Safety*, 24, pp. 1-28, 2002.

39. A. J. Kappos, 'Sensitivity of calculated inelastic seismic response to input motion characteristics'. Proceedings of the 4th U.S. National Conference on Earthquake Engineering, EERI, Oakland California, p.25-34, 1990.

40. Y.J. Park and AH-S Ang, 'Mechanistic seismic damage model for reinforced concrete'. *Journal of Structural Engineering.* 111, pp. 722-739, 1985.

41. T. Rossetto and A. Elnashai, 'Derivation of vulnerability functions for European-type RC structures based on observational data'. *Engineering Structures*, 25, pp.1241-1263, 2003.

42. J. M. Bracci, A.M. Reinhorn, J. B. Mander and S.K. Kunnath, *Deterministic model for seismic damage evaluation of reinforced concrete structures.* Report NCEER-89-0033, State University of New York at Buffalo, 1989.

43. H. Hatamoto, Y. S. Chung and M. Shinozuka, 'Seismic capacity enhancement of RC frames by means of damage control design'. Proceedings of the 4th U.S. National Conference on Earthquake Engineering, EERI, Oakland California, p.279-288, 1990.

44. S. K. V. Gunturi and H. C. Shah, 'Building specific damage evaluation'. Proc. 10th World Conference on Earthquake Engineering, 10, pp.6001-6006, Madrid, 1992.

45. Conseil de l'Europe. *European macroseismic scale 1998 (EMS-98).* Cahier du Centre Europeen de Geodynamique et de Seismologie, G. Gruenthal, editor. Luxemburg, 15, 1998.

46. L. Ferrara, 'Seismic behaviour of reinforced concrete industrial buildings. Report of the test on the cast-in-situ prototype.' Technical Report - Department of Structural Engineering, Politecnico di Milano, September 2003.

47. E.Mola, G. Tsionis, F. Taucer and A. Pinto, *The Molise (Italy) earthquakes of 31 October and 1 November 2002: Report and analysis from field mission,* EUR 20664 EN, European Commission, Joint research Centre, IPSC, 2002.

48. J.J. Bommer *et al.*, 'The El Salvador earthquakes of January and February 2001: context, characteristics and implications for seismic risk'. *Soil Dynamics and Earthquake Engineering*, 22, pp. 389-418, 2002.

49. H. Sezen, A. S. Whittaker, K. J. Elwood and K. M. Mosalam, 'Performance of reinforced concrete buildings during the August 17, 1999 Koçaeli, Turkey earthquake, and seismic design and construction practice in Turkey'. *Engineering Structures*, 25, pp.103-114, 2003.

50. A. S. Elnashai, 'Analysis of the damage potential of the Koçaeli (Turkey) earthquake of 17 August 1999'. *Engineering Structures*, 22, pp.746-754, 2000.

51. A. Ansal and D. Slejko, 'The long and winding road from earthquakes to damage', *Soil Dynamics and Earthquake Engineering*, 21, pp. 369-375, 2001.

52. S. Pampanin, G. M. Calvi and M. Morrati, 'Seismic behaviour of R.C. beam-column joints designed for gravity loads'. Proc. 12th European Conference on Earthquake Engineering, 2002, Elsevier Science, Paper 726.

APPENDIX A. Material properties

1.1 Design values

Concrete

Characteristic compressive strength $f_{ck} = 40$ MPa

Design compressive strength $f_{cd} = \frac{f_{ck}}{\gamma_c} = \frac{40\ \text{MPa}}{1.5} = 26.7$ MPa

Long term design compressive strength $f_{c1} = 0.85\ f_{cd} = 0.85 * 26.7$ MPa = 22.7 MPa

Mean tensile strength $f_{ctm} = 0.3\ (f_{ck})^{2/3} = 3.5$ MPa

Characteristic tensile strength $f_{ctk} = 0.7\ f_{ctm} = 2.5$ MPa

Design tensile strength $f_{ctd} = \frac{f_{ctk}}{\gamma_c} = \frac{2\ \text{MPa}}{1.5} = 1.67$ MPa

Mean Young modulus $E_{cm} = 9500\ (f_{ck} + 8)^{1/3} = 35\ 10^3$ MPa

Steel
Type B500H

Characteristic yielding strength $f_{yk} \geq 500$ MPa

Design yielding strength $f_{sd} = \frac{f_{yk}}{\gamma s} = \frac{500\ \text{MPa}}{1.15} = 435$ MPa

Young modulus $E_s = 205\ 10^3$ MPa

1.2 Actual material properties

Concrete

Columns

Mean value of the cube (150 mm side) compressive strength $R_m = 51.5$ MPa

Mean value of the cylindrical compressive strength $f_{cm} = 0.83\ R_m = 42.75$ MPa

Mean Young modulus $E_{com} = 2.15\ 10^4\ (f_c/10)^{1/3} = 34.894\ 10^3$ MPa

Young modulus taking into account the initial inelastic strains [12]
$E_{cmel} = 0.85\ E_{com} = 29.66\ 10^3$ MPa

Mean tensile strength $f_{ctm} = 0.3\ (f_{cm})^{2/3} = 3.668$ MPa

Strain corresponding to the peak stress $\varepsilon_{cl} = 2\ f_{cm} / E_{com} = 0.00245$

Beams

Mean value of the cube (150 mm side) compressive strength $R_m = 56.9$ MPa

Mean value of the cylindrical compressive strength $f_{cm} = 0.83\ R_m = 47.2$ MPa

Mean Young modulus $E_{com} = 2.15\ 10^4\ (f_c/10)^{1/3} = 36.064\ 10^3$ MPa

Young modulus taking into account the initial inelastic strains [12]
$E_{cmel} = 0.85\ E_{com} = 30.655\ 10^3$ MPa

Mean tensile strength $f_{ctm} = 0.3\ (f_{cm})^{2/3} = 3.929$ MPa

Strain corresponding to the peak stress $\varepsilon_{cl} = 2\ f_{cm} / E_{com} = 0.00289$

Steel

The results from the tests on 600 mm steel bar samples of type B500H (ϕ16) are accepted in the entire work:

yielding strength $f_y = 550$ MPa

tension strength $f_t = 657$ MPa

ultimate elongation of 8% is considered.

APPENDIX B. The HRC-Scale

Table 1. Typical damage expected in ductile moment resisting frames (MRF) according to the HRC-scale:

DI_{hrc}	Damage state	Ductile MRF
0	None	No damage
10	Slight	Fine cracks in plaster partitions/infills
20	Light	Start of structural damage
30		
40		Hairline cracking in beams and columns near joints (< 1 mm)
50	Moderate	Cracking in most beams & columns
60		Some yielding in a limited number
70		Larger flexural cracks & start of concrete spalling
80	Extensive	Ultimate capacity reached in some elements – large flexural cracking, concrete spalling & rebar buckling
90		
100	Partial collapse	Collapse of a few columns, a building wing or single upper floor
	Collapse	Complete or impending building collapse